2016

Applicability of LiDAR Technology in Saltmarshes: Landscape-Scale Predictive Models to Local-Scale Biomass Estimation

James Dean Edwards Jr.
University of South Carolina

Applicability of LiDAR Technology in Saltmarshes: Landscape-Scale Predictive Models to Local-Scale Biomass Estimation.

By

James Dean Edwards Jr.

Bachelor of Science
East Carolina University, 2007

Master of Arts
East Carolina University, 2011

Submitted in Partial Fulfillment of the Requirements

For the Degree of Master of Science in

Marine Science

College of Arts and Sciences

University of South Carolina

2016

Accepted by:

James Morris, Director of Thesis

Jean Ellis, Reader

Ray Torres, Reader

Tom Allen, Reader

Lacy Ford, Senior Vice Provost and Dean of Graduate Studies

Acknowledgements

I would like to thank my committee for their support and enthusiasm during my time at Carolina. Dr. James Morris, thesis advisor, has been much more than an academic mentor. While developing the thesis, Dr. Morris was extremely supportive and provided invaluable programming and modeling guidance that prepares me for my career beyond academics. Above all, Dr. Morris has always been patient and provided unbiased feedback when approached with significant questions. For these reasons, Dr. Morris has been more of a father figure than a mentor, and words cannot describe my gratitude and loyalty towards Dr. Morris. Dr. Tom Allen and I have been working together since my tenure at East Carolina University and I am very thankful for his long term commitment. I would like to tank Dr. Jean Ellis and Dr. Ray Torres for serving on my committee and providing thoughtful feedback. The thesis would not have been possible without the assistance of many people. Special thanks are given to Trenton Agrelius, Warren Hankinson, Dr. Katherine Renken, Karen Sundberg, Dr. Matt Kimbal, Dr. Scott White, Dr. Dennis Allen, and the Baruch Institute Staff. Finally, I would like to thank my family, especially my wife, for their unwavering support while in graduate school.

Abstract

The management of saltmarshes requires detailed knowledge of the underlying processes driving their distribution in both time and space to make appropriate management decisions. With most of the world's population living in the coastal zone and rising sea levels, one of our most important natural resources in the coastal zone faces increasing threat of collapse. This study uses the current state of Light Detection and Ranging (LiDAR) technology to model and predict saltmarsh distribution at a landscape-scale and provide evidence that a terrestrial laser scanner (TLS) can be used to estimate saltmarsh biomass for inclusion into existing models.

Land cover classification of the dominant saltmarsh species, *S. alterniflora* and *S. patens*, of the Plum Island Estuary in Massachusetts indicate that when augmented by LiDAR, aerial imagery can spectrally discriminate these species allowing for the identification of species elevation range. A spatial 'bathtub' model of the estuary indicates that the saltmarshes will survive a 1m sea-level rise but not without a change in the dominant marsh plant species. These changes will occur at different rates along a latitudinal gradient owing to a difference in relative marsh tidal elevation.

Although the numerical Marsh Equilibrium Model (MEM) was developed with data from North Inlet, South Carolina and has been coupled with spatial models to predict saltmarsh distribution, no such study exists for North Inlet. A stand-alone python model, MEM3D, was created to couple MEM with a Geographic Information System (GIS) and

analyze the future distribution of saltmarshes within North Inlet following a 1m sea-level rise in the next 100 yr. Results indicate that the saltmarshes will not survive sea-level rise of this magnitude, and the system will switch to mudflat dominance by the end of the simulation.

A TLS was used to address the need to quickly and non-destructively estimate biomass. Results indicate that there exists an optimal resolution for collecting data in a saltmarsh and that contrary to airborne LiDAR systems, TLS can also penetrate the canopy to ground level. Predictive biomass equations are generated for *S. alterniflora* and *J. roemerianus* with $R^2 = 0$.

Table of Contents

List of Tables

List of Figures

Chapter 1: Literature Review and Problem Identification

The management of saltmarshes requires detailed knowledge of the underlying processes driving their distribution in both time and space to make appropriate management decisions. With most of the world's population living in the coastal zone and anthropogenic climate change causing sea levels to rise, one of our most important natural resources in the coastal zone faces increasing threat of collapse (Kirwan & Megonigal 2013; McGranahan, Balk, & Anderson 2007; Morris et al. 2002; Small & Nicholls 2003). Saltmarshes provide a suite of ecosystem services ranging from carbon sequestration, biodiversity support, wave attenuation, and storm surge protection (Barbier 2012; Chmura 2011; Gedan, Silliman, & Bertness 2009; Gedan et al. 2011; Zedler & Kercher 2005). These services are valuable to the people inhabiting proximal locations as they support local economies and protect infrastructure. Despite the value of saltmarshes to civilization, anthropogenic modifications of the landscape coupled with natural processes lend varying degrees of sensitivity. The sensitivity of these valuable resources will vary depending on local rates of sea-level rise, mineral sediment supply, productivity, and availability to uplands (Craft et al. 2008; Stralberg et al. 2011). The hypothesis most often postulated with global climate change and sea-level rise is loss of saltmarshes (Feagin et al. 2010). Predicting the future distributions of stressed saltmarshes, therefore, is important for the identification and protection of the most stable samples.

Saltmarsh ecosystems are known to have maintained an elevation in equilibrium with sea level during the late Holocene either by accumulating organic and mineral sediments at a rate compensatory for sea-level rise or by migrating upslope (Brinson, Christian, & Blum 1995; Moorehead & Brinson 1995; Morris 2007; Redfield 1972). The mechanism of saltmarsh maintenance is the tenet of the developed predictive models thus far. While many models of saltmarsh dynamics exist, they can be categorized as spatially distributed (Bartholdy, Bartholdy, & Kroon 2010; Bouma et al. 2007; French 2006; Temmerman et al. 2004) or zero-dimensional (Kirwan et al. 2010; Leonard & Croft 2006; Leonard & Luther 1995; Leonard & Reed 2002; Mudd, D'Alpaos, & Morris 2010; Nepf & Vivoni 2000; Peterson et al. 2004).

Spatially distributed models are the simpler of the two types to implement. Major uses of these models consist of inundation/floodplain mapping and saltmarsh migration. Gesh et al. (2009) utilized a simple spatial model to identify and delineate areas vulnerable to sea level rise from a series of elevation datasets. Wu, Najjar, & Siewert (2009) used elevation datasets to determine the population and infrastructure at risk due to inundation caused by sea-level rise for the mid and upper Atlantic states. When analyzing saltmarsh vegetation, spatially distributed models project the distribution of saltmarshes as a function of elevation contours (Temmerman et al. 2004). These projections ignore vegetation and its feedbacks, which result in under or overestimates of wetland loss (Stralberg et al. 2011). A specific model, the Sea Level Affecting Marshes Model (SLAMM), has a vegetative feedback mechanism but utilizes a constant linear accretion per wetland classification, which results in biased estimates (Craft et al. 2008).

These models can be appropriate, however, if vertical accretion is outpaced by sea-level rise, land cover is considered, and elevation is accurate (Feagin et al. 2010).

All models based on Krone's (1985) differential equations are zero-dimensional (Bartholdy, Bartholdy, & Kroon 2010). Such models include the Marsh Elevation Model (Morris et al. 2002) and its derived family (Kirwan et al. 2010; Kirwan et al. 2012; Mudd, D'Alpaos, & Morris 2010). Unlike spatial models such as SLAMM, these models use a non-linear accretion rate due to the presence of vegetation and ignore space by working on a single location. Vegetation has been shown to change the physics of a water column flowing through its canopies, promoting particle settling (Leonard & Croft 2006; Leonard & Luther 1995; Nepf & Vivoni 2000; Peterson et al. 2004). The change in physics associated with vegetation creates non-linear accretion rates applied as a function of inundation depth. Inundation depth is determined by the astronomical tides. Elevations near the lower limit of the vegetative tolerance, such as creek banks, receive the highest inundation depth resulting in the highest rates of mineral sedimentation. Elevations approaching the upper limit of vegetative tolerance receive the least mineral sedimentation. Organic contributions to vertical accretion are directly proportional to biomass, which has a maximum value at the species equilibrium elevation (Morris et al. 2002). Vegetative productivity has been proven a critical determinant of saltmarsh survivability.

Searching for key environmental factors that affect vegetation productivity has long been a major goal in biogeographical research (Kim, Cairns, & Bartholdy 2010). The spatial distribution of halophytic vegetation and productivity is not random nor spatially uncorrelated but exists in organized characteristic patches (Silvestri, Defina, &

Marani 2005). Environmental controls to productivity have been proposed to be salinity, sulfide levels, anaerobic conditions, nitrogen levels, and distance from tidal creek (Gross, Hardisky, & Klemas 1990; Silvestri, Defina, & Marani 2005). All of these controls, except the latter, are assumed to be a function of elevation as it determines the duration and frequency of tidal flooding, which in turn creates variability in the proposed controls (Morris et al. 2005; Rosso, Ustin, & Hastings 2006; Sadro, Gastil-Buhl, & Melack 2007; Silvestri, Defina, & Marani 2005). These controls lead to conditions promoting the most productivity at an equilibrium elevation within the tidal prism (Morris et al. 2002). Accurately measuring elevation is, therefore, an important process in predicting future wetland distributions.

. Airborne light detection and ranging (LiDAR) technology has been recognized by the forest ecology community to remotely derive structural characteristics of biomass such as volume, carbon content, leaf area and angle, roughness, and height segmented density (Antonarakis et al. 2010; Garcia et al. 2010; Hopkinson et al. 2004; Lin et al. 2010; Loudermilk et al. 2009; Popescu, Wynne, & Nelson 2003; Siedel et al. 2011). These uses, however, are significantly affected by properties of the LiDAR system and its interaction with vegetation. Typical airborne LiDAR systems have large footprints averaging to the decimeter scale resulting in posting densities of a few points per square meter at best. Vegetation characteristics, especially leaf dynamics, effect the penetration of the laser beam. Drake et al. (2003) found no generality of relationships between LiDAR and field derived structural metrics across species of tropical trees. Popescu, Wynn, & Nelson (2003) and Popescu, Wynne, & Scrivani (2004) suggest that airborne LiDAR can be used to estimate forest structural characteristics at the individual tree level.

Studies addressing the use of LiDAR technology in saltmarshes has only consisted of vertical error as a result of biomass (Sadro, Gastil-Buhl, & Melack 2007). Typical LiDAR error estimates are conducted by the vendor at easily assessable sites that usually are not in the salt marsh and vary drastically from such locations (Hodgson & Bresnahan 2004). Positive error bias of LiDAR in southeastern USA salt marshes up to 0.17 m have been reported (Chassereau, Bell, & Torres 2011, Hladik & Albers 2012, Montane & Torres 2006; Morris et al. 2005). The error between GPS ground truth elevation and LiDAR falls within accepted ranges of error on the platform but consistently higher near creek networks (Chassereau, Bell, & Torres 2011; Montane & Torres 2006). Advances in LiDAR technology, specifically Terrestrial Laser Scanning (TLS), show promise as a technique for non-destructive collection of biomass with canopy penetration.

TLS is a powerful ground based LiDAR system with a small footprint. These systems have millimeter scale footprints and are thus capable of achieving high posting densities. Additionally, these systems are designed to collect data up to a few thousand points per second and are highly mobile. Given these characteristics, TLS systems are ideal for collecting fine-scale canopy structure. Siedel et al. (2011) used a TLS system to monitor the total above ground biomass, leaf biomass and area, and stem biomass of greenhouse saplings. Their results suggest that TLS techniques agree with traditional techniques. Rosell et al. (2009) found a high correlation between field structure and TLS derived structure in citrus orchards. In a study of fuel bed dynamics in longleaf pine savanna ecosystems, Loudermilk et al. (2009) found that TLS performed better than field techniques. Their results suggest a correlation coefficient of 0.83 between TLS derived

vegetative volume and field observed biomass. With advances in LiDAR stemming from TLS technology, canopy biomass estimation is a future direction for research in the field.

Predicting the future distribution of saltmarshes requires attention to the identified limitations. These limitations are explored within three chapters. A spatially distributed model is used in Chapter 2 to explore topographic conditions, analyze the current distribution of saltmarsh vegetation, and predict their future distributions within the Plum Island Estuary (PIE). A spatial version of Morris et al's. (2002) Marsh Equilibrium Model (MEM) is developed for Chapter 3 to explore the tradeoff between input spatial resolution and computer processing time, and employ the model for North Inlet, SC. The frequency distribution of terrestrial LiDAR point clouds over the saltmarsh canopy is analyzed in Chapter 4 to explore the correlation with standing above ground biomass from *Spartina alterniflora* and *Juncus roemerianus* plots. Ultimately this research is intended to aid the coastal and saltmarsh management communities in understanding the spatial patterns of saltmarsh response to sea-level rise.

Chapter 2: Plum Island Estuary Long Term Ecological Research Reserve Saltmarsh Species Turnover and Migration during a Worst-Case Sea-Level Rise Event.

Coastal ecosystems face an uncertain future as a result of sea-level rise and anthropogenic landscape modification. Saltmarshes, highly productive coastal ecosystems, provide a range of economically valuable ecosystem services, such as carbon sequestration, biodiversity support, wave attenuation, and surge protection (Barbier 2012; Chmura 2011; Gedan, Alteiri, & Bertness 2011; Gedan, Silliman, & Bertness 2009; Zedler & Kercher 2005) but are highly susceptible to changes in mean sea level (MSL; Kirwan & Megonigal 2013). This susceptibility is problematic because global sea level has risen for the last 10,000 years with recent decadal rates recorded as 2-3 mm per year for the northeast United States (Nydick et al. 1995; Schmitt, Weston, & Hopkinson 1998). Forecasts predict acceleration in current rates resulting in centennial (2100) MSL increases of 20-180 cm, with 100 cm being an average (Craft et al. 2008; Schile et al. 2014). With over 53% of the US population living in the coastal zone, it is important to identify the mechanisms in which saltmarshes survive sea-level rise to predict and protect their future extent (Craft et al. 2008). This study classifies 2011 aerial imagery to define the composition, extent, and elevation range of saltmarsh species in a New England estuary and employs a 'bathtub' model to predict species turnover and distribution with sea-level rise.

The survivorship of saltmarshes with sea-level rise is contingent upon their ability to accrete vertically and/or migrate laterally (Cavatarta et al. 2003; Kirwan & Megonigal 2013; Morris et al. 2002; Schmitt, Weston, & Hopkinson 1998). Coastal plain, or bar built lagoons, and fjords constitute a majority of estuaries in New England while drowned river valleys are present in low numbers (Roman et al. 2000). Deep coastal water combined with steep bedrock topography limit the lateral expansion of most New England saltmarshes (Warren et al. 2002). Drowned river valleys, however, with low sloping topography provide the greatest protection from wave energy and the shallowest coastal waters. Coupled with steady sea-level rise, the topography of drowned river valleys resulted in slow marsh development at MSL that vertically matched or slightly exceeded sea-level rise depending on availability to sediment (Morris, Schaffer, & Nyman 2013; Nydick et al. 1995; Orson, Warren, & Niering 1998; Redfield 1972; Schmitt, Weston, & Hopkinson 1998). Saltmarshes in New England, however, are currently situated at an elevation approximating mean high-water (MHW) because of a large pulse of sediment input caused by century-long inland deforestation during the industrial revolution that led to rapid accretion of sediment and relative elevation increase (Gedan, Altieri, & Bertness 2011; Kirwan et al. 2011; Roman et al. 2000). This sedimentation altered spatial distribution of saltmarsh species because species composition within the marsh is dependent on elevation relative to tidal datum (Marani, Lio, & D'Alpaos 2013).

The saltmarshes of New England are dominated by cordgrasses. Tides inundate the low marsh daily, resulting in increased anaerobic conditions and decreased salinities compared to the irregularly flooded high marsh (Bertness & Ellison 1987). The dominant

cordgrass of the low marsh is *Spartina alterniflora* while *Spartina patens* dominates the high marsh (Bertness & Ellison 1987; Nydick et al. 1995; Redfield 1972; Redfield and Ruben 1962; Schmitt, Weston, & Hopkinson 1998). The ability of these species to trap sediment is highly dependent upon the duration of inundation, which in turn is dependent upon the elevation within the tidal frame (Schmitt, Weston, & Hopkinson 1998). Thus, accretion rates vary by species. Suspended sediment concentrations are currently low in New England as a result of the re-growth of the once dominant forests (Morris, Schaffer, & Nyman 2013). Total suspended sediment (TSS) concentrations of ~4 mg/L are reported in a main river channel and associated estuary of New England with slightly higher concentration (~12-14 mg/L) within tidal creeks but no significant differences in marsh sedimentation rate with distance from source (Cavatarta et al. 2003; Schmitt et al. 1998). Recent rates of vertical accretion for a New England saltmarsh are estimated to be 0.22 cm/yr (Morris, Schaffer, & Nyman 2013). With current high marsh dominance and accelerating sea-level rise, these marshes are not in equilibrium with current rates of sea-level rise (Cavatarta et al. 2003).

Sea level rise will inundate lands currently above the tidal prism thereby providing accommodation space for saltmarsh lateral migration while simultaneously flooding the shoreward marshes. As sea levels rise, stable saltmarshes will transgress inland at a rate that reflects hinterland topography (Morris 2007; Townend et al. 2011). Submergence on the shoreward side of existing northeastern saltmarshes will change species distributions. The present distribution of cordgrasses, with large *Spartina patens* meadows fringed by *Spartina alterniflora,* is evidence of ongoing submergence due to sea-level rise (Nydick et al. 1995). It is important to identify potential accommodation

space and the way in which these marshes will change in order to direct management and protection measures of these areas.

This study addresses how the species composition and distribution of saltmarshes in a New England estuary will change during predicted sea-level rise. A New England estuary is segmented topographically to test the hypotheses that 1) 2011 species composition and distribution is not uniform across the estuary and 2) species composition will turnover due to the effects of sea-level rise and their respective distributions will be spatially variable. The specific objectives of this study are to 1) use LiDAR to spatially segment a New England estuary, 2) augment aerial imagery with hydrological information to provide a supervised land cover classification, and 3) employ a 'bathtub' model to forecast species composition and distribution during sea-level rise. It is expected that LiDAR, when corrected for internal errors, can provide a quantitative method to spatially segment a New England estuary, and that coupling hydrological information with aerial imagery can provide high-accuracy species classification. The approach used in this study builds on the work of Millette et al. (2010).

Methods

Study Area

The Plum Island Estuary-Long Term Ecological Research Reserve (PIE-LTER; Figure 2.1) is located in Massachusetts and is characterized as a macro-tidal estuary with a maximum astronomical tide range of approximately 3 m. PIE is the largest wetland-dominated system of the northeast USA containing saltmarsh cordgrass (*Spartina alterniflora*), marsh hay (*Spartina patens*), and tidal flats as the dominant intertidal land

cover types with deeply incised tidal creeks, pannes, and ponds (Millette et al. 2010). The high marsh platform, dominated by *S. patens,* has been extensively altered by drainage ditches dug for mosquito control and marsh hay production (Roman et al. 2000). The system receives minimal sediment loads from the region's major river systems.

Watershed Delineation

The elevation layer used for watershed delineation in this analysis was 2011 LiDAR obtained from the Woods Hole Marine Biological Laboratory (MBL) and referenced to the North American Vertical Datum of 1988 (NAVD88), a leveling network on the North American continent affixed to a stable location in Quebec (National Geodetic Survey 2016). The data used to define the boundary of PIE was reclassified 2005 LiDAR as discussed by Millette et al. (2010). Data analysis consisted of the following steps: a) vertical elevation correction, b) image classification, c) watershed delineation and attribute enumeration, and d) flooding the landscape. All spatial data were processed in ESRI ArcMap, and all statistical analyses were performed in SAS.

The first step was standardizing the LiDAR elevations to mean sea level (MSL). Mean sea level at the National Oceanographic and Atmospheric Administration (NOAA) tide gauge 8443970 in Boston Harbor was determined at NAVD88 -0.09 m for the 1983-2001 tidal epoch (NOAA Tides and Currents 2013A). Sinks and noise, or erroneous elevations, existed within the LiDAR data. Sinks were located and eliminated by raising the sink to the elevation of its nearest neighbor (Chang 2008; Jenson & Domingue 1988). A 3x3 local mean filter was used to process the LiDAR DEM identically to Millette et al. (2010) 2005 LiDAR processing, and update the focal pixel to the mean of the nine pixels, thereby smoothing the data. To test the accuracy of the data, LiDAR measurements are

compared against twelve Faststatic GPS measured Surface Elevation Table (SET) points (Figure 2.2; Table 2.1) obtained from Wood's Hole Marine Biological Laboratory (MBL) staff and adjusted to reference 0m MSL.

Image Classification

Land cover classification was conducted to provide estimates of current marsh species distribution and elevation range. A supervised maximum likelihood classification of 2010 4-band NAIP (USDA National Agricultural Imagery Program) was performed to derive land cover types of the study area. The data were collected July through August, 2010, during maximum leaf-on growing season. Training points (n = 175; Figure 2.3) defining ground truth marsh vegetation (*S. alterniflora*, *S. patens*, *Phragmites australis*, and brackish/*Typha sp*.) were obtained from MBL and University of South Carolina Belle W. Baruch Institute for Marine and Coastal Sciences' staff. An additional 291 training points representing anthropogenic structures, upland vegetation, water, ponds, and tidal flats/bare mud were digitized manually on the imagery. All training points were labeled by cover type and buffered 1 m to provide training polygons. Using the maximum likelihood classifier, each pixel of the imagery was assigned a land cover type based on spectral signatures. Input bands were red, green, blue, and near-infrared obtained directly from the imagery plus two developed bands: NDVI (Normalized Difference Vegetative Index) and a composite band. NDVI was calculated as described by Jensen (1996) to represent photosynthetic activity (Figure 2.4). A composite image was developed by changing the band directories of a standard red-green-blue image and later grey-scaling the image to further delineate differences in vegetative pigmentation (Figure 2.5; Liew 2001). The band association is near-infrared as red, NDVI as green, and green as blue.

The result of the supervised classification was the creation of 4 land cover classes: a) marsh vegetation, b) upland trees, c) bare cover, and d) developed land. These classes were grouped as current marsh (a), accommodation space (b) and area unsuitable for marsh migration or development (c and d; Figure 2.6; Table 2.2).

To test the spectral classification and ecological zonation of the similar saltmarsh species, histograms of 2011 LiDAR elevations were developed. Image classification was insufficient to fully separate the saltmarsh vegetation and *S. alterniflora* was further classified. All pixels representing *S. alterniflora* with a class probability from the maximum likelihood classification less than 95 % were considered *S. patens*. Distance to nearest hydrological unit (Figure 2.7) was calculated for all remaining *S. alterniflora* pixels. All pixels beyond a threshold of 10 m were considered *S. patens*. The threshold of 10 m was chosen because this is the location on the histogram (Figure 2.7) where frequencies begin to level off under 1% of total observations. Updated elevation statistics for the final histogram (Figure 2.8) were tested against 378 *S. alterniflora* and 334 *S. patens* ground truth elevations for statistical agreement, and agreement improved (Table 2.3).

Accuracy assessment of the classification was conducted by overlaying classified land cover against 1013 separate land cover ground-truth points obtained from MBL staff and random manual identification (Table 2.4). Kappa indices exceeding 75 % are satisfactory while those exceeding 85 % are exemplary (Fielding & Bell 1997; Foody 2002; Landis & Koch 1977). Classification was considered a true positive if the reference was within 1 m of a correctly classified land cover pixel, assuming normal positional

accuracy of handheld GPS units. Classified land cover coupled with delineated watersheds allowed for identification of spatially explicit properties for PIE.

Watershed Delineation

Delineation of watersheds was determined by defining flow paths, accumulation, and stream networks. It is difficult to assign flow paths in flat terrain typical of coastal environments, resulting in erroneous watersheds (Chang 2008). Consequently, topographic variability was artificially enhanced by adding 1m to the LiDAR elevations and then cubing them. The resulting watersheds were vectorized and all contributing sub-watersheds of large drainage networks merged into a single watershed. The vectorized watersheds were clipped to areas above MSL as this represented the location of the existing marsh platform.

Topographic Attributes

Current and future intertidal statistics were calculated for each watershed to provide data explaining 2011 topographic conditions. The tidal amplitude of MHHW, the assumed maximum elevation of marsh vegetation growth, was determined to be 1.55 m at tide gauge Boston Harbor (NOAA Tides & Currents 2013b). A simple reclassification was used to represent current and future intertidal area based the assumption of constant MHHW throughout PIE. The 2011 processed LiDAR dataset was clipped to all area between current MSL and future MHHW (0 - 2.55 m) assuming a 1 m SLR event to represent only the area that is expected to be currently covered by marsh or the area that is susceptible to marsh development under rising sea-level. To remove areas unsuitable for marsh migration or development, two steps were used. First the identified stream network was merged with a ditch drainage network delineated by Millette et al. (2010)

and buffered by 1 m to form polygons. Secondly, classified unsuitable land cover was used to remove all unsuitable cover. Watershed attributes describing the topography of all areas currently or susceptible to being intertidal were enumerated.

Topography was used to identify the 2011 surface patterns of existing marshes and their expected accommodation space assuming a 1 m SLR. Topographic attributes (Tables 2.5 - 2.6) consisted of metrics that explained the physical shape and distribution of elevation within each watershed's current and future intertidal landscape, respectively. Current intertidal area was calculated as the sum of the area of all pixels occurring within each watershed. Slope was calculated to identify the flatness of each watershed. The same metrics were calculated for accommodation space, assuming a 1 m SLR. All 2011 current and future intertidal LiDAR elevations are converted to cell center points and exported for time-series analysis within SAS to track and update current and future marsh pixels.

Change Statistics

It was necessary to define a threshold elevation of species zonation to determine change in vegetation distribution and area due to SLR during the analysis period. The threshold elevation used to distinguish *S. alterniflora* and *S. patens* was 1.29 m. The threshold was derived from the intersection of the species elevation histograms (Figure 2.8) located one standard deviation above the *S. alterniflora* mean elevation and one standard deviation below the *S. patens* mean elevation. Elevations above this threshold were assigned *S. patens* while elevations below were assigned *S. alterniflora*. This threshold provides an elevation rule that can be used to update potential marsh vegetation as MSL increases. Mean sea level was modeled to accelerate to 1 m over the next century

(Figure 2.9). Rearranging Equation 2.1 with the desired 100 m global sea level rise (gSLR) in 100 years (t) and current linear trend of 0.0028 m/yr (A) observed at tide gauge Boston Harbor (NOAA 2013c) provides the accelerating coefficient (B: m/yr).

$$gSLR = At + Bt^2 \quad (2.1)$$

Equation 1 was used in a time series with 2011 LiDAR to model the annual addition and/or loss of intertidal area within each watershed under the SLR scenario. Elevation points are representative of 1 m^2 ground cover. The *Spartina sp*. elevation thresholds were used to model vegetation change in each watershed. Annual change of intertidal area and cover of *Spartina sp.* dominance was tracked and plotted during the 100 year scenario.

Results

Mean Absolute Error (MAE) between twelve SET locations and 2011 LiDAR (Table 2.1) was found to be -0.09 m with individual differences ranging from -0.01 m - 0.22 m and no discernible spatial pattern. 2011 NAIP PIE classification is presented in Figure 2.6. 2011. Distance to the nearest drainage feature for all *S. alterniflora* classified pixels exceeding 95 % confidence is presented in Figure 2.7. Overlapping histograms representing corrected *S. alterni*flora and *S. patens* are presented in Figure 2.8. Mean 2011 LiDAR elevation for *S. alterniflora* was 0.92 +/- 0.37 m compared to 1.50 +/- 0.22 m for *S. patens*. Classification accuracy is presented as a confusion matrix (Table 2.4) displaying ground truth versus classified land cover statistics. Unsuitable land cover was classified correctly 245 times out of 249 ground truth points for user accuracy of 98.39%. *S. alterniflora* was classified 309 times out of 378 ground truth observations for user

accuracy of 81.75 %. Upland trees were classified correctly 92.31 % while *S. patens* was classified correctly 95.51 %. Producer accuracy ranged from 86.45 % for *S. patens* to 95.67 % for *S. alterniflora*. Overall accuracy was measured to be 90.92 % with a Cohen's Kappa index of 86.89 %.

Watershed results are presented for the riverine and tidal creek systems on the western boundary of Plum Island Sound. There were 57 sub-watersheds identified overall, which were merged into 6 larger watersheds (Figure 2.10). 2011 LiDAR derived intertidal topographic attributes of each watershed are presented in Table 2.5. Intertidal area varied from 0.66 km^2 to 7.71 km^2. Mean intertidal elevation across all watersheds ranged from 1.30 m to 1.39 m. Current intertidal slope increased from a low of 2.51° to a high of 3.06°. Mean elevation was used as a primary grouping rule for PIE watersheds. The northern region, defined by the cumulative extent of the watersheds of the Parker River, Merrimack-Plum Blush Creek, and a large tidal creek, had a mean 2011 elevation at 1.38 m and an average surface slope of 2.6°. The southern region, defined as the cumulative extent of the watersheds of the Ipswich River, Rowley River, and a smaller tidal creek, had a mean 2011 elevation at 1.31 m and an average surface slope of 2.79°.

Intertidal topographic results for the modeled 1 m SLR are presented in Table 2.6. During a 1 m SLR in 100 years, the available accommodation space ranged from 0.15 km^2 to 4.33 km^2. Mean elevation of the accommodation space was between 1.62 m and 1.88 m with surface slope from 1.13° to 2.78° respectively. The northern region contained 8.09 km^2 of accommodation space with a mean elevation of 1.76m and a surface slope of 1.82°. The southern region contained 4.06 km^2 of accommodation space at a mean elevation of 1.77 m and a surface slope of 1.98°. The total amount of intertidal

area changed between 2011 and the 100 year model output as the result of a 1 m rise in sea level (Table 2.7). Watershed intertidal area increased between 12.12 % and 74.45 % while on a regional basis, intertidal area increased 21.54 % for the southern region and 54.76 % for the northern region.

Marsh vegetation coverage and distribution was different between 2011 and the 100 year model output (Table 2.8). Regionally, *S. alterniflora* covered 16.54 % of the northern region and 30.39 % of the southern region in 2011 compared to 83.46 % and 69.61 % for *S. patens* respectively. At the year 100 output, *S. alterniflora* covered 96.97 % of the northern watersheds and 97.02 % of the southern watersheds compared to 3.03 % and 2.98 % for *S. patens*, respectively. Time series vegetation analyses of the 100 year 1 m modeled SLR are presented in Figure 2.11. Rate of change in intertidal area during the 100 year sea-level rise is presented in Figure 2.12.

Discussion

The approaches used in this study address the predictions that: 1) 2011 saltmarsh species composition and distribution is not uniform across the PIE estuary and 2) species composition will turnover due to the effects of sea-level rise and their respective distributions will be spatially variable. The study used watershed delineation of corrected LiDAR elevations and aerial imagery combined with distance to nearest hydrologic feature to meet the objectives of the study. Topographic attributes suggest that the PIE study site can be split into two distinct regions. It was found that in 2011, the northern region was dominated by a higher percentage of *S. patens* than the southern region.

Following a 1 m 100 year sea-level rise simulation, it was found that a species turnover occurred resulting in *S. alterniflora* dominance, which was highest in the southern region.

Watershed delineation provided appropriate boundaries after errors within the 2011 LiDAR were corrected and the variance in elevation artificially inflated. Use of a low-pass filter to correct for errors is acceptable because studies show smoothed data are highly correlated to reference ground elevation measurements (Hodgson & Bresnahan 2004; Millette et al. 2010). To assess accuracy of smoothed 2011 LiDAR for PIE saltmarshes, known elevations from SET's on the marsh platform were compared to 2011 LiDAR elevations. The mean absolute error between datasets was 0.09 m, an acceptable error because it was within the vendor reported error. LiDAR errors can be very high in marshes due to dense vegetation cover obstructing the laser pulse from reaching the soil surface (Chassereau, Bell, & Torres 2011; Hladik & Albers 2012; Montane & Torres 2006; Morris et al. 2005). The error of this data is small because the data were collected in early April during low tide with the marsh denuded of vegetation.

The method used to increase the variance in 2011 LiDAR elevation proved satisfactory. Low relief landscapes, a characteristic of saltmarshes, are difficult to model hydrologically because of the inability of algorithms to appropriately identify surface flow, resulting in unusual boundaries (Chang 2008). The six delineated watersheds were topographically correct. The watersheds were characterized by expected non-linear boundaries following defined hydrological features and shared borders were found to occur on interfluves created by the method used to increase the variance in elevation. Of the six delineated watersheds, the Rowley River watershed was the most complex. The Rowley River watershed exists as a composite of a large intertidal creek and the Rowley

River (Figure 2.10). It was assumed during watershed delineation that similar properties of water during the tidal cycle (sediment concentration, velocity) would affect the associated saltmarshes in the same way. By virtue of this delineation method, a large portion of intertidal area and its creek network was connected to the Rowley River. It appears that this large creek, which exists between the Rowley and Ipswich Rivers, would have been defined as a tide creek watershed under the delineation without sea-level rise. As sea levels have risen and tide creeks meandered, migrated, and formed, this entire section was connected to the Rowley River.

Classification results for the desired saltmarsh species and potential accommodation space are satisfactory. Classification of species from remotely sensed imagery is a popular topic dependent on spectral signatures of individual species. Spectral signatures are not unique to plant types, but to evolutionarily similar populations (Artigus & Yong 2006). It was not surprising that ancillary data had to be used to discriminate *S. alterniflora* and *S. patens,* since the species belong to the same genus. Because *S. alterniflora* has been described to fringe large *S. patens* meadows, distance to nearest hydrological feature was used to further discriminate the species (Nydick et al. 1995). Figure 2.7 is interpreted that within the initial classified *S. alterniflora*, some pixels beyond 10 m from the nearest hydrologic feature are not fringing and represent misclassified *S. patens*. The desired elevation frequencies after thresholding distance to hydrologic features are presented in Figure 2.8. *S. alterniflora* has been reported to have a mean elevation of 0.9 +/- 0.3 m for PIE, directly corroborating results of the *S. alterniflora* classification (Morris, Sundberg, & Hopkinson 2013). Elevations for classification of *S. patens* are, however, not in agreement with Morris et al. (2013) but are

in agreement with independent reference elevations provided by MBL staff. A potential explanation for this could be that the reference elevations were collected from a greater spatial range and are more representative of the *S. patens* population. The saltmarsh classification is appropriate for PIE as elevations for both species classifications are supported by external studies.

Overall accuracy places the classification as excellent. It is assumed that if a classified land cover occurs within 1 m of an identifying ground truth, a correct classification occurred. This assumption is warranted on the grounds of GPS horizontal accuracy, typically upwards of 5 m in open terrain (Wing, Eklund, & Kellogg 2005). This indicates that when overlying datasets, especially those collected from different sensors as is the case for NAIP imagery (aerial mounted GPS) and field collection (consumer grade hand-held units), it cannot be assumed that there is an exact overlap. While a 5 m buffer could be used, it is assumed that 5 m in a saltmarsh represents a distance in which micro topography can change rapidly, resulting in rapid change in saltmarsh vegetation. This scenario would inflate accuracy by increasing the probability that a classified land cover would be found within the buffer distance of a field observed land cover. While Cohen's kappa is preferred over overall accuracy as it corrects for random chance agreement (Foody 2002), it is misleading such that producer, user, and overall accuracy are preferred (Pontius & Millones 2010). User accuracies were high, exceeding 90 % for all land cover classes except *S. alterniflora* (81.75 %). Similar results were found for *S. patens* (86.45 %) under producer accuracy. The findings suggest that although efforts were made to classify the species based on spectral signature coupled with distance to nearest hydrological unit, some *S. alterniflora* pixels were misclassified as *S. patens*.

Despite this continued but alleviated error, PIE classification, overall accuracy = 90.92 %, is satisfactory to define species composition.

Saltmarsh species composition and distribution is not uniform across the PIE estuary. The topographic analysis presented indicate that the delineated PIE watersheds can be quantitatively split into two regions: north and south. Mean intertidal elevation for the delineated watersheds fall within 2 ranges, thereby forming a grouping rule. Intertidal area of the southern watersheds exist at a slightly lower modal elevation (1.31 m) and are more sloped than those in the northern group (1.38 m), which are nearly 0.1 m higher in the tidal prism exhibit a decreased surface slope up to 0.19°. Data displayed in Table 2.8 representing species composition at 2011 confirm that the PIE saltmarshes are spatially variable in species composition and distribution. *S. patens* dominated the 2011 saltmarshes, comprising 83.46% of the northern region (13.24 km^2) and 69.61 % of the southern region (12.44 km^2). 2011 species composition data indicate that the southern marshes, existing slightly lower in modal elevation are presently exhibiting the early effects of an accelerating sea-level rise.

Species composition in 2011 will turnover during sea-level rise and the changes in saltmarsh distribution will be variable by region. Time series analysis of the saltmarsh species composition by PIE region indicate a complete saltmarsh species turnover from 2011 *S. patens* dominated to saltmarshes dominated by *S. alterniflora* in 2111. Following the 1 m sea-level rise, *S. alterniflora* compositions were 96.97 % and 97.02 % for the northern and southern regions respectively. The timing of saltmarsh species turnover was interpreted as an intersection in composition curves. Figure 2.11 displays saltmarsh composition within each region during the modelled sea-level rise. It is estimated that

species turnover will occur at approximately 25 years into the sea-level rise for the southern region and 35 years for the northern region. This places PIE saltmarsh species turnover occurring approximately 2036 and 2046, respectively, based on 2011 LiDAR.

Analysis of the rate of change in intertidal area for each region indicates that saltmarshes existing in 2011 will expand and survive a 1 m sea-level rise in 100 years. The fact that no negative rates of change were observed (Figure 2.12) indicates that the saltmarshes of both regions experience a larger increase in area due to migration than losses due to submergence. Landward portions of *S. patens* saltmarshes, currently existing high in the tidal prism, will slowly migrate onto limited accommodation space while the shoreward portions will continue to lose relative elevation and shift to *S. alterniflora* saltmarshes. One hundred year increases in intertidal area were found to be 54.76 % and 21.54 % for the northern and southern regions respectively. It is interpreted from Figure 2.12 that the northern region will increase at least 1 % in area from each previous year for approximately 20 years while the southern watersheds will only increase at approximately 0.4 % during the same time. Accommodation space statistics for each region corroborate this pattern. Total area of accommodation space is reported from Table 2.7 to be 8.09 km^2 with an average surface slope of 1.82° for the northern region and 4.06 km^2 with an average surface slope of 1.98° for the southern region at nearly similar modal elevations (1.76 m and 1.77 m respectively). The increased slope of the southern region is interpreted that the accommodation space butts the natural upland berm, thereby hindering the migration of the saltmarshes compared to the northern region.

It is predicted that although PIE saltmarshes will survive a 1 m 100 year sea-level rise, a species turnover from 2011 *S. patens* dominance to *S. alterniflora* dominance will occur with current suspended sediment concentrations. Ecological consequences of such a change a largely unknown and undocumented at the current time. Research, however, on estuarine community dynamics and food webs are being conducted within PIE (Johnson 2014; Johnson 2015; Nelson, Deegan, & Garrit 2015). Future research should focus on including vegetative feedback as described by Morris et al. (2002) plus large scale hydrodynamic models and sediment budgets beyond the capabilities of this analysis. Incorporating these improvements would likely shift the timing of species turnover further into the future as the marshes would be actively trapping sediment and increasing relative elevation.

Conclusion

Data provides evidence that PIE saltmarshes will survive a 1 m SLR but will undergo a species turnover event and that changes will occur differently on north-south delineation. Data reported from the classification indicate that in 2011, PIE was dominated by large *S. patens* meadows with a smaller coverage of fringing *S. alterniflora*. 2011 LiDAR statistics delineate 2 geographic regions within PIE: north and south. The northern region comprises the watersheds of the Parker River, Merrimack-Plum Blush Creek, and a large multi-order tidal creek system. The Southern region comprises the watersheds of the Ipswich River, Rowley River, and a large multi-order tidal creek system. The northern region is found to exist at a higher modal elevation, 1.38 m, and flatter, 2.60°, than the southern region (1.31 m, 2.79°). 2011 LiDAR based area

for the regions are similar at 13.24 km^2 and 12.44 km^2 respectively. Accommodation space was found to be 8.09 km^2 and 4.06 km^2 at modal elevations of 1.76 m and 1.77 m respectively. Modelling an accelerating sea-level rise resulted in increases of intertidal area at 54.76 % and 21.54 % for the northern and southern regions respectively. The research suggests complete species turnover is expected to occur at 2025 and 2035 for the southern and northern regions.

Table 2.1. Fastatic GPS measured SET elevation vs 2011 LiDAR elevation.

SET Name	Latitude (°)	Longitude (°)	SET Elevation (m)	2011 LiDAR Elevation(m)	Absolute Error (m)
Levine 1	42.727660	-70.852891	1.42	1.45	-0.03
Levine 3	42.727678	-70.853661	1.44	1.50	-0.06
HI1	42.731192	-70.826261	1.23	1.32	-0.09
HI2	42.730583	-70.826725	1.32	1.48	-0.16
MI1	42.729118	-70.834729	1.04	1.10	-0.06
MI2	42.729238	-70.835457	0.99	1.09	-0.10
MI3	42.729418	-70.836333	1.04	1.13	-0.09
LP1	42.731573	-70.841493	1.28	1.23	0.05
LP2	42.731250	-70.842197	1.29	1.30	-0.01
FP2	42.728319	-70.850066	1.08	1.23	-0.15
FP3	42.728383	-70.850162	1.32	1.54	-0.22
OLT2	42.727904	-70.852571	1.32	1.52	-0.20
			Mean Absolute Error (m)		-0.09

Table 2.2. Land cover codes used in 2010 NAIP 4-band image classification.

Training Code	Training Land Cover Classification	Final Classification Code	Final Land Cover Classification
1	*S. alterniflora*	1	*S. alterniflora*
2	*S. patens*	2	*S. patens*
3	*P. australis*	2	*S. patens*
4	Water	4	Unsuitable
5	Tidal flats/Bare mud	4	Unsuitable
6	Wet Ponds	4	Unsuitable
7	Upland Trees	3	Upland Trees
8	Roads	4	Unsuitable
9	Boats/Docks	4	Unsuitable
10	Buildings	4	Unsuitable
11	Brackish/*Typha sp.*	2	*S. patens*

Table 2.3. 2011 mean elevation and standard deviation of classified *S. alterniflora* and *S. patens* compared to ground-truth species mean and standard deviation.

	S. alterniflora		*S. patens*	
	Post	Ground Truth	Post	Ground Truth
Mean Elevation (m)	0.92	1.25	1.50	1.48
Standard Deviation (m)	0.37	0.32	0.22	0.10

Table 2.4. 2010 NAIP land cover classification confusion matrix.

	Reference						
Classified	Unsuitable	*S. alterniflora*	Upland Trees	*S. patens*	Row Total	User Accuracy (%)	Commission Error (%)
Unsuitable	245	0	4	0	249	98.39	1.61
S. alterniflora	19	309	0	50	378	81.75	18.25
Upland Trees	4	0	48	0	52	92.31	7.69
S. patens	0	14	1	319	334	95.51	4.49
Column Total	268	323	53	369	1013		
Producer Accuracy (%)	91.42	95.67	90.57	86.45			
Omission Error (%)	8.58	4.33	9.43	13.55			
Overall Accuracy (%)	90.92						
Kappa (%)	86.89						

Table 2.5. 2011 intertidal above MSL topographic statistics for the delineated PIE watersheds and respective regions.

Watershed	Area (km2)	Mean Elevation (m)	Mean Slope (°)
Merrimack	5.56	1.36	2.51
Parker	6.01	1.38	2.68
Tide Creek 2	1.67	1.39	2.61
North	13.24	1.38	2.60
Tide Creek 1	0.66	1.32	3.06
Rowley	7.71	1.30	2.78
Ipswich	4.07	1.31	2.53
South	12.44	1.31	2.79

Table 2.6. 2011 LiDAR based accommodation space statistics for the delineated PIE watersheds and the respective regions.

Watershe	Area (km2)	Mean Elevation (m)	Mean Slope (°)
Merrimac	2.39	1.72	1.38
Parker	4.33	1.80	2.29
Tide	1.37	1.75	1.79
North	8.09	1.76	1.82
Tide	0.15	1.62	1.13
Rowley	2.72	1.80	2.02
Ipswich	1.19	1.88	2.78
South	4.06	1.77	1.98

Table 2.7. Intertidal area change in PIE delineated watersheds following a 100 year 1 m sea-level rise.

Watershed	2011 Area (km^2)	Accommodation Space (km^2)	Area Lost (km^2)	2111 Area (km^2)	Percent Change
Merrimack	5.56	2.39	0.33	7.62	37.05
Parker	6.01	4.33	0.40	9.94	65.39
Tide Creek 2	1.67	1.37	0.11	2.93	75.45
North Region	13.24	8.09	0.84	20.49	54.76
Tide Creek 1	0.66	0.15	0.07	0.74	12.12
Rowley	7.71	2.72	0.96	9.47	22.83
Ipswich	4.07	1.19	0.35	4.91	20.64
South Region	12.44	4.06	1.38	15.12	21.54

Table 2.8: Current and future (in parentheses) saltmarsh vegetation cover by PIE delineated watershed and region.

Watershed	*S. alterniflora* (km^2)	*S. alterniflora* %	*S. patens* (km^2)	*S. patens* %
Merrimack	0.98 (7.48)	17.63 (98.16)	4.58 (0.14)	82.37 (1.84)
Parker	0.96 (9.57)	15.97 (96.28)	5.05 (0.36)	84.03 (3.62)
Tide Creek 2	0.25 (2.82)	14.97 (96.25)	1.42 (0.11)	85.03 (3.75)
North Region	2.19 (19.87)	16.54 (96.97)	11.05 (0.62)	83.46 (3.03)
Tide Creek 1	0.19 (0.73)	23.79 (98.65)	0.47 (0.01)	63.51 (1.35)
Rowley	2.44 (9.20)	31.65 (97.15)	5.27 (0.27)	68.35 (2.85)
Ipswich	1.15 (4.75)	28.26 (96.74)	2.92 (0.16)	71.74 (3.26)
South Region	3.78 (14.67)	30.39 (97.02)	8.66 (0.45)	69.61 (2.98)

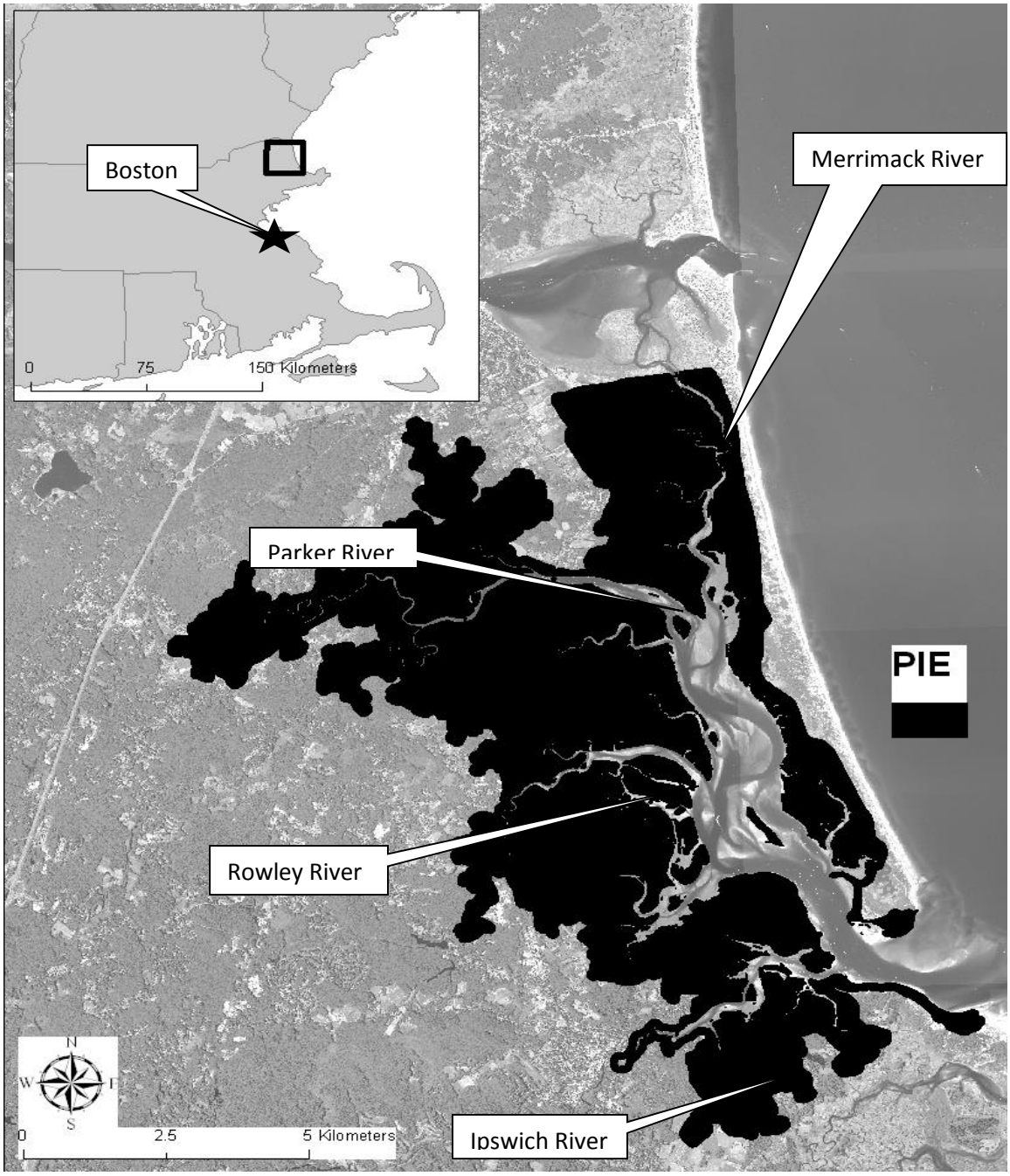

Figure 2.1. Location of the Plum Island Estuary Long Term Ecological Research Reserve (PIE-LTER) in coastal northeastern Massachusetts in relation to the region's major city, Boston, MA

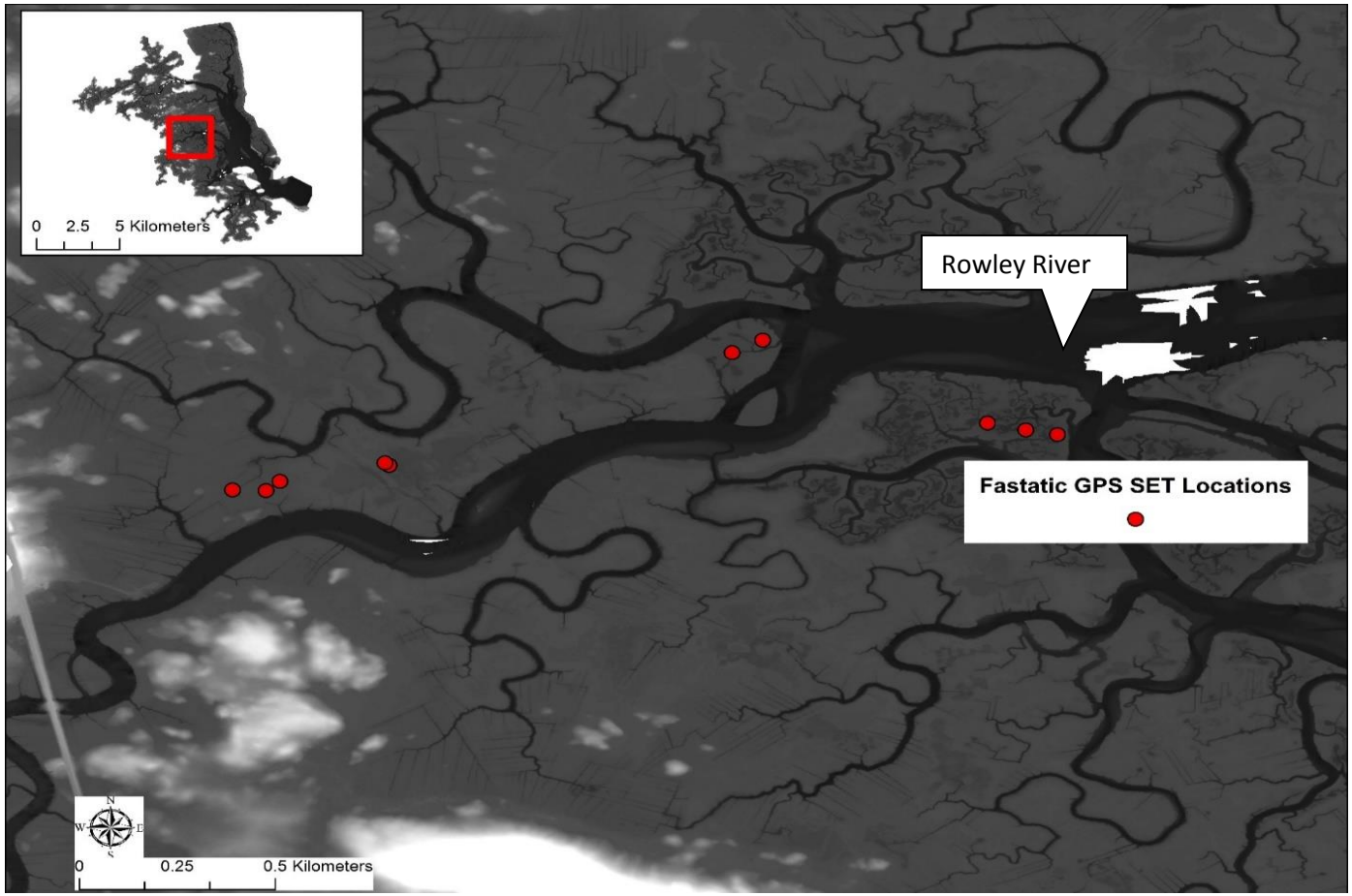

Figure 2.2. Location of 13 Fastatic GPS measured SET sites within PIE overlain 2011 LiDAR.

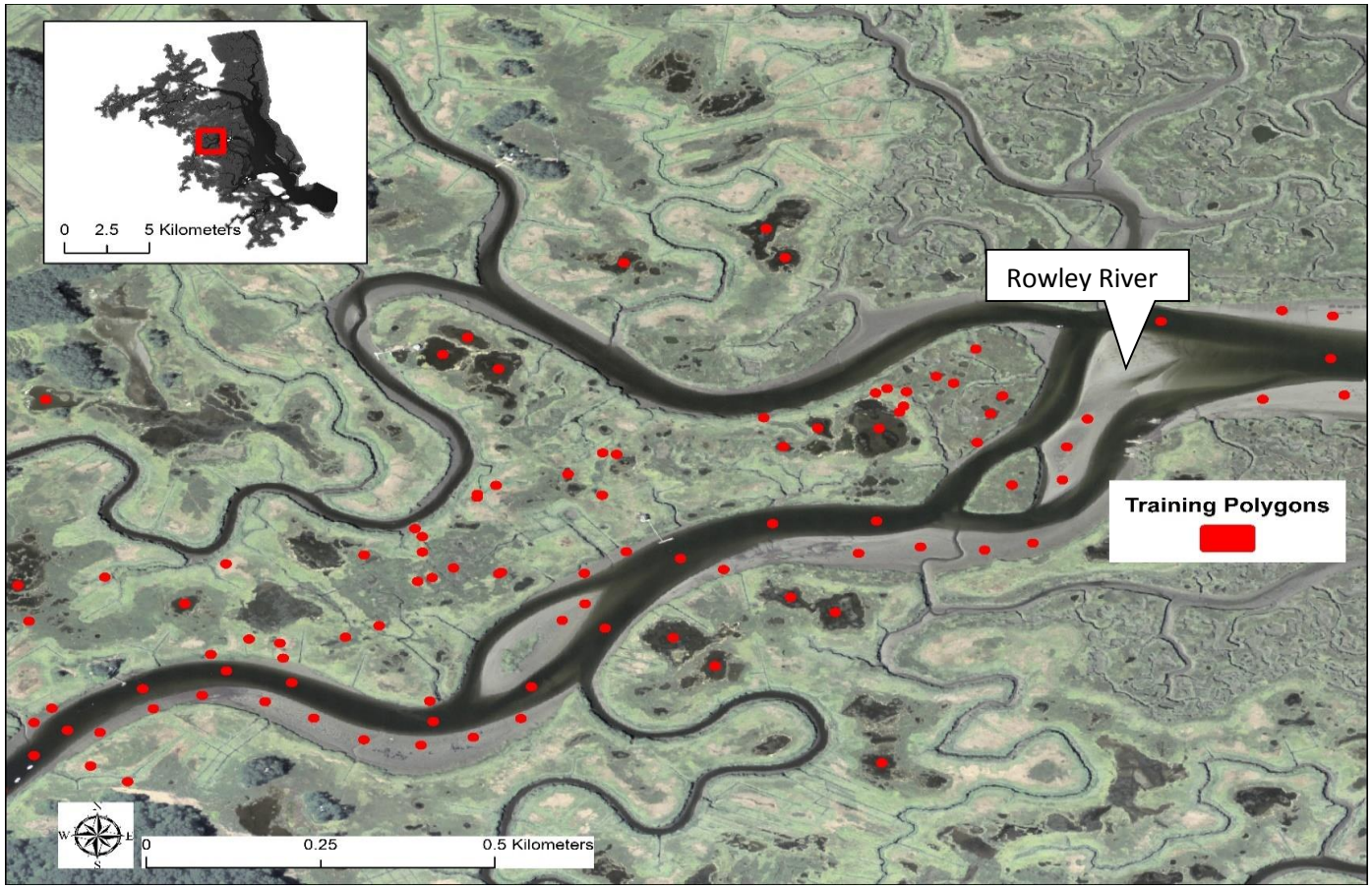

Figure 3.3. Example of training polygons located around the Rowley River overlain 2010 NAIP true color.

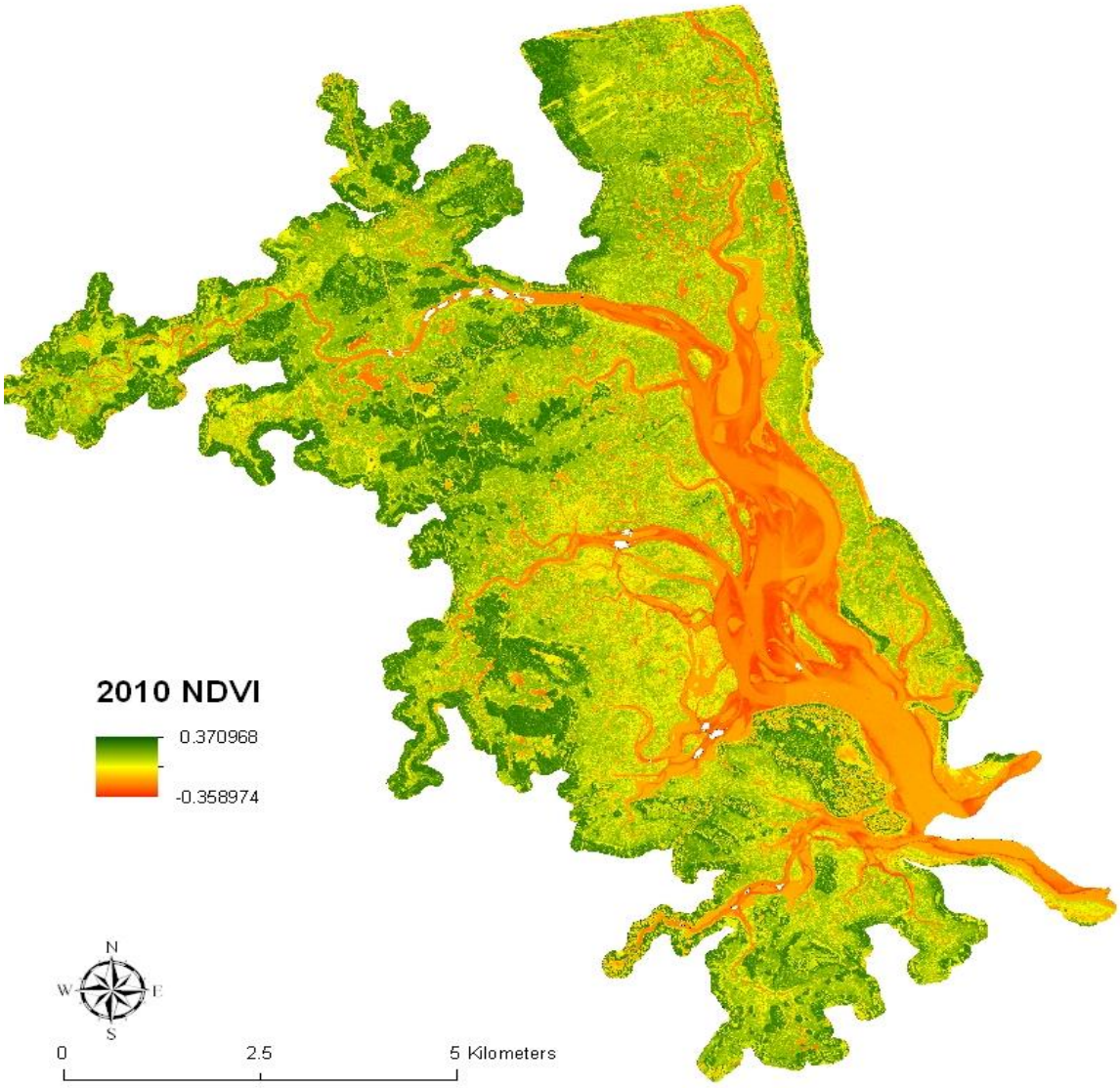

Figure 2.4: 2010 NAIP derived NDVI (unitless).

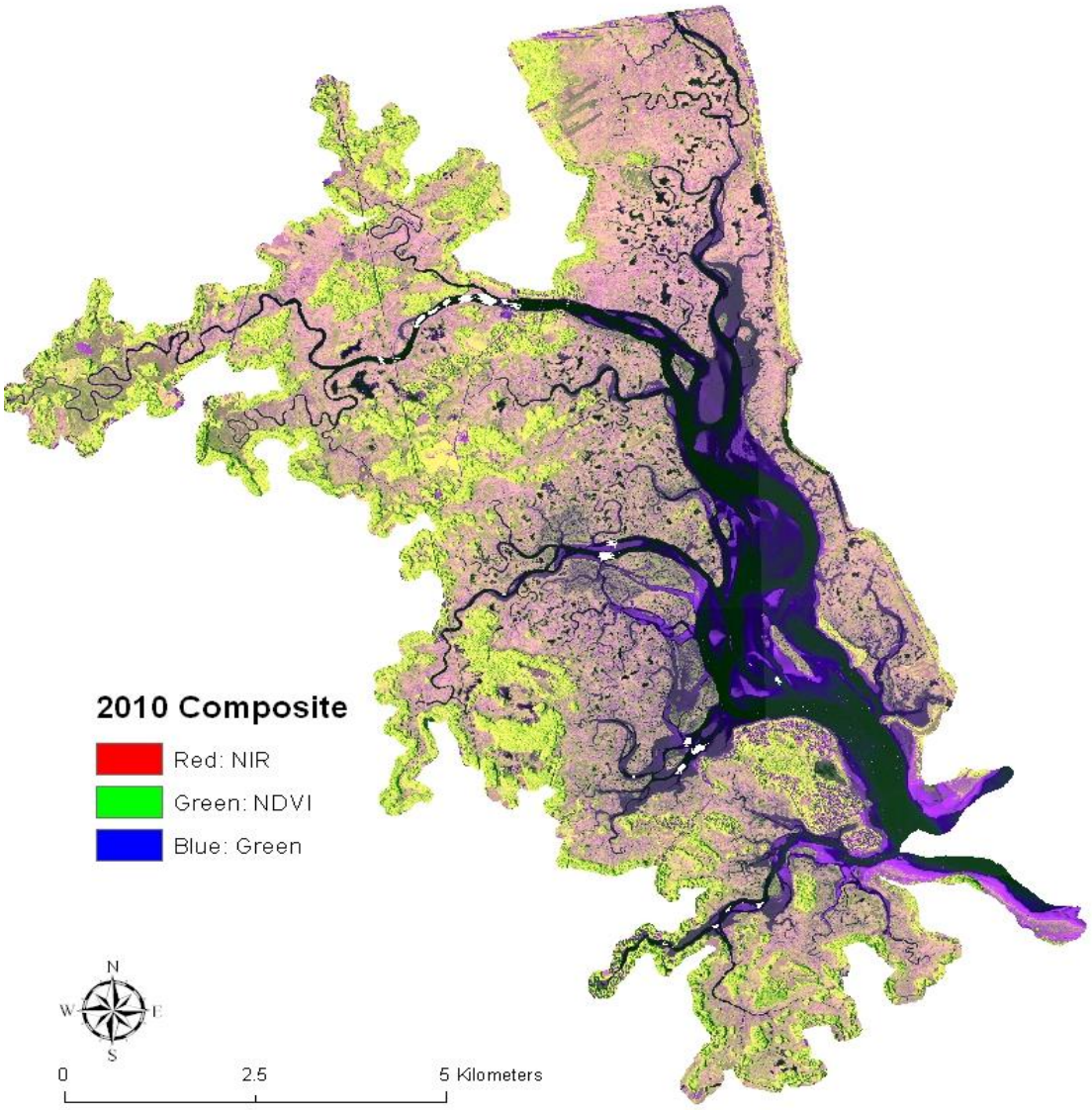

Figure 2.5: Vegetative composite image of PIE.

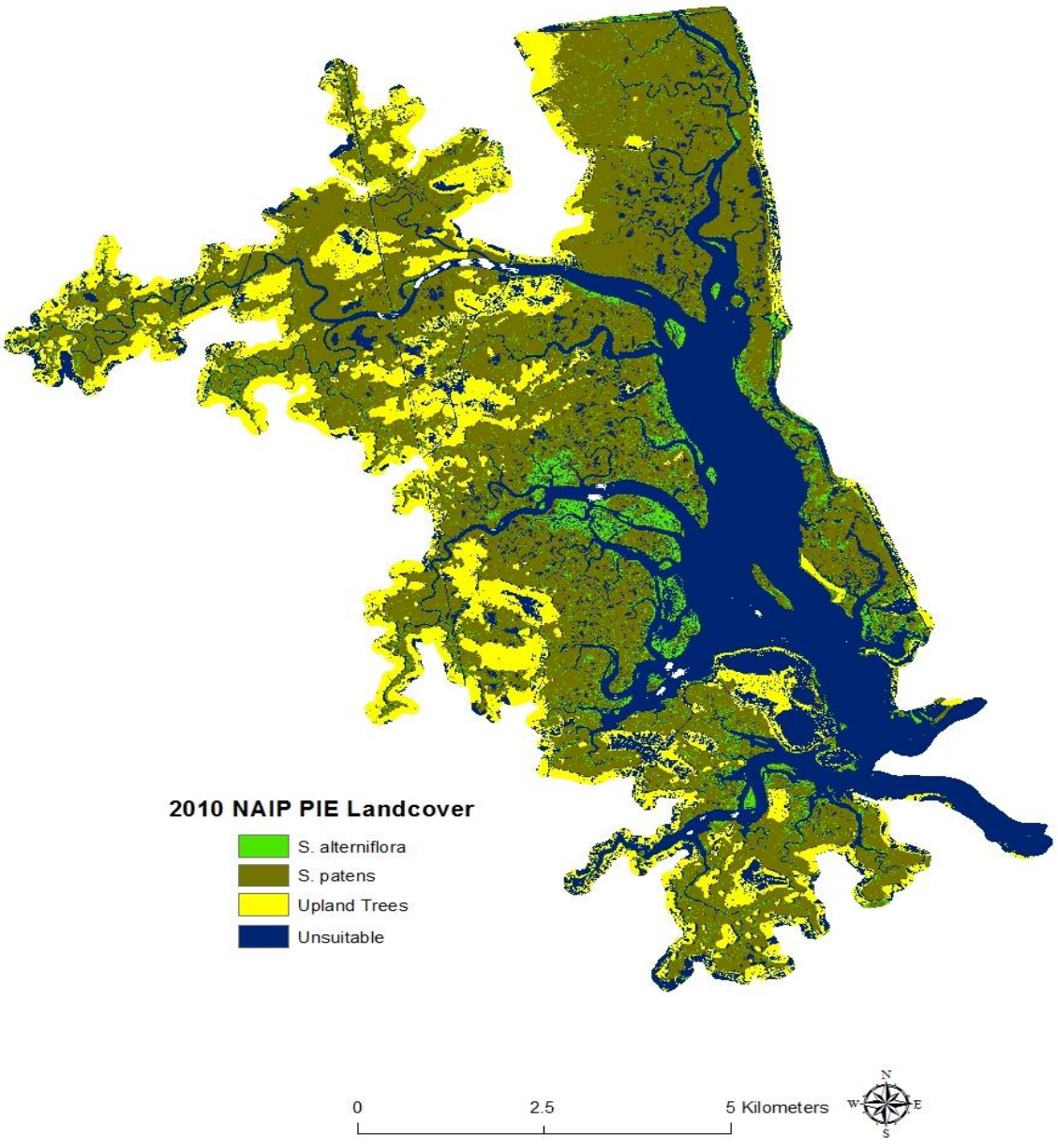

Figure 2.6. 2010 NAIP PIE land cover classification.

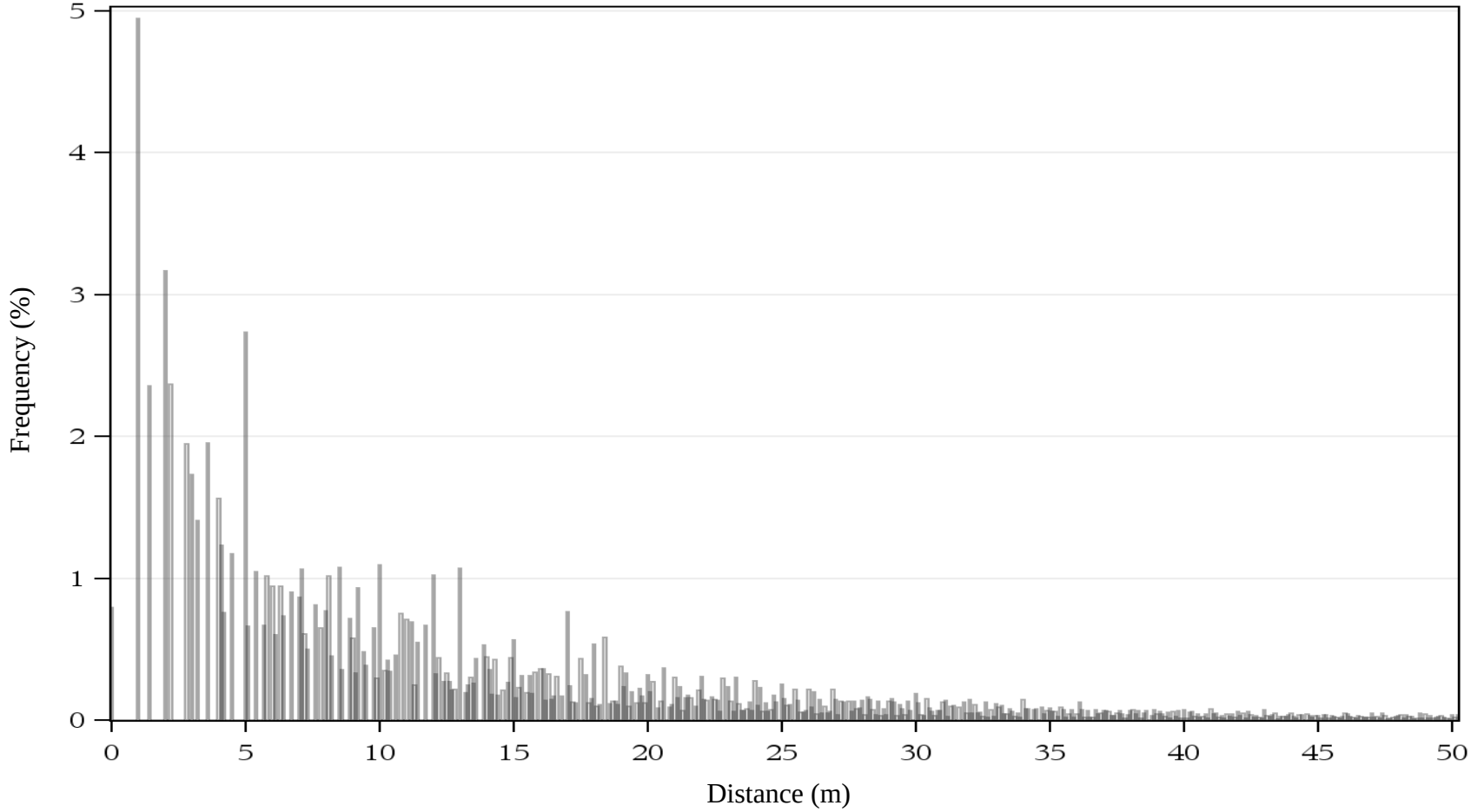

Figure 2.7. Raw classified *S. alterniflora* histogram of distance (m) to nearest hydrological feature.

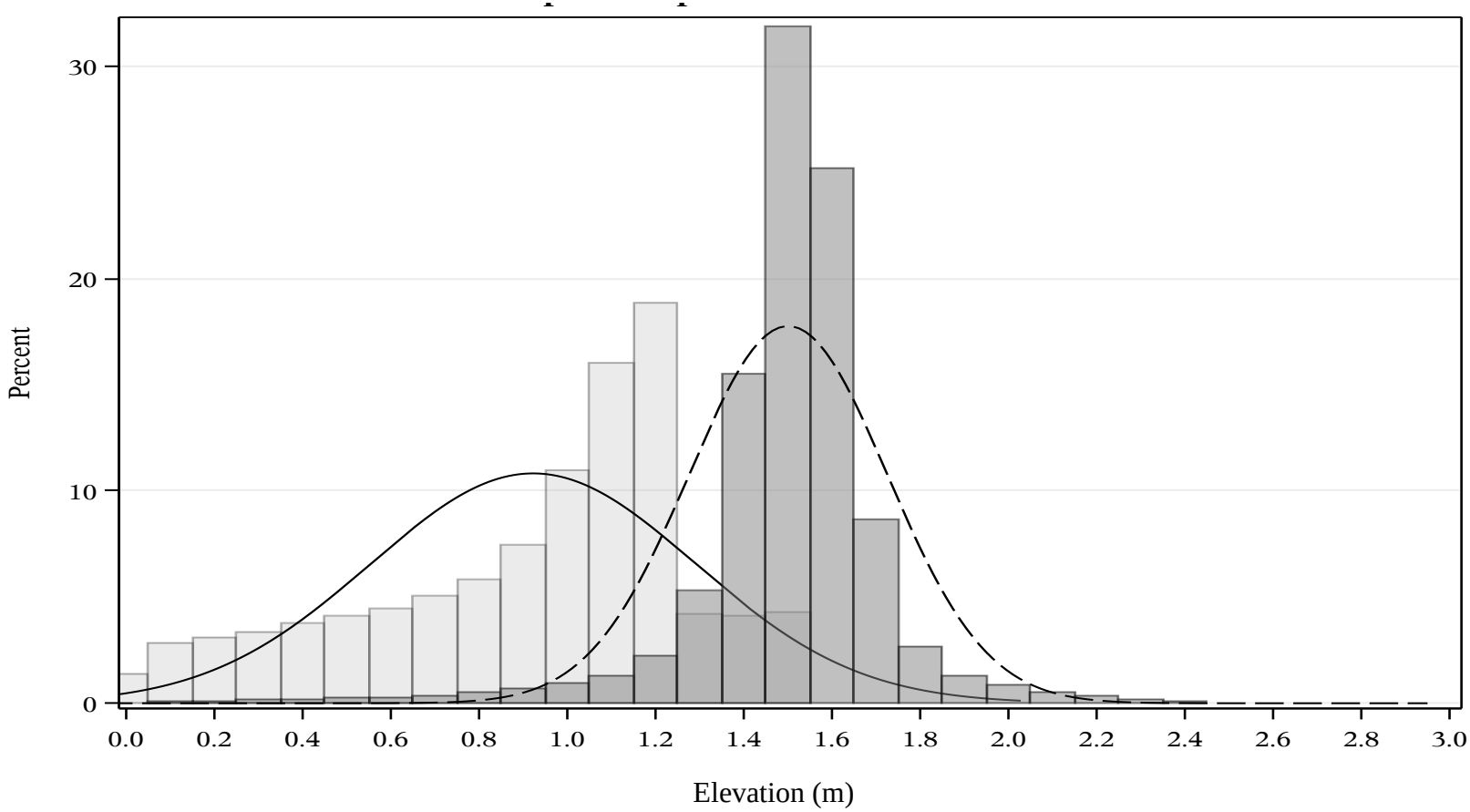

Figure 2.8. 2011 LiDAR Elevation histogram for classified *S. alterniflora* (light shading; solid line) and *S. patens* (dark shading; dashed line) after thresholding distance to nearest hydrological feature.

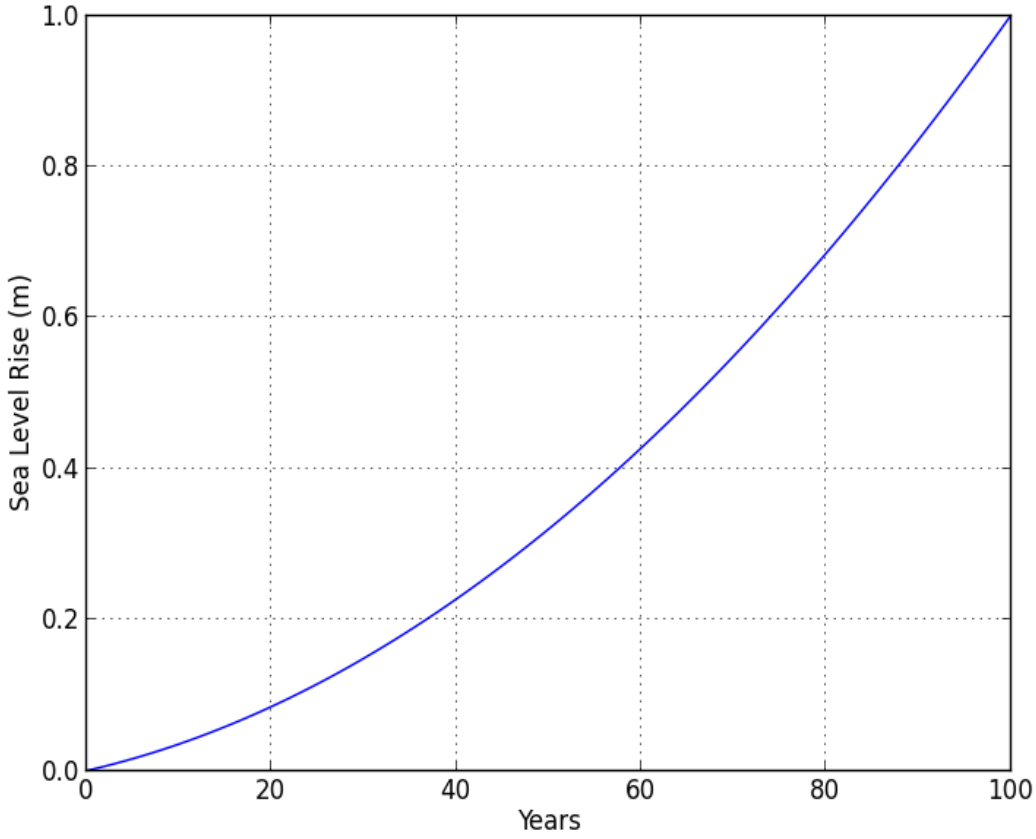

Figure 2.9. 100 year accelerating 1 m sea-level rise.

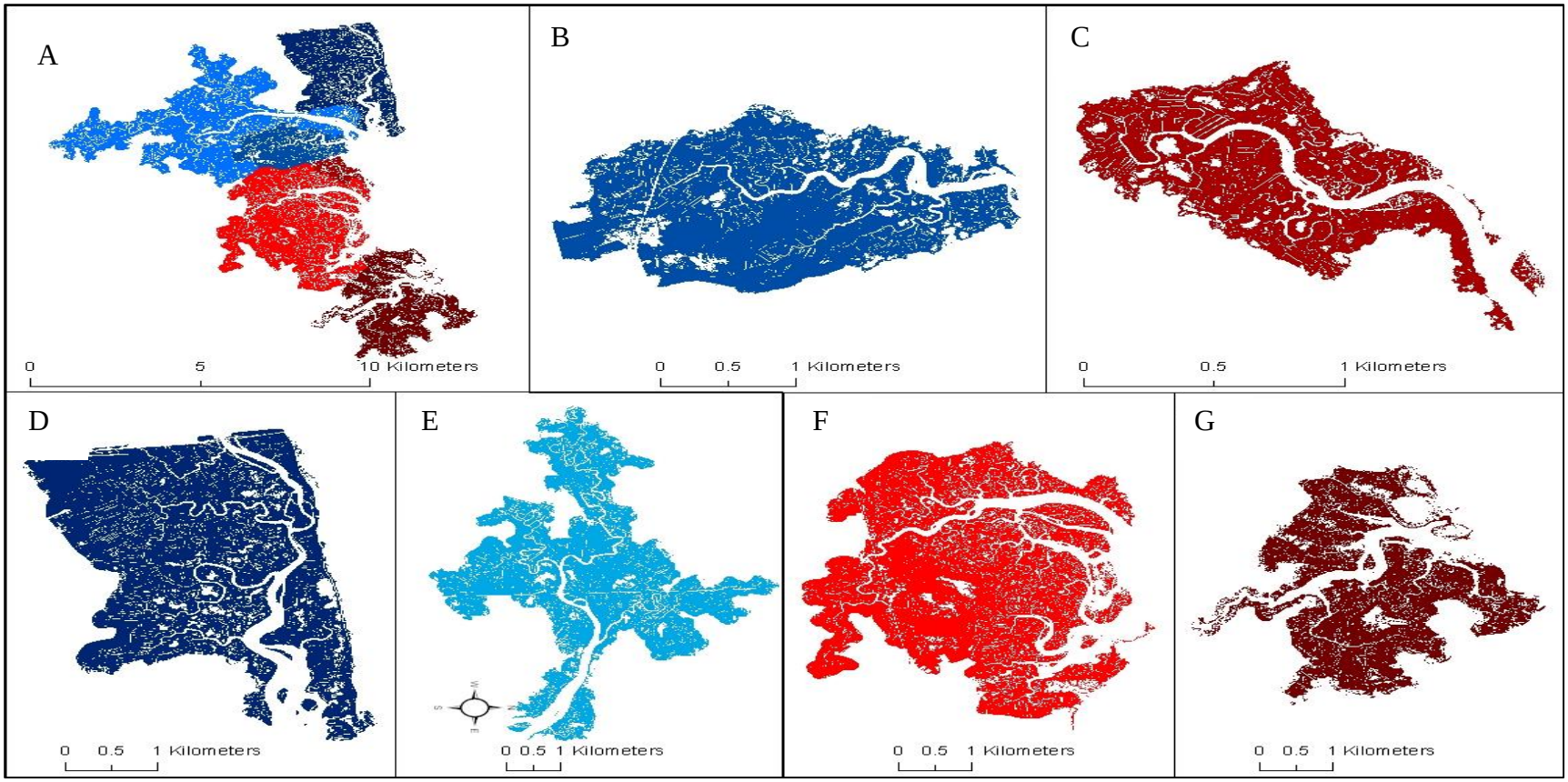

Figure 2.10: Final watershed boundaries and grouping by region. Panel (A) depicts the location of the watersheds within the western boundary of PIE. Blues denote the northern defined watersheds vs. reds defining the southern defined watersheds. Tide creek 2 (B) and 1 (C) are defined as receiving and draining a single large multi-order tidal creek. Panels D-G represent PIE's connection to the Merrimack River through Plum Blush Creek, the Parker River watershed rotated 90°, Rowley River, and Ipswich River respectively. All unsuitable landcover for marsh conversion has been removed.

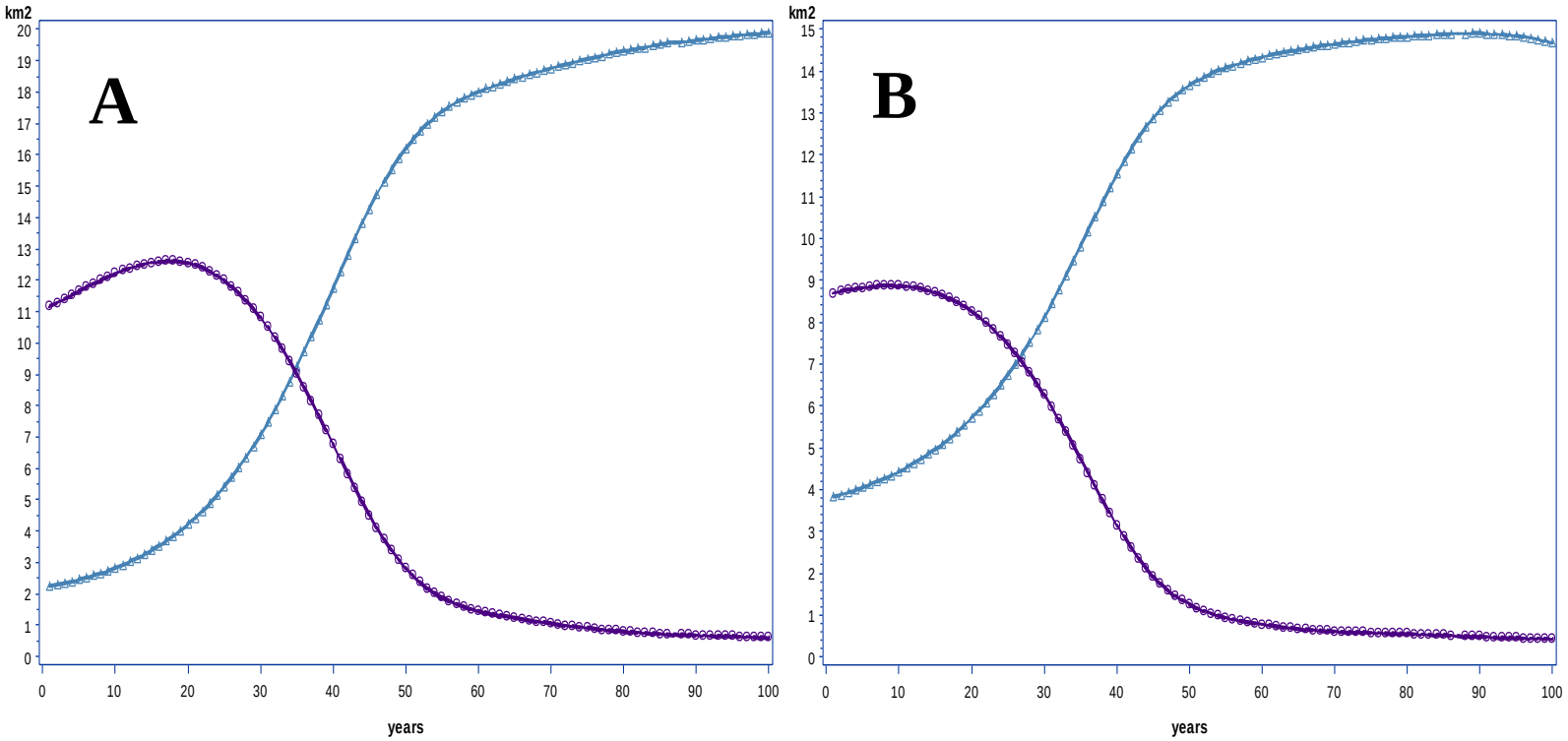

Figure 2.11. 100 year PIE vegetation change in species area by region (North = A, South = B) during an accelerating 1m SLR (purple circles denote *S. patens* vs blue triangles representing *S. alterniflora*).

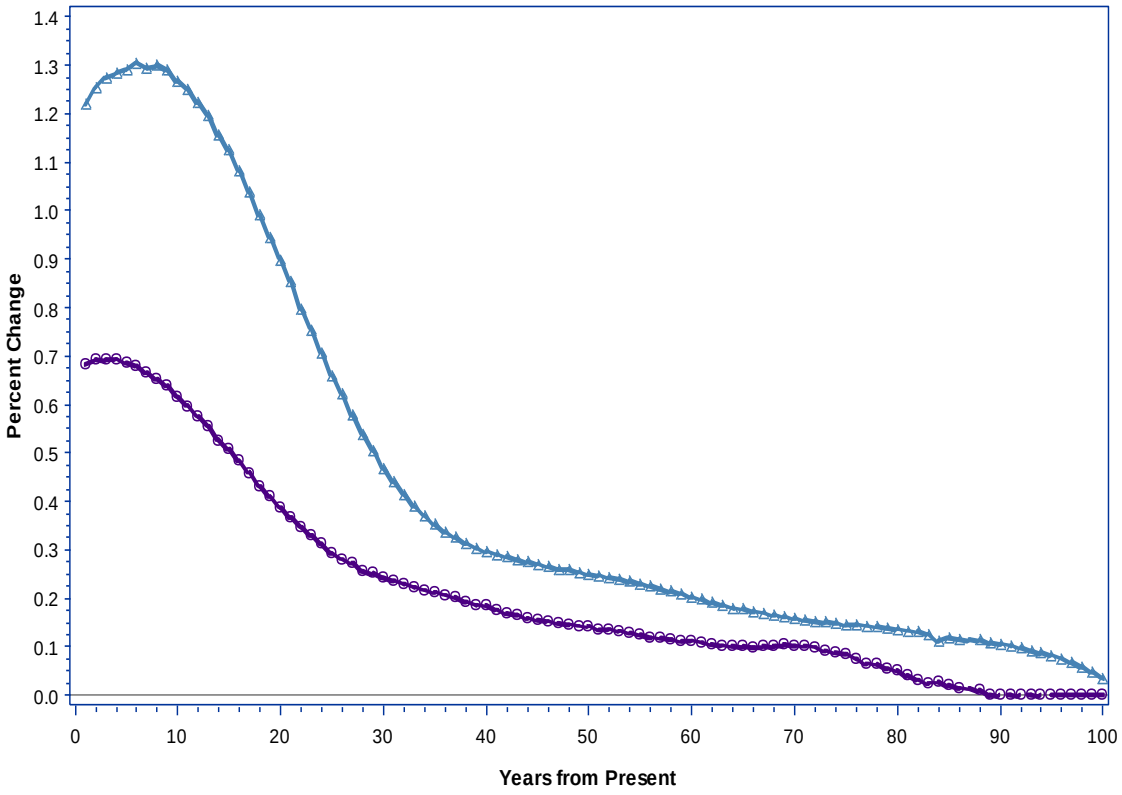

Figure 2.12. Rate of change in intertidal area above MSL per year by PIE region (purple circles denote PIE south vs blue circles representing PIE north).

Chapter 3. Mapping Future Intertidal Landscapes through the Use of a Spatially Coupled Vegetative Feedback Model, MEM3D.

The spatial redistribution of saltmarshes manifested by projected rates of sea-level rise is an important component of assessments of saltmarsh vulnerability and resilience, natural resource management, and property selection by numerous stakeholders. The purpose of this chapter is to predict changes in elevation and migration of the saltmarsh at North Inlet, South Carolina, by developing a spatial model based on the zero-dimensional Marsh Equilibrium Model (MEM) of Morris et al. (2002).

Until recently, models of the effect of sea level rise in marshes predict only changes in boundaries of marshes as a result of only the change in water levels through time (Gesh et al. 2009; Temmerman et al. 2004; Wu, Najjar, & Siewert 2009), and neglect to incorporate the vegetative feedback that contributes to the vertical accretion of the surface in saltmarshes (Craft et al. 2008; Stralberg et al. 2011). The ubiquitous Sea-Level Affecting Marshes Model (SLAMM) incorporates a steady state accretion term that is a function of wetland classification type (Craft et al. 2008), resulting in a biased, unrealistic estimate of the surviving saltmarshes. Several zero-dimensional models of saltmarsh evolution incorporate parameters that accommodate non-linear feedback mechanisms between vegetation and surface elevation changes (Kirwan et al. 2010; Kirwan et al. 2012; Krone 1985, Morris et al. 2002; Mudd, D'Alpaos, & Morris 2010),

including the MEM (Morris et al. 2002). Throughout its existence the MEM has undergone several mutations based on the increasing availability of empirical datasets, each mutation improving the ability of MEM to accurately predict future elevations based on sea level rise rates. The MEM in its current form includes parameters for biomass distribution across elevation and sediment trapping efficiency, inorganic and organic suspended sediment concentrations, sediment organic content, tide datum and frequency, and rate of sea level rise.

This study focuses on developing the spatial version of MEM for several reasons. First, the MEM was developed using one of the longest time series of observations for biomass and accretion and therefore has a strong theoretical basis for surface change in marshes as sea level rises. Second, the MEM is a series of equations that can be scripted into any programming language and is based on a single input elevation, introducing the capability of being projected across space with the use of digital elevation models. Digital elevation models allow for the use of multiple input elevations in a python program written to execute the MEM on multiple input values. As such, the MEM can accommodate pre-defined site-specific parameters of tidal datums, vegetation biomass, sediment organic content, suspended sediments in the water column, and rate of sea level rise. The adaptability of MEM coupled with the spatial power of a geographic information system (GIS) conveys the production of a single model capable of projecting MEM across space.

The goal of this study is to develop a spatial version of MEM that predicts changes in elevation throughout a pre-defined area in order to understand the spatial dynamics of marsh evolution and migration during the unprecedented sea level rise that is

predicted for the upcoming century. The spatial version of MEM automates the computational processes in a single python program so that the only user interactions are specifying input data and manipulating output for deliverables. The specific objectives of the study are to 1) develop a computationally affordable MEM model to avoid back and forth transfers of data between programs; 2) suggest an optimal input DEM resolution that balances aesthetics, processing time, and quantitative output; 3) apply the developed model to analyze the spatial transition of saltmarshes of the North Inlet estuary; and 4) provide evidence for what the future landscape composition of North Inlet will consist of and when major changes will occur.

Methods

Study Site

The study site is the North Inlet-Winyah Bay National Estuarine Research Reserve (NI-WB NERR, Figure 3.1) located east of Georgetown, South Carolina. The NI-WB NERR contains several undisturbed major coastal habitats ranging from upland longleaf pine savanna to an extensive and stable, high salinity marsh-estuary complex dominated by *Spartina alterniflora*. The complex is meso-tidal with an average MHW range of 0.64 m reported from NOAA tide gauge 8662245 (NOAA Tides and Currents 2013d). Hydrologic input to the system is dominantly from the Atlantic Ocean through North Inlet. Freshwater input is from the Waccamaw River through Winyah Bay to the south but is a minor component of the hydrologic input.

Model Scripting

The three-dimensional Marsh Equilibrium Model (MEM3D) was written in the python programming language to allow for loose coupling of the parent model, MEM, with the spatial modeling power of Earth System Research Institute (ESRI) ArcMap. Input data consisted of two datasets and 22 variables stemming from four classes. The two input datasets were a raster representing a bare Earth LiDAR digital elevation model (gDEM) and a shapefile representing the boundary of the area of interest (mask). These datasets were defined as input datasets in the script. The four classes of variables were used to define batch size, tidal parameters, sea-level rise, and biological growth characteristics of the saltmarsh grass *S. alterniflora*. Batch size (N) was defined as the number of records the computer processed per iteration. Tidal parameters were the elevation, in meters, of mean high water (MHW), mean low water (MLW), and the tidal range (Trange). Sea-level rise variables were defined as total global sea-level rise (gSLR), in cm, the model simulation time in years (T), and the current rate of SLR (A), in cm, as inferred from the nearest tide gauge. An additional variable, B, representing an acceleration term in Equation 3.1, was calculated by the model and used as input.

$$\text{gSLR} = AT + BT^2 \qquad 3.1$$

Biological growth (Equation 3.2) consisted of 3 coefficients (a, b, and c) derived from the relationship between *S. alterniflora* biomass and absolute depth (D; Equation 3.3) below MHW described by Morris et al. (2002).

$$\text{Biomass } (BM) = \text{maximum } ((a*D + b*D^2 + c), 0) \qquad 3.2$$

$$\text{Depth } (D) = (MHW - \text{elevation}) / (Trange) \qquad 3.3$$

Five additional coefficients (q=0.9 g/g, k_r=0.05 g/g, m=21e-6 g/cm^3, k_1=0.088 g/cm^3, and k_2=1.91 g/cm^3) were provided by Morris (personal communication) to define sedimentation properties and loss on ignition. Minimum and maximum vegetated elevations (MinE and MaxE) were calculated by solving the roots of the biomass parabola and re-arranging Equation 3.3 for elevation. A final variable, fE, representing the maximum elevation needed for model simulation, was calculated as the maximum vegetated elevation plus the total SLR. An array was created to hold time in years from the current time (T=0) to the end time plus 1 (T+1). Sea-level rise was simulated in a for-loop that incremented MSL yearly by inserting the iteration number (i) in place of T in Equation 3.1. The magnitude of change in MSL, ySLR, between years was calculated as the difference between the latter and prior year's location of MSL and stored in the array.

The script for MEM3D contains several different processing steps. The first step is to reduce the total amount of data necessary for processing and thus reduce the total processing time. This is done by removing data outside the area of interest and the data that will not experience any change in elevation because it exists above the maximum elevation for vegetation at the end of the study period. The input DEM was clipped to the input boundary mask and then reclassified to represent all potentially vegetated elevations during the SLR event. The reclassification produced two classes – one for elevations between the minimum vegetated elevation (minE) for *S. alterniflora* productivity and the maximum elevation for model simulation (fE) (given a value of 1) and all other elevations (given a value of 0).

The second step was to convert the spatial data to a text format that was input into the MEM3D. A raster to point tool in ArcPy, a module that connects ArcGIS to Python,

converted the raster data to point data with Cartesian coordinates representing the center of the raster and an elevation value for each cell. The result was the creation of a text file for input into MEM3D.

The third step in the script, and the most complex step, was the creation of multiple statements and nested for-loops to execute the equations that constitute the MEM. An initial 'with open' statement was employed to create a CSV file where all MEM output was permanently stored. Two empty dictionaries, E and E0, were created to temporarily store MEM input and output respectively. The dictionary 'E' was used to store the raw data columns as tuples with a unique key assignment set as the point's Cartesian coordinates to serve as a spatial identifier. The dictionary 'E0' was used to store temporal data separately from the raw input data.

To avoid memory errors, a primary for-loop was used to obtain a number of records equal to the defined batch size for processing. All the remaining calculations for the MEM portion of the script were contained within this primary for-loop. A secondary nested for-loop was used to process each record of the batch into specific columns for longitude, latitude, and elevation. Input elevation was converted to cm to match the units of the input variables. A column for depth (D) was created to store unitless depth defined by Equation 3.3. Biomass (BM) was calculated from Equation 3.2 to represent the *S. alterniflora* above-ground standing biomass in $g/cm^{2.}$

An additional secondary nested for-loop was used to create an array with length equal to the time of the SLR event, 100 years in this study, and assign year 0 elevation, biomass, and the spatial identifier to a variable from the raw input dictionary. A tertiary nested for-loop was used to calculate elevation and depth for each spatial identifier over

time. Elevation (Z) at each time step (1 year in this study) was updated as described by Equation 3.4 through a combination of variables calculated from the previous year culminating in an accretion (DEDT) value (Equation 3.5) where *f* is the frequency of semi-diurnal tides per year. Absolute depth (absD) was calculated and set to a minimum of 0 m as described by Equation 3.6.

$$Z_{[t]} = [Z_{[t-1]} + (DEDT - ySLR_{[t]})] \quad 3.4$$

$$DEDT = (q*m*f*(D_{real}/2) + kr*B)*[LOI/k_1 + (1-LOI) / k_2] \quad 3.5$$

$$absD = \max(MHW - \text{elevation}, 0) \quad 3.6$$

Real depth (D_{real}) was initially set as equal to absolute depth and updated to the depth of MLW if the calculated elevation was below MLW. This constraint was created to limit elevation change in areas below which marsh vegetation cannot exist, i.e., elevations that are known to be mudflats based on empirical biomass distribution curves. Biomass was set to a minimum of 0 g/cm^2 to avoid erroneous calculated values. Loss on ignition (LOI) was set as 0.1 and updated as described by Equation 3.7 if the calculated biomass was greater than 0 g/cm2.

$$LOI = (k_r*B/(q*m*f*(absD/2) + k_r*B) \quad 3.7$$

Limits were placed on the real depth and biomass to avoid negative accretion values. A remainder function was employed to export temporal elevation and biomass to dictionary 'E0' by a 10 year interval. The product of these calculations was a CSV file with columns for biomass and elevation for each point at the specific time intervals, i.e., year 0, year 10, year 20, …., year 100. Ten years was chosen as the temporal interval to reduce memory constraints associated with storing files.

The final steps in the script were spatial processing procedures to create a point shapefile from the MEM output data. The point file was interpolated with the same cell size as the original input DEM and using the natural neighbor interpolation algorithm (a common interpolation method for LiDAR data). Final output DEMs were clipped to the extent of the potentially vegetated mask previously developed.

Several constraints were placed on terms and equations within the script to ensure that the model output was realistic. Change in elevation (Equation 3.5) is a function of mineral and organic components and controls the magnitude of loss within the simulation by offsetting the loss in elevation due to SLR. The maximum expected loss in elevation during the event was expected to be 1 m. Within the python script, if the magnitude of depth becomes too large, it can dominate the entire amount of accretion resulting in substantial errors for subtidal elevations to a point where new intertidal land would be encountered during the simulation, an unrealistic outcome. On the other end of the tidal prism, if depth is calculated as negative, or above the elevation of MHW, accretion would become negative thereby representing erosion. To adjust these errors, depth was limited to a maximum value to that of MLW and 0cm for all elevations above MHW. The organic component is controlled by *S. alterniflora* above-ground biomass, which has set values between 0 and 0.0928 g/cm^2 for NI-WB. Values for the pure organic (k_1) and inorganic (k_2) coefficients for the calculation of LOI were empirically derived by Morris and set at 0.088 and 1.9 g/cm^3 respectively. At elevations beyond the thresholds for vegetative production, LOI was set to a value of 0.01 to realistically include a minor portion of organic material. The limits imposed on depth, biomass, and LOI ensured that accretion occurs only within vegetated and intertidal elevations. The inclusion of these

constraints meant that testing of the Python script was necessary to verify that the code was written to produce the intended output.

Finally, in addition to creation of the script to run MEM3D, differences between input data spatial resolution were analyzed to determine the optimal resolution that save time but do not result in any loss of information. To provide alternative resolutions for analysis, the 1 m resolution DEM from 2007 (year 0) was aggregated to 5 m and 10 m by averaging. A processing timer was included in the script and began counting at the start of each MEM3D execution and stop at the conclusion of the final interpolation to track time to completion. The point shapefile for the 1m DEM, created by MEM3D, was imported into ArcMap to join the elevation of the 5m and 10m raster into a single tabular dataset. The dataset was loaded into SAS where change in elevation was calculated as the difference between the 1m elevation and each aggregated elevation. Descriptive statistics were produced to define the shape of each change in elevation frequency distribution. Area for each resolution was determined by multiplying the number of cells within the dataset by the cell area for the specific resolution. Maps for each resolution were compared and inspected for presentation quality aesthetics. The modeled extent of the optimal resolution for North Inlet-Winyah Bay was processed within SAS to provide spatial changes in the saltmarshes of the estuary during the SLR event. Biomass was summed for each 10 year iteration to create a total biomass variable.

Model Processing at North Inlet

North Inlet-Winyah Bay was chosen as the estuary to model a 100 year 1m SLR event. Several site-specific parameters were used in the application of MEM3D at North Inlet-Winyah Bay. A 2007 1 m resolution LiDAR DEM referenced to NAVD88 was

obtained from NOAA through a non-disclosure agreement with the Georgetown County, SC GIS Department. The DEM was filtered and a mask drawn to approximate the boundary of the North Inlet-Winyah Bay National Estuarine Research Reserve (Figure 3.1). Saltmarsh biological growth coefficients (a, b, c), were provided by Morris (personal communication) and were 0.0766 g/cm^2, -0.313 g/cm^2, and 0.09287 g/cm^2 respectively. Tidal parameters were obtained from the Oyster Landing tide gauge located within North Inlet. MEM3D was employed to identify the appropriate DEM resolution and quantify the changes in total biomass and area of coastal land cover classification during the SLR event.

Maps for the current and the modeled 100 year estuary were produced for visual representation. The output DEMs were classified into six classes based on vegetative and tidal thresholds identified for *S. alterniflora*. Elevations below MLW were classified to represent water. Mudflat was defined as between mean low water and the minimum elevation for vegetation. Vegetated below mean sea level, or the area most likely to be devastated during sea level rise, was defined as between the minimum elevation for vegetation and MSL. The vegetated intertidal zone, the marsh area with greater biomass productivity, was defined as between MSL and MHW. Another zone between MHW and the maximum elevation for vegetation defined the limits of the vegetation zone above MHW. All elevations above the maximum vegetated elevation were defined as upland.

The total area of each class was calculated by multiplying the number of observations within each class by the raster cell area. Land cover area was plotted against time to graphically track changes in the study site. Total marsh area, defined as the sum of all vegetated zones per 10 year interval, was plotted against time to track temporal

changes in raw marsh area. The analyses described allow for the identification of spatial patterns and how overall SLR will affect the saltmarshes of North Inlet-Winyah Bay.

Results

Results show that the MEM3D model is capable of predicting spatial changes in the marsh at North Inlet during a 100-year, 1-m SLR event. Model outcomes suggest that the marsh is not capable of keeping up with sea level rise, as the amount of marsh area decreased substantially during the model duration. Furthermore, results show that there was a loss of information and computing time as a result of changing the spatial resolution for input DEMs.

Descriptive statistics were used to compare the loss of information caused by aggregating the original 1 m LiDAR to 5 m and 10 m spatial resolutions (Table 3.1). The difference in elevations between the 1 m and aggregated 5 m LiDAR ranged between -1.9 m and 2.15 m with an average of 0 m and standard deviation of 0.11 m. Skewness and kurtosis for the elevation difference of the 5 m resolution were 0.31 and 25.54 respectively. Differences in elevation between the 1 m and the 10 m LiDAR were between -2.17 m and 2.53 m with a mean and standard deviation of -0.01 m and 0.18 m respectively. Skewness and kurtosis for the 10 m resolution were 0.43 and 17.06 respectively. A visual comparison of the 3 LiDAR resolutions is presented in Figure 3.2. The number of cells, associated area, and time for MEM3D processing of each resolution are presented in Table 3.2. The 1 m LiDAR contains 2,825,827 cells for a total area of 2.83 km^2 compared to 114,096 cells and 2.86 km^2 for the 5m LiDAR and 29,137 cells and 2.91 km^2 for the 10 m LiDAR. Processing time is found to be 165.61 minutes, 4.73

minutes, and 1.20 minutes for the 1 m, 5 m, and 10 m LiDAR resolution respectively. Essentially, there was no loss of information in the 5 m spatial resolution and the computing time was significantly lower than the 1 m resolution data. Therefore, the 5 m resolution DEM was used in all future analyses.

In order to assess change in the saltmarsh at North Inlet, six elevation classes were developed based on input tidal datums and the *S. alterniflora* above-ground biomass parabola (Table 3.3). There were substantial changes in each elevation class between 2007 and the final modeled year, year 100 (Figure 3.3). In order to understand the behavior and dynamics of the North Inlet saltmarsh system through time, it was necessary to analyze step-wise changes in elevation classes at 10-year intervals (Table 3.4, Figure 3.4). Water is found to only exist in year 100 at 0.03 km^2. Areas classified as mudflat appeared in model year 40 at 0.01 km^2 and increased to 1.18 km^2 by year 100. The vegetated area below MSL was 0.18 km^2 at the model onset and increased to a maximum of 0.98 km^2 at the year 80 point, only to decrease to 0.71 km^2 at the model termination at year 100. The vegetated area between MSL and MHW was 1.38 km^2 in year 0 and increased to a maximum of 1.54 km^2 in years 30-40 before decreasing to 0.59km^2 in year 100. The area of *S. alterniflora* above MHW was initially 0.68 km^2 and steadily decreased to 0.35 km^2 by the model termination. Total marsh area, defined as the sum of all *S. alterniflora* vegetated land cover classes, was initially 2.24 km^2 and increased to a maximum of 2.46 km^2 before decreasing to 1.65 km^2 in year 100 (Figure 3.5). Upland area decreased from 0.62 km^2 in year 0 to 0 km^2 in year 100. Total marsh biomass for the North Inlet-Winyah Bay study site was 6.95×10^9 kg/km^2 in year 0 (Figure 3.6). Biomass

increased to a maximum of 7.09×10^9 kg/km^2 at year 30. After year 30, total *S. alterniflora* above-ground biomass decreased to 3.71×10^9 kg/km^2 at year 100.

Discussion

The development of a spatial version of the Marsh Equilibrium Model was accomplished using Python scripting and ArcGIS. The optimal input DEM resolution for the North Inlet-Winyah Bay study site that balances aesthetics, processing time, and quantitative output was 5 m. Execution of the new model, called MEM3D, shows that North Inlet-Winyah Bay will experience significant reductions in the amount of marsh area between 2007 and 2107, assuming current dynamics and sediment delivery systems remain the same.

Resolution manipulations of the input LiDAR DEM suggest that a resolution of 5m is sufficient for production of quantitative data. While the mean elevation difference between the 1 m and the 5 m and 10 m datasets is very small (0 m and -0.01 m, respectively), the minimum and maximum elevation differences is quite different (-1.9 m to 2.15 m for the 5 m resolution and -2.17 m to 2.53m for the 10 m resolution), such that the information in the 10 m resolution data is altered to a greater extent than the 5 m resolution data. It is not surprising that the mean differences in elevation are near 0m. Saltmarshes are inherently flat, with topographic relief generally occurring in the micro-scale (Tonelli, Fagherazzi, & Petti 2010). Airborne LiDAR, with low posting densities (Hopkinson et al. 2004), are too coarse to accurately depict any micro-topography. These general properties of the dataset, when coupled together, create the conditions for a low-relief DEM with similar elevations even at a 1m resolution.

Using the skewness and three standard deviations (99.7% of all observations) to identify outliers, the spread of the data and location of extreme elevation discrepancies can be identified. Skewness of the 5 m LiDAR was 0.31 while the skewness of the 10 m LiDAR was 0.43. Values for skewness indicate that the differences in elevation for each dataset are normally distributed around the mean with a slight bias towards underestimating the 1m elevation. The standard deviations indicate that while the mean differences between elevations were 0m, most of the data falls within 0.33m and 0.54m of the mean for the 5 m and 10 m resolutions respectively (Table 3.1). Outliers were identified as being outside of the 3 standard deviations and were responsible for the extreme elevation discrepancies of the minimum and mean. These outliers were located along the edges of tidal creeks and the major transition onto the upland are where these differences occur because there is a large relief over a short span (Figure 3.7). Elevations in the tidal creek and on the marsh platform are drastically different from each other; and as a result a resampled pixel covering a transition from creek to platform has an average value that does not accurately represent one or the other, but something in between. This simple condition explains the interaction between the spatial location of a cell and the influence of an edge to create large elevation discrepancies.

A final metric, kurtosis, was used to further describe the data. The 5 m resolution data (kurtosis value = 25.54) have a more spiked, leptokurtic distribution around the mean compared to the 10 m resolution data (kurtosis value = 17.06). This means that the 5 m resolution data are more concentrated around the mean of 0 m than the 10 m resolution data. Thus there is minimal loss of information in the 5 m resolution data, or the 5 m resolution data more accurately represent the 1 m resolution data than the 10 m

resolution data. Further considerations for landscape area and processing time should be considered to fully suggest an optimal input resolution.

Another consideration to suggest an optimal input resolution is processing time. Processing time is directly proportional to file size. Processing time decreased from 164.61 minutes for the 1 m resolution to 4.73 minutes for the 5 m and 1.2 minutes for the 10 m. Processing was conducted on a standard PC with 16GB of RAM, and it is assumed that similar results will occur on other systems as long as the memory and processor are similar.

The final consideration, and perhaps the most compelling for the creation of visual aids for community planner and managers, for suggesting a 5 m resolution for input into the MEM3D is the visual comparison of output data from the model (Figure 3.2). In general, an increase in resolution causes a decrease in sharpness between topographic features and a loss of information. Important topographic features in saltmarshes, which are inherently flat environments, are the tidal creeks, marsh platform, uplands, and their respective transitions. Tidal creeks are easily identified in the 1 m resolution image and exist as individual topographic features within the marsh platform. The uplands are also clearly distinguished from the marsh platform. Increasing the resolution to 5 m, the described features become more subdued but are still evident. When the resolution is increased to 10 m, the important features become completely blended, resulting in a significant loss of information and a nearly incomprehensible graphic. Tidal creeks become merge with the marsh platform at NI-Winyah Bay and are visually diminished, some disappearing. As a result, the 10m resolution is unacceptable for the production of qualitative, presentation-quality graphics.

From the analyses of aesthetics, differences in elevation, physical attributes, and processing time it is suggested that the optimal resolution to input into MEM3D is 5m. Although the optimal resolution has been determined, results of a MEM3D simulation are purely topographic unless a classification is performed.

Analysis of changes in elevation classes based on vegetative and hydrological boundaries indicates that the North Inlet-Winyah Bay estuary will shift from current *S. alterniflora* dominance to a mosaic of *S. alterniflora* and mudflat (Figure 3.3) thereby corroborating the instability of the marsh predicted by Morris et al. (2002). Based on the 2007 LiDAR DEM, saltmarshes comprised 2.24 km^2 of the 2.86 km^2 study site, or 78.32%. During the 100 year simulation, marsh area slowly increased to a maximum of 2.46 km^2, 86.01%, during year 60. The gradual increase in marsh area occurred as a result of steady SLR-induced inundation, converting 0.32 km^2 of uplands to saltmarsh, drowning 0.1 km^2 of saltmarsh drowning, and creating 0.22 km^2 of mudflat. After year 60 the area of saltmarshes rapidly declined to a year 100 minimum of 1.65 km^2 (57.69%). During this time, the remaining 0.3 km^2 of uplands became saltmarsh while 1.08 km^2 of saltmarsh were lost to mudflat for a net loss of 0.78 km^2. Year 60 represents a tipping point for the estuary. Before year 60 the saltmarsh is keeping pace with SLR by vertically accreting sediment and migrating onto newly available intertidal space provided by the inundation of uplands resulting in an expansion of marsh area. After year 60, there is no available upland for the marsh to migrate into, and conversion of marsh to mudflat dominate changes in this estuary.

Based on the parabola describing the relationship between biomass and elevation relative to MSL, there is an optimal elevation for biomass production, below which the

marsh is incapable of accreting enough sediment and producing enough belowground biomass to maintain equilibrium with sea level rise (Morris et al. 2002). Thus, it is necessary to go beyond a simple analysis of total saltmarsh area and look at categories, or classes, of elevation based on vegetative characteristics. While changes in total marsh area indicated short term SLR mitigation with an increase in total saltmarsh area, trends in the distribution of each elevation class suggest that, even in year 0, the marsh at North Inlet-Winyah Bay is not poised to maintain equilibrium with sea level rise. Of the 2.24 km^2 at year 0, it was found that the vegetated intertidal class dominates, composing 61.61% of all marsh area followed by the vegetated above MHW class at 30.35% and the vegetated below MSL class at 8%. By year 60 the vegetated intertidal and above MHW classes had decreased to 47.96% and 19.51% of the year 60 total marsh area respectively. During the same time vegetated below MSL class increased to 32.52% of total marsh area. Following the 100 year simulation, the vegetated intertidal class further decreased to 35.76% and the vegetated above MHW class marginally increased to 21.21% of year 100 total marsh area. The vegetated below MSL class increased further to 43.03%. This suggests that, although total marsh area increases for the first 60 years, inter-class transfer in area began immediately. Although upland area was converted to the vegetated above MHW class at a nearly constant rate, the gain was offset by slightly greater loss of marsh area to the vegetated intertidal class. The vegetated intertidal class gained more area from the vegetated above MHW class than it lost to the vegetated below MSL class for 40 years, at which time the trend switched and the area of the vegetated below MSL class began increasing rapidly. The switch in trend was also associated with the appearance of mudflat which exhibited an exponential shape for the remainder of the simulation.

To corroborate the loss in elevation interpreted from intra-class transfers of area, change in total biomass was plotted against time (Figure 3.6). Biomass is a function of elevation and is therefore sensitive to any changes in relative elevation. Biomass clearly demonstrated the loss of relative elevation and the effect of SLR by exhibiting the shape of a logarithmic curve. It was interpreted that when the rate of SLR was low, the loss of biomass was gradual and that as SLR accelerated, the loss of biomass followed as depth rapidly increased below the elevation of maximum biomass. Tracking changes in intra-specific transfer of area and total biomass indicated a directly proportional loss of relative elevation to MSL and the rate of SLR.

The analysis of inter-class transfer and biomass have several important meanings for the NI-Winyah Bay study site. Assessing inter-class transfer revealed the fallacy with interpreting raw changes in total marsh area. The North Inlet-Winyah Bay study system is not stable in the short term, instead the entire system lost elevation relative to MSL during every 10 year interval. The total area identified threshold of 60 years representing the switch from marsh gain to loss is delayed 20 years compared to that identified by intra-class transfer. The threshold rate of SLR that NI-Winyah Bay marshes can withstand before large downward intra-class transfers and conversion to mudflat was found to be 0.86 cm/yr using Equation 3.1. Organic carbon content of total aboveground biomass that can be sequestered from the atmosphere has been estimated to be approximately 44% from southeastern USA saltmarshes (Alexander & Robinson 2006; Craft, Seneca, & Broome 1991; Gallagher 1975; Osgood & Zieman 1993; Tyler 1997). Assuming this percentage, the sequestration of carbon will decrease from a 2007 level of 30.6 tonnes to 16.34 tonnes by 2107, a reduction of 46.6%. The end result of a 100 year 1

m SLR event for North Inlet-Winyah Bay will be a rapid ecosystem conversion from current saltmarsh dominance to one characterized by numerous mudflats once the rate of SLR exceeds 0.86 cm/yr.

Conclusion

The initial version of MEM3D has been demonstrated to meet the objectives of this study. The model is written in the freely available Python programming language with only a single external software license needed – ArcGIS. Input spatial data is kept to a minimum of any freely available LiDAR dataset and an associated boundary for analysis. The model produces satisfactory landscape-scale results clearly identifying temporal transitions in coastal land cover. Results from a 100 year 1m SLR event for NI-Winyah Bay suggest the saltmarshes are migrating inland with SLR thereby expanding area. It was found that this areal expansion, however, is a false SLR mitigation as the saltmarshes are losing elevation relative to MSL within every 10 year iteration. Evidence corroborating the loss of elevation include the cascading biomass from the 2007 MEM3D interpreted value of 31,047.15 kg/km^2 to the 2107 MEM3D predicted value of 22,505.38 kg/km^2 and the downward shift in area reported from the intra-class analysis. The data indicate the saltmarshes will reach a tipping point in approximately 40 years when SLR is expected to exceed 0.86cm/year. By the end of the simulation, the estuary will shift from current saltmarsh dominance to mudflat. The result of this ecosystem shift is currently unknown but predicted to be both environmentally and economically disastrous as current fisheries collapse.

The optimal resolution for input LiDAR DEM's, assuming landscape-scale graphics, is 5 m. The resolution was found to possess the most accurate elevations (0 m mean, 0.11 m standard deviation) and area (+0.01%) when aggregated from 1m LiDAR.

Future versions of the model should focus on how the marsh is allowed to migrate, the assumption of steady states, and the effect of vegetation on elevation measurment. Marsh migration has not been addressed in the literature. Currently, all marsh evolution models assume that if an elevation is within the tolerance range for a species, then it is vegetated. Studies using 'least-cost' distance analysis are becoming more common and focus on functional landscape connectivity for the spread of a species of interest (Adriaensen et al. 2003). There must exist a certain rate of lateral expansion that a species can migrate per year given soil properties, biotic competition, and slope, to name a few. Updating MEM3D to address migration would limit the rate of lateral expansion providing more realistic results.

Steady states of tidal datum and tide channel network are interrelated within an estuarine environment and have been addressed in the literature independently. Luettich, Westerink, & Scheffner (1992) prove that the elevation of MHW is a function of bathymetry that varies across an estuary as it fills. The lunar nodal cycle has been described as an 18.6 year cycle that imposes a sinusoidal wave on the tidal amplitude (Baart et al. 2011). Channel networks have been modelled by Devauchelle et al. (2012) to be represented as a collection of paths that grow and bifurcate at specific angles with underlying topographic roughness. It can be expected that as the tidal volume grows, tidal creeks will meander and erode headword into the marsh platform (Hughes et al. 2009). This expansion would then be expected to alter the suspended sediment concentration

which would need to be updated. Adjusting these limitations will be challenging with current technology but will increase the validity of MEM3D.

Vegetation affects the model when multiple species exist and its preclusion of the true ground elevation. The current version of the model only uses coefficients calculated for *S. alterniflora*, despite other saltmarsh species existing at proximal elevations. Other species can be modeled in MEM3D with specific 'if' statements imposed on elevation when coefficients are known. Overestimates of 'bare earth' in LiDAR datasets is a common problem in densely vegetated ecosystems. Chassereau, Bell, & Torres (2011) and Montane & Torres (2006) collected dense Real Time Kinematic Global Positioning System (RTK GPS) points for Madieanna Island in North Inlet and found average vertical errors of 0.06 – 0.07 m on the marsh platform. Future work should focus on collecting biomass, RTK, and distance to creek measurements to coincide with LiDAR missions such that correction factors can be identified and modeled onto the DEM before MEM3D analysis.

MEM3D shows promise as a user friendly model with minimal expert knowledge required but much needed updates as new modeling technology in estuarine circulation and sedimentary processes are developed.

Table 3.9. Elevation difference and statistics from 1m resolution.

Resolution	Mean (m)	Standard Deviation	Skewness	Kurtosis	Minimum (m)	Maximum (m)
5m	0.00	0.11	0.31	24.54	-1.90	2.15
10m	-0.01	0.18	0.43	17.06	-2.17	2.53

Table 3.10. Input raster number of cells, area, and MEM3D processing time by resolution.

Resolution	Number of Cells	Total Area (km^2)	Time to Completion (min)
1m	2825827	2.83	165.61
5m	114096	2.86	4.73
10m	29137	2.91	1.20

Table 3.11. Land cover classification thresholds as determined by the *S. alterniflora* biomass curve.

Land Cover Classification	Min. Elevation (m)	Max. Elevation (m)
Water	< -0.76*	-0.76
Mudflat	> -0.76	-0.32
Vegetated below MSL	> -0.32	-0.01
Vegetated intertidal	> -0.01	0.64
Vegetated above MHW	> 0.64	1.25
Upland	> 1.25	2.25**

* No minimum limit on elevation

** Assumes data is limited to the value of gSLR above maximum vegetated elevation

Table 3.12. Temporal change in land cover area during a 100 year 1 m SLR event. Marsh area is defined as the sum of all *S. alterniflora* vegetated land cover classes. Biomass represents the cumulative biomass sum, output by MEM3D, of all *S. alterniflora* vegetated pixels.

	Land Cover Classification Area (km^2)							
Time (Years)	Subtidal	Mudflat	Vegetated below MSL	Vegetated intertidal	Vegetated above MHW	Upland	Marsh Area	Biomass (kg/km^2)
0	0.00	0.00	0.18	1.38	0.68	0.62	2.24	31047.15
10	0.00	0.00	0.18	1.45	0.64	0.59	2.27	30945.25
20	0.00	0.00	0.20	1.50	0.61	0.55	2.31	30662.19
30	0.00	0.00	0.25	1.54	0.57	0.50	2.36	30084.03
40	0.00	0.01	0.34	1.54	0.53	0.44	2.41	29224.11
50	0.00	0.05	0.53	1.40	0.50	0.38	2.43	28275.0
60	0.00	0.10	0.80	1.18	0.48	0.30	2.46	26573.38
70	0.00	0.20	0.91	1.06	0.46	0.23	2.43	24658.64
80	0.00	0.42	0.98	0.88	0.43	0.15	2.29	22774.85
90	0.00	0.90	0.81	0.69	0.39	0.07	1.89	23298.89
100	0.03	1.18	0.71	0.59	0.35	0.00	1.65	22505.38

Figure 3.13. Approximate boundary of the North Inlet-Winyah Bay NERR overlain natural color 8-bit imagery.

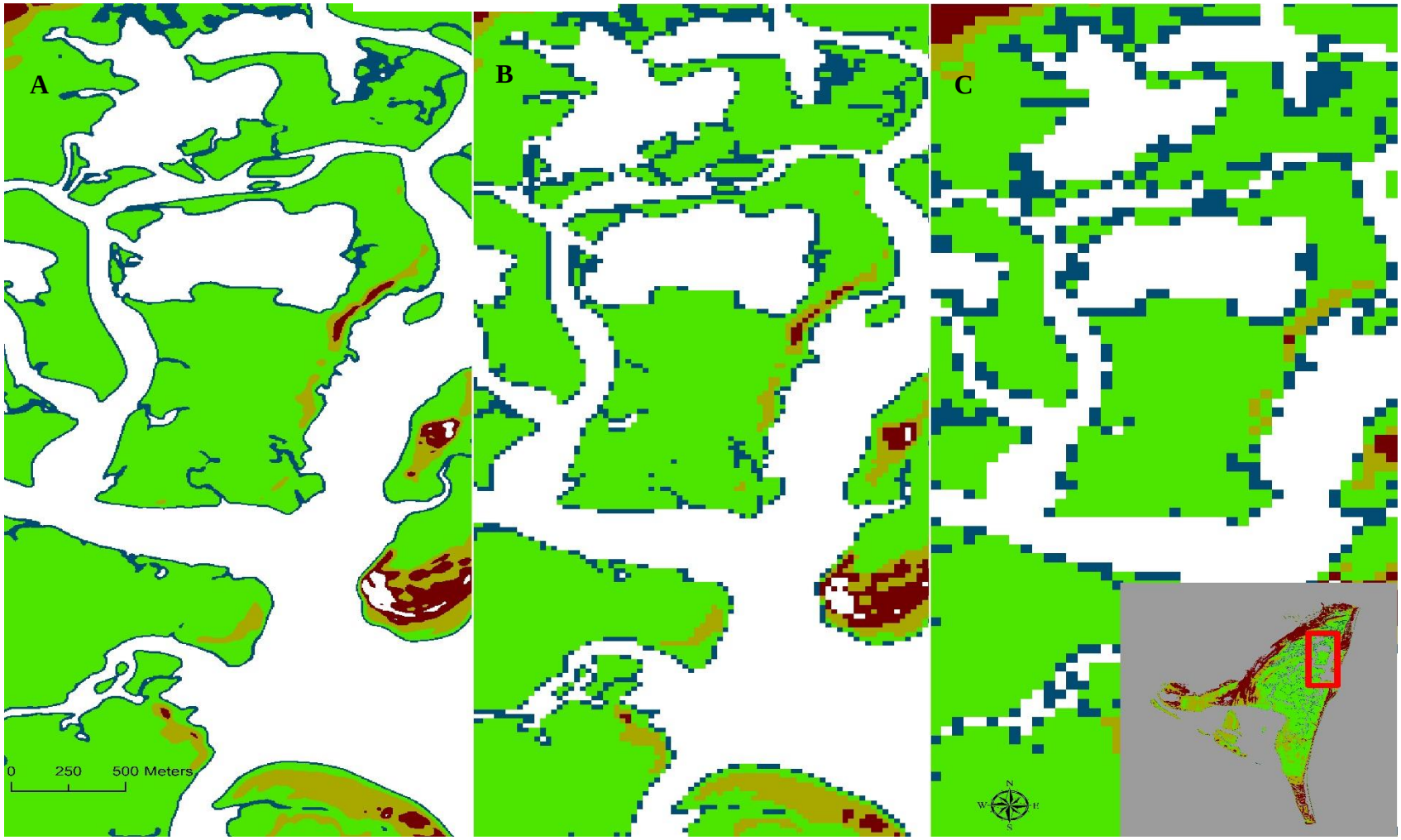

Figure 3.14 Zoomed in 1:15,000 scale comparison of the 3 LiDAR resolutions. Resolutions are ordered 1 (A), 5 (B), and 10 m (C) respectively.

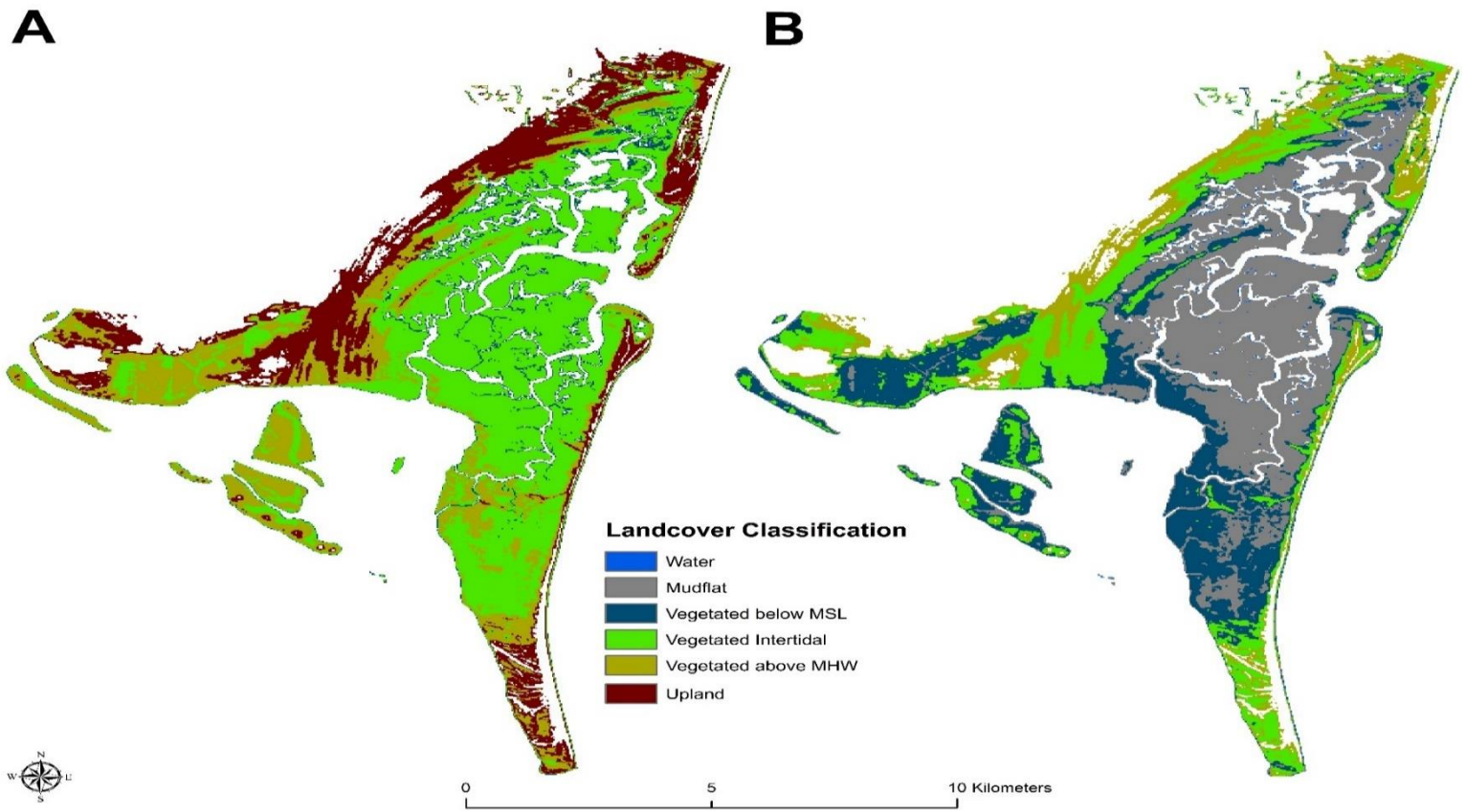

Figure 3.15. Comparison of current, year 0, 5 m resolution classified LiDAR (A) to MEM3D year 100 5 m resolution classified output (B).

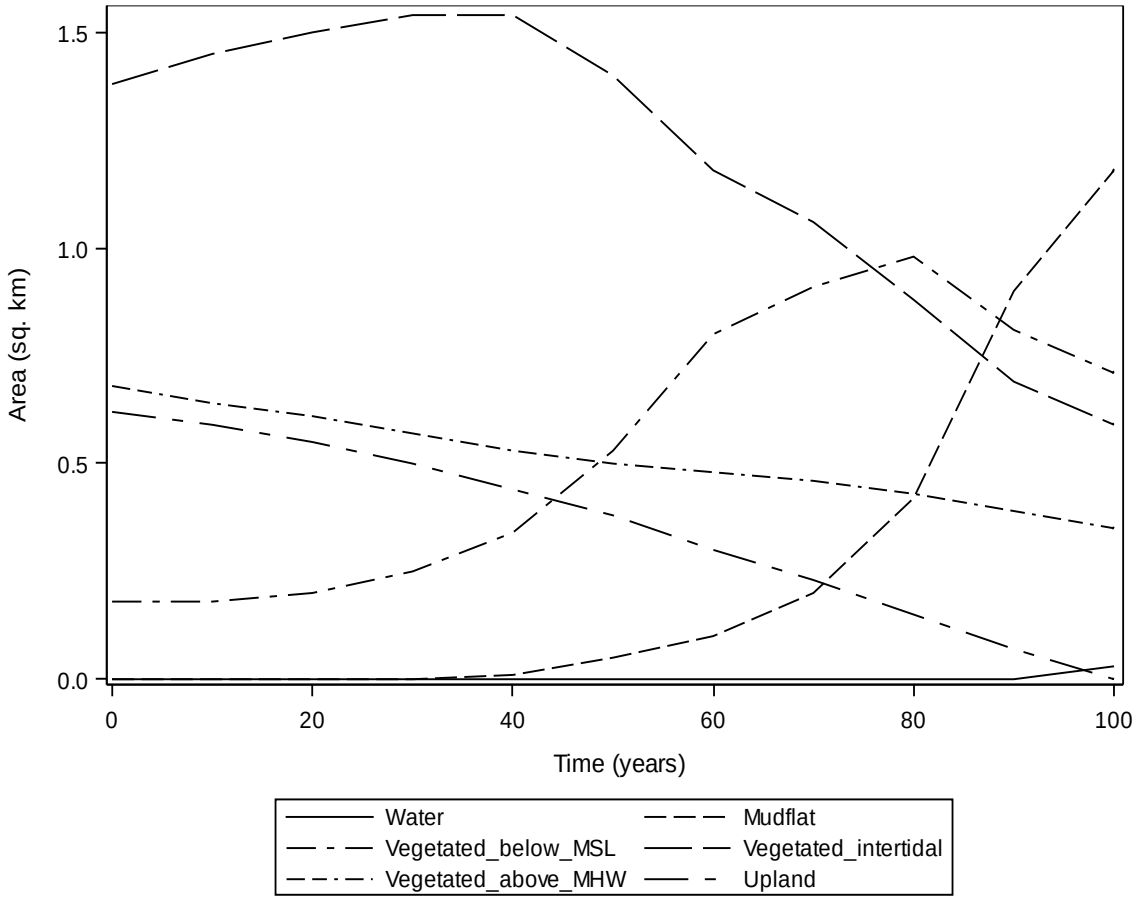

Figure 3.16. 5 m resolution MEM3D predicted area (km^2) of NI-Winyah Bay classified land cover vs. time (years).

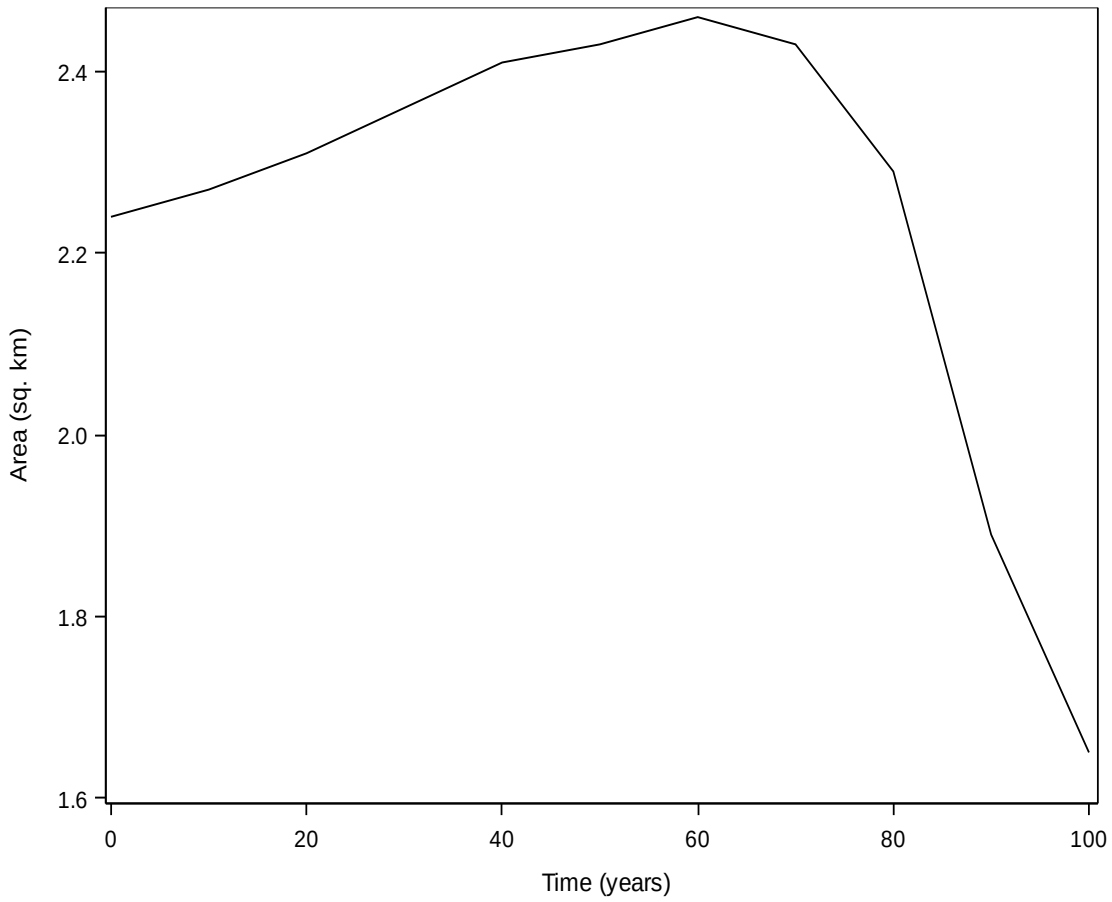

Figure 3.17. 5 m resolution MEM3D predicted NI-Winyah Bay total marsh area (km^2) by time (years). Total marsh area represents the cumulative sum of all S. alterniflora vegetated pixels.

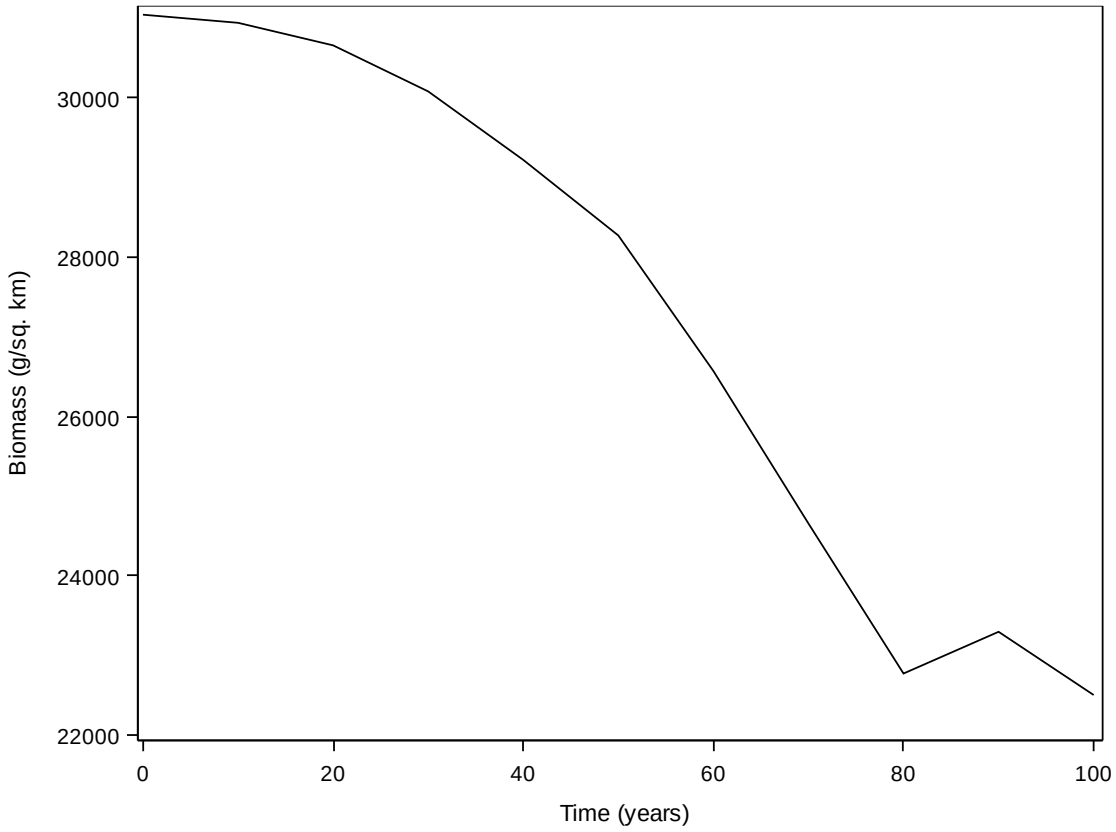

Figure 3.18. 5 m resolution MEM3D predicted total NI-Winyah Bay *S. alterniflora* above-ground biomass (g/m^2) vs time (years).

Figure 3.19. Location of outliers resulting from the aggregation of 2007 1 m LiDAR to 5 m resolution.

Chapter 4: Prediction of Saltmarsh Vegetative Above-Ground Biomass from a High Resolution Terrestrial Laser Scanner

Saltmarsh vegetation above-ground biomass is vital to the ecosystem's survival against accelerating sea-level rise. Leonard and Croft (2006), Leonard and Luther (1995), Nepf & Vivoni (2000), and Peterson et al. (2004) provide empirical results displaying non-linear sedimentation rates as result of changes in structural density of vegetative canopies in a water column. The authors' results are contingent on traditional biomass measurements. The traditional method of vegetative biomass determination is to harvest live vegetation from pre-determined sample plots and to process the samples within a laboratory. This method is laborious, physically demanding, time consuming, and environmentally destructive (Baskerville 1972; Eitel, Vierling, & Magney 2013; Garcia et al. 2010; Lin et al. 2010; Loudermilk et al. 2009). These limitations have resulted in long term datasets of vegetative biomass to be infrequent and spatially limited to a single site or small set of sites. Numerical models, such as the Marsh Equilibrium Model (Morris et al. 2002), utilize above-ground biomass to forecast vertical accretion. The measurement of saltmarsh above-ground biomass, therefore, is an important component of vegetative structural morphology that is critical to appropriately model the future distribution of saltmarshes. There exists a need to develop rapid on-site saltmarsh vegetation biomass determination techniques that are environmentally friendly. Recent advances in LiDAR technology provide a promising approach to address this issue.

LiDAR became mainstream in the last quarter of the 20th century. Historically used within satellites for atmospheric research, the technology has become commonly used mounted on airplanes (i.e. Airborne Laser Scanning: ALS) for high accuracy measuring of topography and bathymetry (Wandinger 2005). Stemming from the need to develop efficient and accurate ways to quantify horizontal and vertical distributions of vegetation in forests, the technology has been introduced to, but limited in, biological applications (Loudermilk et al. 2009; Michel et al. 2008; Rossell et al. 2009). Drake et al. (2002; 2003), Lefsky et al. (1999), Means et al. (1999), and Nelson, Krabill, & Tonelli (1988) report positive correlations between LiDAR derived point cloud metrics and landscape-scale forest canopy biomass collected from traditional techniques. At the local-scale, however, the relationship fails due to low posting densities (Eitel, Vierling, & Magney 2013; Hopkinson et al. 2004; Lin et al. 2010). The advancement of LiDAR technology in the direction of terrestrial systems is fostering new research at the micro-scale.

Terrestrial laser scanning was developed to provide industrial and civil engineers a lightweight tool to generate dense point clouds at micro-scales (Dassot, Constant, & Fournier 2011). Current TLS systems allow users to collect thousands to millions of points per second at scales up to 100 m (Michel et al. 2008). In the last decade, TLS has advanced to become a common method for the optical measurement of the 3D extensions of distinct objects (Seidel et al. 2011). Accurate measurements of single tree and canopy metrics have been successfully estimated using tripod mounted TLS systems under forest canopies (Henning & Radthe 2006; Hopkinson et al. 2004; Tanaka, Yamaguchi, & Takeda 1998; Watt & Donoghue 2005). Expansion of TLS technology into studies

involving fine-scale graminoid characteristics is limited (Rowell & Sceielstad 2012). The absence of appropriate methods to use this data in a meaningful way coupled with the lack of sensitivity when estimating biomass strain further advancement (Garcia et al. 2010; Michel et al. 2008). Loudermilk et al. (2009) provides evidence that micro-scale forest understory fuel volume can successfully be predicted using an elevated TLS. Studying dominant sagebrush species found within ecosystems of the western US, Olsoy, Glenn, and Clark (2014) utilized TLS to predict total and green biomass from a single study site. Exploring the use of TLS in a saltmarsh and deriving appropriate above-ground biomass predictive models is needed to provide an avenue of research into these sensitive ecosystems.

This study provides an initial attempt to test the hypothesis that TLS can be used to measure vegetative above-ground biomass for two saltmarsh species: *Spartina alterniflora* and *Juncus roemerianus*. The hypothesis firmly depends on whether the TLS system used can penetrate the marsh canopy. It is predicted that there exists an optimal resolution to collect dense point clouds representative of the entire canopy, and that from this representation, specific attributes can be used to predict above-ground biomass. This research is needed to provide a method to quickly and non-destructively estimate saltmarsh vegetative above-ground biomass at locations where no such information exists.

Methods

Leica ScanStation P20®

The TLS used to collect point clouds of saltmarsh vegetation biomass is the Leica ScanStation P20® (Leica Geosystems 2016a). Figure 4.1 represents the standard TLS scanning principal providing a right triangle to the laser beam at 10 m. Manufacturer specifications, Table 4.1, place the laser beam wavelength at 658 nm with a beam diameter at the front window of 2.8mm. To maximize the number of recorded observations, a trigometric function on the beam divergence at the scanner was solved. Since no knowledge of the hypotenuse was available, the beam divergence, in degrees, was the inverse tangent of the quotient between the resolution leg (*O*) and the distance leg (*A*). The beam divergence and the resolution leg (*O*) were held constant at the calculated degree and 2.8mm, respectively, to calculate critical distances (Table 4.2). A custom device (Figure 4.2) designed from stainless steel tubing and cables termed a 'boom' or 'howitzer' was designed by the University of South Carolina College of Arts and Sciences Mechanical Prototype Facility (USC 2008) to allow the terrestrial laser scanner to be hoisted above the marsh surface. The derivation of critical distances and custom equipment design allow for the collection of high-density LiDAR point clouds in a saltmarsh.

Data Collection and Processing

Data collection consisted of collecting point clouds and vegetative biomass within 0.25m^2 white Polyvinyl Chloride (PVC) quadrats randomly assigned to *Spartina alterniflora* and *Juncus roemerianus* across the marsh platform. Random assignment consisted of throwing a single quadrat onto the marsh. Vegetation was carefully

maneuvered to either be within or outside the quadrat based on location of stalk protruding from the soil surface, thereby allowing it to rest on bare soil. Two additional quadrats were placed approximately 0.25m right and left of the initial quadrat forming a triplet to increase sample collection. The P20 terrestrial laser scanner was mounted on the 'howitzer' in an inverted position and hoisted to be near the edge of the center quadrat. A single point cloud was collected at a resolution of 6.3mm @ 10m. The scanning angle, or area of collection from the scanner, was adjusted to 65° - 90° to decrease collection time and avoid sampling un-needed data outside of the quadrat triplet. Point cloud data were uploaded to Leica Cyclone®, Leica's proprietary software required to use data collected with their products (Leica Geosystems 2016b). The PVC quadrats were located within the scan image and delineated based on sample ID. Delineated point clouds are horizontally cropped of all data remaining outside the quadrat to exclude neighboring point returns. All returns below the top of the PVC quadrat were removed assuming the location approximates the soil surface. The remaining point cloud is representative of sample vegetation within the PVC quadrat and is exported with Cartesian coordinates, elevation relative to scanner, and intensity to a 3D point file for further analyses within a statistical software package.

All vegetation within the quadrat was clipped at ground level, and processed in the laboratory within 36 hours of collection to prevent errors associated with decay and regrowth. Stems of each plant were aligned and leveled where they were cut. Stems were cut into 10 cm subsamples and bagged for drying. All samples were placed in a drying oven at 64° C for 5 days to remove water weight. Dried samples were removed from the oven and weighed within 1 hr. to prevent absorption of water vapor. Biomass, recorded

as the difference between total weight and empty bag, was recorded for further manipulation.

Biomass Model Derivation

Sample point clouds were imported as individual datasets into SAS 9.4 for statistical analyses. Analyses were conducted independently for populations belonging to each species. Because raw data were collected below the scanner resulting in negative elevations, a means procedure was employed to derive the minimum elevation within each dataset and force all elevations positive referenced to 0m. All elevations above the 99^{th} percentile of elevations within each station were deleted from further analyses to reduce the effect of possible foreign debris collected in the point cloud. All samples were labeled and merged into a single species population dataset to conduct the remaining analyses. Successive bins were created to subsample the data by label and elevation to increase the number of samples used in statistical analyses. The bottom 10cm of data were deleted for each successive bin until the top of the canopy was encountered. Elevation was updated by subtracting 10cm from each succession to force the minimum elevation of the subsample to 0m. A final population dataset was created by merging the original dataset and each of the subsampled bins to store the data by species. A univariate procedure was employed to provide elevation descriptive statistics on the population dataset. All available SAS metrics were enumerated (Table 4.3) and exported to a dataset. Species' above-ground biomass was successively binned to match the subsampled point clouds. Biomass for each bin was recorded as the cumulative biomass minus the biomass of the bottom 10cm. Binned above-ground biomass was merged with the statistical dataset to produce a final population dataset suitable for regression analyses.

An initial linear regression was attempted to test the multicollinearity and usefulness of the raw statistical measures in a predictive model. Principal components analysis (PCA) was employed to reduce the correlation between explanatory statistical variables and improve the predictive biomass model. Principal components were calculated from the set of explanatory elevation statistical measures. The minimum eigenvalue for component inclusion was set to 1 to identify the factors explaining more than 1% of the total variance within the explanatory biomass variable. An orthogonal matrix representing variance within the explanatory variables was set to be rotated such that the variance was maximized and correlation minimized between the factors resulting in variable assignment. Explanatory variables loading onto no factors or multiple factors were removed from further analyses assuming their contribution to the variance was 0 or were still correlated with other variables respectively. Standardized scoring coefficients were exported and used to enumerate the factor. Factors were regressed against biomass to produce preliminary diagnostics. Model diagnostics were inspected for significance to decide which factors were significant in a predictive model. Point clouds were filtered based on intensity to test the effects of edge returns. The 1^{st} and 5^{th} percentiles were identified for each species population and sequentially removed. The removal of each intensity was followed by the described procedure to determine the best fit linear predictive model.

The single best predictive model for each species was tested against independent field data. Binned point cloud data were processed to provide statistical metrics and joined with binned biomass data for regression. Predicted biomass was calculated through the best fit predictive model and directly compared to that measured from the field. Mean

absolute difference (MAE) and root mean squared error (RMSE) were enumerated to identify the overall accuracy of the model in determining biomass from remotely sensed LiDAR data.

Results

Results for the P20 beam divergence calculations are presented in Table 4.2. Beam divergence at scanner was found to be a maximum of 0.29° for the pre-set resolution of 50mm at 10m and a minimum of 0.005° for the 0.8mm at 10m resolution. Critical distance was found to vary from 0.55m for the 50mm at 10m resolution to 32.09m for the 0.8mm at 10m resolution.

Collinearity among explanatory variables is presented in Tables 4.4 – 4.5. Table 4.4 results originate from *S. alterniflora* while Table 4.5 results are from *J. roemerianus*. Data for the initial linear regression are presented in Table 4.6. All parameter estimates in the model were biased and insignificant at α=0.05. Variance inflation for the *S. alterniflora* variables was found to be a minimum of 4.67 for standard error of the mean. Variance inflation for *J. roemerianus* variables was found to be a minimum of 7.99 for the mode.

Principal component analysis factor properties are presented in Table 4.7. For the *S. alterniflora* data, the first 4 factors explaining 95% of the variance in the raw variables were retained and exhibit eigenvalues of 21.10, 3.00, 1.71, and 0.83 respectively. The first 3 factors explaining 94% of the total variance were retained for *J. roemerianus* with eigenvalues of 22.06, 2.96, and 1.36 respectively. All retained factors for both species explain at least 2% of the variance independently. The scree plot, Figure 4.3, displays

graphically the relationship between explanatory factors and their respective eigenvalues for each species. Variables loading significantly onto *S. alterniflora* factors are presented in Table 4.8. The 5^{th} and 10^{th} percentiles were found to load significantly onto multiple factors. Mode and standard error of the mean were the only variables found to switch factors while removing the bottom 5% of intensity returns. Mode switched from factor 4 to 1 while the standard error of the mean switched from factor 3 to 4. All other variables remained on their respective factors regardless of intensity correction. Variables loading significantly onto *J. roemerianus* factors are presented in Table 4.9. The lower quartile and Uncorrected Sum of Squares were found to load onto no factors. Factor loadings were found to remain constant regardless of intensity correction.

Results of the regression of the retained factor scores against biomass are presented in Table 4.10. Regression analyses were employed on 3 intensity corrected simulations for each species: no intensity removal, clipping the bottom 1%, and clipping the bottom 5%. Factors 1 and 3 were found to be significant for all simulations while factor 4 was only significant while removing the bottom 5% of intensity returns. Removing the bottom 1% of intensity returns showed no significant improvement in biomass prediction while removing the bottom 5% of intensity returns increased the model R^2 by 0.05 from 0.84 to 0.89. Intensity removal for *J. roemerianus* showed no significant improvements to the model. Factors 1 and 2 are significant in predicting biomass.

Model diagnostics for the *S. alterniflora* best fit biomass predictive model with the bottom 5% of intensity returns removed are presented in Figure 4.4. Outlier analysis provided no evidence of significant outliers in the model. A residual histogram and plot

of residuals vs quantile provided additional evidence that the residuals are normally distributed. *J. roemerianus* model results are presented in Figure 4.5 for the simulation with no intensity removal. Standardized scoring coefficients for the factors under each species' best fit model are presented in Tables 4.11 and 4.12 respectively. Results for model verification are presented in Table 4.13. The *S. alterniflora* model was found to overestimate biomass of 25 samples, an average of 10.39g/0.25 m^2 with an associated RMSE of 20.33g/0.25 m^2. The *J. roemerianus* model was found to overestimate biomass of 28 samples, an average of 4.31g/0.25 m^2 with an associated RMSE of 31.08g/0.25 m^2. Graphs of biomass vs absolute error and biomass vs predicted biomass are presented for *S. alterniflora* in Figures 4.6 and 4.7 and *J. roemerianus* in Figures 4.8 and 4.9 respectively.

Discussion

This innovative study addressed the hypothesis that saltmarsh above-ground standing biomass can be predicted as a function of the spatial distribution of high-resolution LiDAR derived point clouds. Factory settings of a terrestrial laser scanner were analyzed to prove that there exists an optimal resolution and distance from object to maximize the point cloud. Point cloud returns were collected for the canopy of two saltmarsh species and indicated that the resolution used provides the density of points needed to penetrate an otherwise impassible canopy. Analyses of multicollinearity and principal components revealed that there are certain descriptive statistics of the point cloud that are important in predicting biomass. The quality of returns analyzed were found to have an effect on one of the two saltmarsh species modeled. Saltmarsh species

biomass has been proven capable of being rapidly measured non-destructively with the use of a terrestrial laser scanner.

The optimal TLS resolution for use in a saltmarsh exists as the trade-off between point cloud density and distance to object. Critical distances were calculated to identify the threshold minimum distance an object can be from the scanner that results in the densest point cloud. There is a minimum because in theory, a LiDAR system will collect invalid 'ghost' returns at a spacing smaller than the diameter of its laser beam (Baldwin & Newman 2012). With the minimum height needed over 8m, the 3.1, 1.6 and 0.8 mm @ 10m resolutions are infeasible for saltmarsh studies. These resolutions would require tall and stable structures permanently mounted on the marsh platform to provide safe operation. Considering the beam divergence of the remaining resolutions and that plant height could approach 2m at an extreme, the lowest two resolutions are impractical. This is because the increased beam divergence causes a rapid point density decay with increasing distance. Of the remaining resolutions, 6.3mm @ 10m is the optimal resolution for saltmarsh studies. Using this resolution, the terrestrial laser scanner would need to be hoisted approximately 6m above the marsh canopy, clearing the assumed 2m maximum vegetative height. While the 12.5 mm @ 10 m resolution is viable, it is characterized as having a slightly larger beam divergence and expected to not produce the most dense point cloud at an approximate height of 6 m above the canopy.

Canopy penetration is a major issue for studies whose objective depends on measures of elevation. Hopkinson et al. (2004) reports from a review of multiple studies using LiDAR that single tree above-ground biomass is typically well under predicted. Using LiDAR in saltmarshes Chassereau, Bell, & Torres (2011), Hladik & Albers (2012),

Montane & Torres (2006), and Morris et al. (2005) have found positive error bias of LiDAR in southeastern USA saltmarshes up to 0.17 m. The literature indicates that LiDAR is poor at penetrating dense canopies due to its inherent low point cloud density. As the density of the canopy of interest increases, the probability of a laser beam penetration is directly proportional to the number of intercepts, or the point density. Terrestrial laser scanning, being a new technology, is not represented in the saltmarsh literature. The reported issues on the use of LiDAR in saltmarshes stem from the poor posting density of airborne systems. The fact that point cloud returns were recorded for every 10cm segment of the sample demonstrates the TLS is penetrating the canopy.

Multicollinearity between variables impedes the identification of significance in regression models. The initial attempt to predict biomass through linear regression against statistical properties of the point cloud produced no significant results (Table 4.6). The results of insignificance from the initial regression attempt was not surprising because some of the metrics SAS reports are mathematically similar. The mathematical similarity allowed for the identification and removal of variables that were linear combinations of other variables. Interquartile range standard deviation, Gini's standard deviation, median absolute difference about the median standard deviation, stdsn (a normalized alternative to median absolute difference about the median standard deviation), range, and the upper quartile of the elevation returns from *S. alterniflora* were found to be linear combinations of other explanatory variables (Table 4.4). Only interquartile range standard deviation, Gini's standard deviation, and median absolute difference about the median standard deviation were found to be linear combinations of the remaining explanatory variables for *J. roemerianus* (Table 4.5). O'Brien (2007)

discusses that multicollinearity between independent variables increases the estimates of the parameter variance and that variance inflation factors (VIF) of more than 10 suggest extreme multicollinearity. Variance inflation is interpreted as the quotient of the observed variance and what would be expected if all other variables were removed. Variance inflation reported in Table 4.6 for all remaining variables after those with linear representations are removed indicate moderate to extreme multicollinearity. Of the 25 explanatory variables for *S. alterniflora,* only the standard error of the mean (4.67) did not exceed the VIF threshold. A similar result was observed for *J. roemerianus* in that of the 28 variables, only the mode (7.99) did not exceed the threshold. Variance inflation indicates that the remaining explanatory variables for both species exhibit extreme multicollinearity and that the use of principal components is justified to combine correlated variables into a single variable.

Principal component analysis for the *S. alterniflora* and *J. roemerianus* point clouds reduced the explanatory variables into 4 and 3 factors respectively (Tables 4.7-4.9). The eigenvalue for the fourth factor (0.83) of *S. alterniflora* was considered close enough to the accepted minimum of 1 for inclusion. It appears that 95% cumulative variance explained (Table 4.7) by the factors represents a critical threshold for inclusion. The fact that cumulative variance for the 4^{th} variable for *J. roemerianus* was 97% and not significant for the model coupled with the 95% for the 4th *S. alterniflora* factor indicates that 95% represents a threshold. It is interpreted that this is because the majority of variables load significantly onto the first factor (Tables 4.8-4.9), with near equal loadings of the remaining variables on the next 2-3 factors. As the variable number is reduced with increasing factor number, the higher order factors would only contain a single variable as

evidenced by *S. alterniflora* factor 4 (Table 4.9), an exception that was only included by discretion.

Model diagnostics for 3 scenarios indicate that factors 1, 3, and 4 are significant for predicting *S. alterniflora* biomass while factors 1 and 2 are significant for predicting *J. roemerianus* biomass (Table 4.10). The quality of the point cloud returns were found to increase the predictive power of the *S. alterniflora* biomass but not *J. roemerianus* (Table 4.10). The best fit *J. roemerianus* model was, therefore, determined without correcting for intensity. The model exhibited an adjusted R^2 of 0.89 and significant F-value of 132.26. Removing the bottom 5% of *S. alterniflora* intensity returns increased the adjusted R^2 value by 0.05 to 0.89 with a significant F-value of 122.07. The reported significance in F-values suggests that there is strong evidence in both models that the enumerated factors contribute to estimating biomass and that the reported R^2 values are reliable. The increase in predictive power with removing intensity values for *S. alterniflora* is interpreted to be a function of plant morphology and resolution. Eiting, Vierling, & Long (2010) report that low intensity returns are the result of the laser beam being partially intercepted by the edge of an object. The result of such interceptions are two observations with erroneous elevations caused by the inability of the system to calculate time-of-flight distance. Obtaining the highest density point cloud possible (point spacing ~2mm) would increase the probability of edge effects for *S. alterniflora* and not *J. roemerianus* because of the shape of each species leaf. *S. alterniflora* leaves can be characterized as long and flat that generally slump over while *J. roemerianus* leaves can be characterized as cylindrical and stiff remaining erect for their entire length. It would therefore be expected that since *S. alterniflora* leaves provide more surface area and are

more widely distributed in the sample space, that there should be an increase in the probability of edge returns as compared to *J. roemerianus*.

When inspecting variable loadings for the factors, a specific pattern could be interpreted: the shape of the distribution has no impact on biomass estimation. Factor 2 for *S. alterniflora* and 3 for *J. roemerianus* are composed of the 3 dominant variables (skew, kurtosis, and coefficient of variation) describing the shape of the elevation frequency distribution. The insignificance of the shape of the distribution could be a product of elevation and biomass skew. If a standard elevation frequency across all samples exists such that the distributions are nearly identical, then the identical shape of the distribution would have negligible results in predicting biomass. This would also suggest further consideration as to how the canopy is being penetrated by the terrestrial laser scanner.

Data presented in Table 4.13 suggest that *S. alterniflora* and *J. roemerianus* biomass can be predicted with high levels of certainty. Model error has been a topic of debate in the literature with no clear consensus on an appropriate metric for model validation (Chai & Draxler 2014). The RMSE has been presented as a suitable metric for model error by the geosciences community because it describes the spread of error (Chai et al. 2013; McKeen et al. 2005; Savage et al. 2013). Conversely, Willmott & Matsuura (2005) and Willmott et al. (2009) avoid the use of RMSE in favor of MAE as it assumes equal weight for all variances, thereby, insensitive to outliers. The authors report that in the presence of large outliers, RMSE can become misleading due to inflation. To address the lack of consensus, Chai & Draxler (2014) propose the use of both metrics in that the

magnitude of difference between them can address the distribution of variance better than a single use alone.

The reported MAE (10.39) and RMSE (20.33) for *S. alterniflora* are similar and indicate that the variance in the model is fairly uniform. A graph of biomass vs absolute error for *S. alterniflora* (Figure 4.6) provides visual evidence for the uniform distribution of error. No correlation is observed between the magnitude or error and increasing biomass. This is an important finding as it suggests that the model distributes *S. alterniflora* biomass prediction error equally for data collected anywhere on the marsh platform as depicted by plotting field collected biomass vs model predicted biomass (Figure 4.7). Biomass for *S. alterniflora* is known to increase to a maximum at an equilibrium elevation for the species niche (Morris et al. 2002). It is a major finding that the model can be expected to appropriately predict *S. alterniflora* biomass within an average of 20.33g/0.25 m^2.

The reported MAE (4.31) and RMSE (31.08) for *J. roemerianus* exhibits a greater difference than that reported for *S. alterniflora*, indicating disproportional distribution of error. Graphing biomass vs absolute error (Figure 4.8) reveals this relationship. There appears to be a strong correlation between the magnitude of error and increasing biomass. It is demonstrated that as biomass increases, the model begins to fail at appropriately predicting *J. roemerianus* biomass. The trend is interpreted to be a function of plant morphology and distribution of biomass. *J. roemerianus* has been characterized has having cylindrical erect live leaves. Field and lab observation from the date of collection of verification samples place a thick layer of wrack and senescing *J. roemerianus* near the ground level. The laser beam most likely under-collected data below the elevation of

these obstructions. The result of this scenario is manifested in the distribution of error. Because the data were binned by sequentially removing the bottom 10cm of data, low biomass is representative of the live portion of the canopy above the described obstructions. Coincidentally, the model appropriately predicts this region with minimal error. High biomass is representative of the entire canopy, a portion of which would not have been collected below the elevation of the obstructions. When attempting to predict the biomass for the entire sample, it is demonstrated that the model begins to fail and is characterized by having increased error. Plotting biomass vs. predicted biomass (Figure 4.9) further corroborates the disproportionate trend in error.

The approach used for this study is satisfactory for developing saltmarsh biomass predictive models with a particular caveat to *J. roemerianus*. Model results for *J. roemerianus* indicate that the model is most useful for predicting live vegetation, not the entire canopy. The study proves that TLS can be used to estimate *S. alterniflora* biomass from multiple locations within the marsh platform, thereby providing much needed data for numerical modelling that is currently hindered by the spatial limitation of long-term datasets. Results from the study prove that TLS is a powerful LiDAR technology capable of penetrating the *S. alterniflora* canopy, a feat beyond the capability of airborne systems. It is demonstrated, however, that TLS still has difficulty in penetrating *J. roemerianus* canopies and this may be due to tidal conditions near the timing of final data collection. The findings of this study provide an opportunity to identify biomass specific correction factors for landscape-scale LiDAR. Future efforts should align with the collection of airborne LiDAR such that actual elevation and biomass can be collected via TLS in the saltmarsh simultaneously with an airborne LiDAR mission. Findings from such a study

can greatly enhance current modeling efforts by improving known issues with landscape-scale LiDAR. A major benefit of the findings is they address how to quickly collect data without destructive harvesting. Future studies should focus on the morphology by bin and the addition or creation of other metrics. Biomass plays a critical role in sedimentation that the identification of morphological characteristics by elevation intervals can be a substantial contribution to sedimentation models and thus developing landscape-scale predictive models of saltmarsh survivability and distribution during sea-level rise scenarios.

Conclusion

Data collected from a TLS provide satisfactory biomass predictive models for *S. alterniflora* and *J. roemerianus*. It was found that the optimal resolution for data collection in saltmarshes is 6.3 mm @ 10 m and that this resolution provides a density sufficient to penetrate all layers of the canopy. Analysis of collinearity indicated that six of the reported variables for *S. alterniflora* and three for *J. roemerianus* were linear representations of the other explanatory variables and thus unsuitable for predicting biomass. Multicollinearity results indicated that the variance of the remaining variables was highly inflated warranting a principle components procedure to identify significant components or factors. Principle components analysis indicate that there exists four significant factors for *S. alterniflora* and 3 for *J. roemerianus*. The quality of point cloud returns was found to effect the predictive power of *S. alterniflora*, not *J. roemerianus*. Linear regression of biomass against the scored factors indicate that the shape of the frequency distribution does not significantly contribute to biomass estimation for either

species. Final biomass predictors were found to exhibit high R^2 values: 0.89 for both species. Verification of the models against independent data suggests *S. alterniflora* is underestimated an average of 10.39 g/0.25 m^2 and *J. roemerianus* is overestimated an average of 4.31 g/0.25 m^2.

Table 4.1. Leica P20 TLS system specifications as described by Leica (2016a).

Type	Ultra-high speed time-of-flight enhanced by Waveform Digitizing (WFD) technology
Laser wavelength	658 nm
Laser beam diameter at front window	2.8 mm
Range	Max: 120 m Min: 0.4 m
Scan rate	Max. 1,000,000 points/s
Scanning resolution	7 pre-set point spacing (mm at 10 m) Spacing 50 25 12.5 3.1 1.6 0.8
Field of view	Horizontal: 360° Vertical: 270°

Table 4.2. Leica P20 scanning resolution
beam divergence and critical distance.

Point Spacing (mm @ 10 m)	θ°	Critical Distance (m)
50	0.29	0.55
25	0.14	1.15
12.5	0.07	2.29
6.3	0.04	4.01
3.1	0.02	8.02
1.6	0.01	16.04
0.8	0.005	32.09

Table 4.3. Description of input model explanatory variables availabble as output from SAS and grouped by mathmatical calculation method.

Variable	Descriptive Statistics
CSS	Corrected sum of squares
CV	Coefficient of variation
kurt	Kurtosis of the elevation frequency distribution
max	Maximum elevation return
mean	Average of all elevations
mode	Most frequent elevation
obs	Number of elevation returns
range	Range of elevation returns
skew	Skew of the elevation frequency distribution
std	Standard deviation of the elevation frequency distribution
stdmean	Standard error of the mean
USS	Uncorrected sum of squares
var	Variance of the elevation frequency distribution
	Robust Statistics
gini	Gini's mean difference
mad	Median absolute difference about the median
sn	Alternative to MAD
stdgini	Gini's standard deviation
stdmad	MAD standard deviation
stdmean	Standard error of the mean
stdqrange	Interquartile range standard deviation
stdsn	Sn standard deviation
	Quantile Statistics
med	Median of the elevation frequency distribution
p1	1st percentile of the elevation frequency distribution
p10	10th percentile of the elevation frequency distribution
p5	5th percentile of the elevation frequency distribution
p90	90th percentile of the elevation frequency distribution
p95	95th percentile of the elevation frequency distribution
p99	99th percentile of the elevation frequency distribution
q1	Lower quartile of the elevation frequency distribution
q3	Upper quartile of the elevation frequency distribution
qrange	Interquartile range of the elevation frequency distribution

Table 4.4. *S. alterniflora* highly correlated explanatory variables reported as linear combinations.

Variable	Linear combination of other variables
Interquartile range standard deviation =	-423E-12 * mean + 18E-17 * uncorrected sum of squares - 731E-14 * 99th percentile + 0.7413 * inter-quartile range + 447E-12 * Gini's mean difference + 128E-12 * median absolute difference about the median - 621E-13 * alternative to MAD + 365E-18 * corrected sum of squares + 137E-12 * standard deviation - 137E-12 * 10th percentile - 161E-12 * lower quartile - 865E-13 * median + 438E-14 * 90th percentile - 495E-14 * 95th percentile
Gini's standard deviation =	-352E-12 * mean + 134E-18 * uncorrected sum of squares + 18E-12 * inter-quartile range + 0.88623 * Gini's mean difference + 974E-13 * median absolute difference about the median - 448E-13 * alternative to MAD + 335E-18 * corrected sum of squares + 148E-12 * standard deviation - 135E-12 * 10th percentile - 119E-12 * lower quartile - 808E-13 * median - 938E-14 * 90th percentile - 131E-13 * 95th percentile
MAD standard deviation =	1.01E-9 * mean + 224E-18 * uncorrected sum of squares - 498E-14 * maximum - 147E-12 * 5th percentile - 895E-13 * inter-quartile range - 415E-12 * Gini's mean difference + 1.4826 * Median absolute difference about the median + 316E-13 * alternative to MAD + 133E-17 * corrected sum of squares - 344E-13 * standard deviation - 182E-12 * variance+ 113E-12 * 10th percentile + 402E-12 * lower quartile + 261E-12 * median + 63E-12 * 90th percentile - 373E-14 * 95th percentile
SN standard deviation =	2.56E-6 * Intercept - 0.00223 * mean + 6.84E-6 * skewness + 1.64E-9 * uncorrected sum of squares - 2.45E-6 * kurtosis + 0.00001 * maximum - 0.00005 * 99th percentile - 0.00031 * 5th percentile - 0.00017 * inter-quartile range + 0.00002 * mode + 0.0027 * Gini's mean difference + 0.00076 * Median absolute difference about the median + 0.99954 * alternative to MAD + 4E-9 * corrected sum of squares + 1.21E-7 * coefficient of variation - 127E-14 * observations + 0.00009 * standard deviation - 0.01434 * standard error of the mean + 0.00033 * variance - 0.00023 * 1st percentile - 0.00116 * 10th percentile - 0.00061 * lower quartile - 0.00058 * median + 0.00017 * 90th percentile + 0.00009 * 95th percentile

Table 4.4 continued

range =	-5.09E-6 * Intercept - 0.00145 * mean - 0.00003 * skewness + 16E-11 * uncorrected sum of squares + 9.81E-6 * kurtosis + 1.00001 * maximum - 0.00059 * 99th percentile + 0.00868 * 5th percentile - 0.00359 * inter-quartile range - 0.00009 * mode + 0.04157 * Gini's mean difference - 0.00598 * median absolute difference about the median - 0.00186 * alternative to MAD - 396E-14 * corrected sum of squares + 2.32E-7 * coefficient of variation + 418E-14 * observations + 0.02414 * standard deviation + 0.00679 * standard error of the mean + 0.00368 * variance + 0.00063 * 1st percentile + 0.00404 * 10th percentile + 0.00051 * lower quartile - 0.00145 * median + 0.00295 * 90th percentile - 0.00018 * 95th percentile
Upper quartile =	-1.95E-9 * mean - 246E-18 * uncorrected sum of squares + 673E-14 * maximum + 116E-13 * 99th percentile + 221E-12 * 5th percentile + 1 * inter-quartile range + 816E-12 * Gini's mean difference + 349E-12 * Median absolute difference about the median - 96E-12 * alternative to MAD + 197E-17 * corrected sum of squares - 767E-13 * standard deviation - 342E-12 * variance + 258E-12 * 10th percentile + 1 * lower quartile + 486E-12 * median - 119E-12 * 90th percentile + 723E-14 * 95th percentile

Table 4.5. *J. roemerianus* highly correlated explanatory variables reported as linear combinations.

Variable	Linear combination of other variables
Interquartile range standard deviation =	4E-12 * Intercept - 27E-11 * variance + 369E-13 * mean + 337E-14 * skewness - 732E-15 * kurtosis - 382E-12 * maximum - 55E-13 * 99th percentile + 0.7413 * inter-quartile range - 1.17E-9 * Gini's mean difference + 127E-12 * median absolute difference about the median + 2.16E-9 * alternative to MAD + 2.21E-9 * Sn standard deviation - 641E-17 * corrected sum of squares + 102E-15 * coefficient of variation + 697E-19 * observations - 386E-12 * range - 831E-12 * std - 314E-12 * standard error of the mean - 211E-12 * 1st percentile + 624E-13 * median - 132E-12 * upper quartile - 62E-12 * 90th percentile - 195E-13 * 95th percentile + 258E-12 * 5th percentile + 766E-13 * 10th percentile
Gini's standard deviation =	-287E-13 * Intercept - 3.43E-9 * variance + 118E-12 * mean - 109E-13 * skewness + 318E-14 * kurtosis + 1.04E-8 * maximum + 113E-12 * 99th percentile - 123E-13 * inter-quartile range + 0.88623 * Gini's mean difference + 449E-12 * median absolute difference about the median + 2.1E-8 * alternative to MAD + 2.13E-8 * Sn standard deviation - 239E-16 * corrected sum of squares - 244E-15 * coefficient of variation + 224E-18 * observations + 1.04E-8 * range + 3.32E-9 * standard deviation + 563E-12 * standard error of the mean - 197E-12 * 1st percentile + 233E-12 * median + 192E-12 * upper quartile - 115E-13 * 90th percentile - 171E-12 * 95th percentile + 326E-12 * 5th percentile - 281E-12 * 10th percentile
MAD standard deviation =	248E-13 * Intercept + 1.86E-9 * variance - 161E-12 * mean + 121E-13 * skewness - 319E-14 * kurtosis - 7.47E-9 * maximum - 827E-13 * 99th percentile - 17E-12 * inter-quartile range - 3.56E-9 * Gini's mean difference + 1.4826 * median absolute difference about the median - 1.06E-8 * alternative to MAD - 1.08E-8 * Sn standard deviation + 605E-17 * corrected sum of squares + 309E-15 * coefficient of variation - 435E-19 * observations - 7.47E-9 * range - 3.43E-9 * standard deviation - 837E-12 * standard error of the mean - 233E-12 * 1st percentile - 963E-13 * median - 378E-12 * upper quartile - 847E-13 * 90th percentile + 87E-12 * 95th percentile + 211E-12 * 5th percentile + 242E-12 * 10th percentile

Table 4.6. Biomass regression results with remaining explanatory variables after removing linear variables. Reported Degrees of Freedom (DF) of 'B' implies that the estimate is biased and not unique. Probability values report significance while Variance Inflation (VI) measures the increase in variance. *J. roemerianus* results are displayed in grey.

Variable	DF	Pr > |t|		Variance Inflation	
Intercept	B	0.61	0.92	0.00	0
Mean	B	0.38	0.37	794295.00	1922.92
Skewness	B	0.60	0.12	144.36	90348.00
Uncorrected sum of squares	B	0.21	.	9251.99	.
Kurtosis	B	0.39	0.70	80.67	849.00
Maximum	B	0.57	0.71	2068.86	692.61
99th percentile	B	0.53	0.81	11923.00	20051985.00
5th percentile	B	0.62	0.80	2268.32	1078.56
Inter-quartile range	B	0.21	0.47	13795.00	12337.00
mode	B	0.27	0.50	92.16	7.99
Gini's mean difference	B	0.89	0.85	259489.00	266822.00
Median absolute difference about the median	B	0.78	0.34	18000.00	4374.51
Alternative to MAD	B	0.46	0.66	8151.59	2406367.00
Sn standard deviation	B	.	0.65	.	2484727.00
Corrected sum of squares	B	0.32	0.47	10241.00	648.06
Coefficient of variation	B	0.73	0.56	57.23	446.34
Observations	B	0.13	0.35	33.34	620.28
Range	B	.	0.81	.	20088189.00
Standard deviation	B	0.95	0.73	105253.00	110232.00
Standard error of the mean	B	0.02	0.42	4.67	80.86
Variance	B	0.62	0.10	939.06	329.63
1st percentile	B	0.33	0.12	101.71	7590.17
10th percentile	B	0.57	0.24	5642.09	42194.00
Inter-quartile range	B	0.54	0.98	32807.00	4929.47
Median	B	0.27	0.80	56113.00	1872.55
Upper quartile	B	.	0.24	.	42194.00
90th percentile	B	0.26	0.25	37779.00	3202.81
95th percentile	B	0.76	0.19	12836.00	2888.24

Table 4.7. Eigenvalue properties of the factor matrix. Proportion reports the proportion of total variance explained by the factor while cumulative reports the cumulative proportion explained by the addition of factors. *J. roemerianus* results are displayed in grey.

Factor	Eigenvalue		Proportion		Cumulative	
1	21.10	22.06	0.75	0.79	0.75	0.79
2	3.00	2.96	0.11	0.11	0.86	0.89
3	1.71	1.36	0.06	0.05	0.92	0.94
4	0.83	0.66	0.03	0.02	0.95	0.97
5	0.55	0.37	0.02	0.01	0.97	0.98
6	0.37	0.20	0.01	0.01	0.98	0.99
7	0.16	0.19	0.01	0.01	0.99	0.99
8	0.13	0.06	0	0	0.99	1
9	0.09	0.04	0	0	1	1
10	0.02	0.03	0	0	1	1
11	0.01	0.02	0	0	1	1
12	0.01	0.02	0	0	1	1
13	0	0.01	0	0	1	1
14	0	0.01	0	0	1	1
15	0	0	0	0	1	1
16	0	0	0	0	1	1
17	0	0	0	0	1	1
18	0	0	0	0	1	1
19	0	0	0	0	1	1
20	0	0	0	0	1	1
21	0	0	0	0	1	1
22	0	0	0	0	1	1
23	0	0	0	0	1	1
24	0	0	0	0	1	1
25	0	0	0	0	1	1
26	.	0	.	0	.	1
27	.	0	.	0	.	1
28	.	0	.	0	.	1

Table 4.8 . *S. alterniflora* rotated factor pattern. Symbols denote the explanatory variables that significantly load onto the respective factors. Greyed out variables are removed from the model due to no factor loading.

Variable	Factor1	Factor2	Factor3	Factor4
Corrected sum of squares	* +^			
Coefficient of variation		*+^		
Gini's mean difference	*+^			
Median		*+^		
Median absolute difference about the mean	*+^			
Maximum	*+^			
Mean	*+^			
Median	*+^			
Mode	^			*+
Observations			*+	
1st percentile			*+^	
10th percentile				
5th percentile				
90th percentile	*+^			
95th percentile	*+^			
99th percentile	*+^			
Lower quartile	*+^			
Inter-quartile range	*+^			
Skewness		*+^		
Alternative to MAD	*+^			
Standard deviation	*+^			
Standard error of the mean			*+	^
Uncorrected sum of squares	*+^			
Variance	*+^			

* = No Intensity Removal
+ = Bottom 1% Intensity Removal
^ = Bottom 5% Intensity Removal

Table 4.9. *J. roemerianus* rotated factor pattern. Symbols denote the explanatory variables that significantly load onto the respective factors. Grayed out variables are removed from the model due to no factor loading.

Variable	Factor1	Factor2	Factor3
Corrected sum of squares	*+^		
Coefficient of variation			*+^
Gini's mean difference	*+^		
Kurtosis			*+^
Median absolute difference about the median	*+^		
Maximum	*+^		
Mean	*+^		
Median	*+^		
Mode		*+^	
Observations	*+^		
1st percentile		*+^	
10th percentile		*+^	
5th percentile		*+^	
90th percentile	*+^		
95th percentile	*+^		
99th percentile	*+^		
Lower quartile			
Upper quartile	*+^		
Inter-quartile range	*+^		
Range	*+^		
Skewness			*+^
Alternative to MAD	*+^		
Standard deviation	*+^		
Standard error of the mean	*+^		
Sn standard deviation	*+^		
Uncorrected sum of squares			
Variance	*+^		

* = No Intensity Removal

+ = Bottom 1% Intensity Removal

^ = Bottom 5% Intensity Removal

Table 4.10. Intensity corrected regression diagnostics by species (*J. roemerianus* in grey).

Model Run	Intercept Significant (Yes/No; α=0.05)	Significant Factors (α=0.05)	F^	Adj. R^2
No Intensity Removal	Y	Factor 1 Factor 3	119.96^	0.84
Bottom 1% Intensity Removal	Y	Factor 1 Factor 3	120.04^	0.84
Bottom 5% Intensity Removal	Y	Factor 1 Factor 3 Factor 4	122.07^	0.89
*No Intensity Removal	Y	Factor 1 Factor 2	132.26^	0.89
*Bottom 1% Intensity Removal	Y	Factor 1 Factor 2	132.26^	0.89
*Bottom 5% Intensity Removal	Y	Factor 1 Factor 2	132.26^	0.89
^ Denotes significant F-Value (α=0.05) *Model dependent variable is square root transformed Boxcox Lambda (λ) = 0.5				

Table 4.11. *S. alterniflora* standardized scoring coefficients for the 5% intensity reduction best fit linear model.

Standardized Scoring Coefficients				
Variable	Factor1	Factor2	Factor3	Factor4
mean	0.04184	-0.01968	0.03289	0.01231
skew	-0.01832	0.32889	0.12010	0.01653
USS	0.06414	-0.11397	-0.19980	-0.30547
kurt	-0.03743	0.29517	0.25207	0.00657
max	0.09238	0.11832	0.00254	-0.01698
p99	0.04751	0.05935	0.00165	0.01887
qrange	0.13965	0.01757	-0.03962	0.15833
mode	0.02534	-0.15835	0.00900	-0.17736
gini	0.11047	0.06848	-0.06095	0.09114
mad	0.10292	0.00224	-0.01404	0.13551
sn	0.10984	-0.00188	-0.06801	0.05411
CSS	0.06788	-0.07694	-0.20643	-0.28108
CV	0.08282	0.27149	-0.48847	-0.06810
obs	0.01082	0.02968	0.00823	-0.35864
std	0.05474	0.04712	-0.02939	0.05012
stdmean	-0.00213	-0.00612	0.26753	0.68576
var	0.07109	-0.01821	-0.15393	-0.08379
p1	-0.12838	0.06588	0.90637	0.26146
q1	0.04026	-0.07976	0.11203	-0.02869
med	0.04014	-0.06351	0.02706	-0.02250
p90	0.04929	0.02279	0.00180	0.04931
p95	0.05034	0.04119	-0.00759	0.03782

Table 4.12. *J. roemerianus* standardized scoring coefficients for the no intensity correction best fit linear model.

Standardized Scoring Coefficients			
	Factor1	Factor2	Factor3
mean	0.03630	0.02333	-0.01558
skew	0.02022	0.06827	0.35006
kurt	-0.00721	0.14341	0.37660
max	0.07777	-0.01677	0.09367
p99	0.08536	-0.03073	0.09480
qrange	0.14665	-0.13708	-0.14134
mode	-0.15380	0.38278	0.10570
gini	0.19083	-0.17789	-0.03581
mad	0.11072	-0.07037	-0.14323
sn	0.06196	-0.04632	-0.06933
stdsn	0.06165	-0.04591	-0.06971
CSS	-0.00723	0.11283	0.02382
CV	0.08703	-0.15527	0.15555
obs	0.02086	0.06767	0.03913
range	0.07796	-0.01708	0.09381
std	0.10248	-0.09071	0.01536
stdmean	-0.10149	0.06838	-0.13982
var	0.07581	-0.04000	0.01499
p1	-0.12918	0.34152	0.06852
med	0.00433	0.07403	-0.02921
q3	0.04155	0.00291	-0.04187
p90	0.07974	-0.06783	-0.03840
p95	0.08680	-0.06226	0.01239
p5	-0.10816	0.30766	0.06598
p10	-0.07763	0.25220	0.05464

Table 4.13. Predictive models and verification by species.

Species	Model	MAE	RMSE
S. alterniflora	Biomass = 46.22 + 28.73*F1 + 11.49*F3 -29.86*F4	10.39	20.33
J. roemerianus	$Biomass^{0.5}$ = 8.45 + 3.27*F1 + 1.52*F2	4.31	31.08

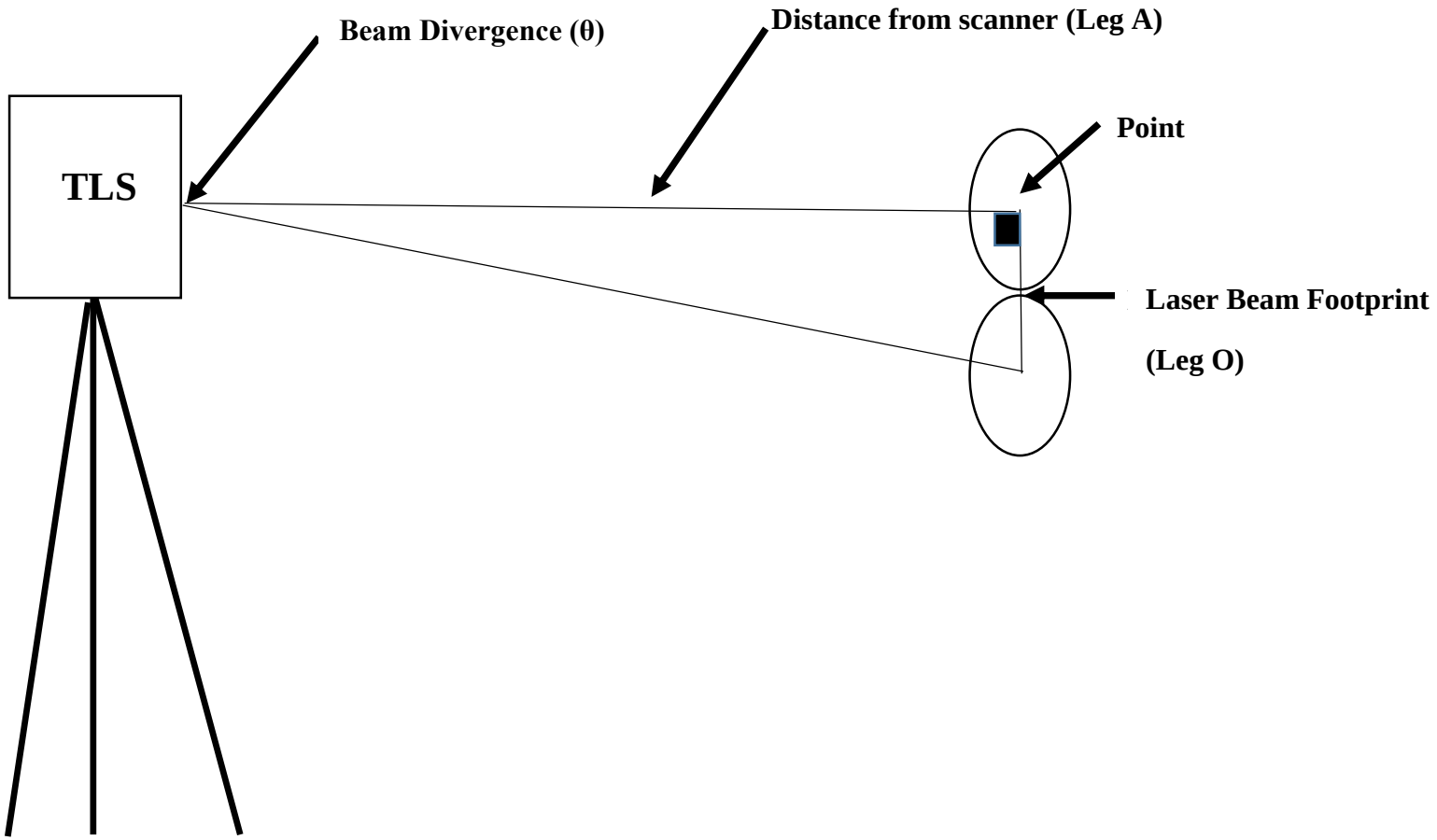

Figure 4.1: Principle of TLS data collection. Recorded points are the Cartesian XY center of the 2.8 mm laser footprint.

Figure 4.2: Depiction of the USC Protype Machine Shop developed ‘howitzer’ used to hoist the Leica P20 in the saltmarsh.

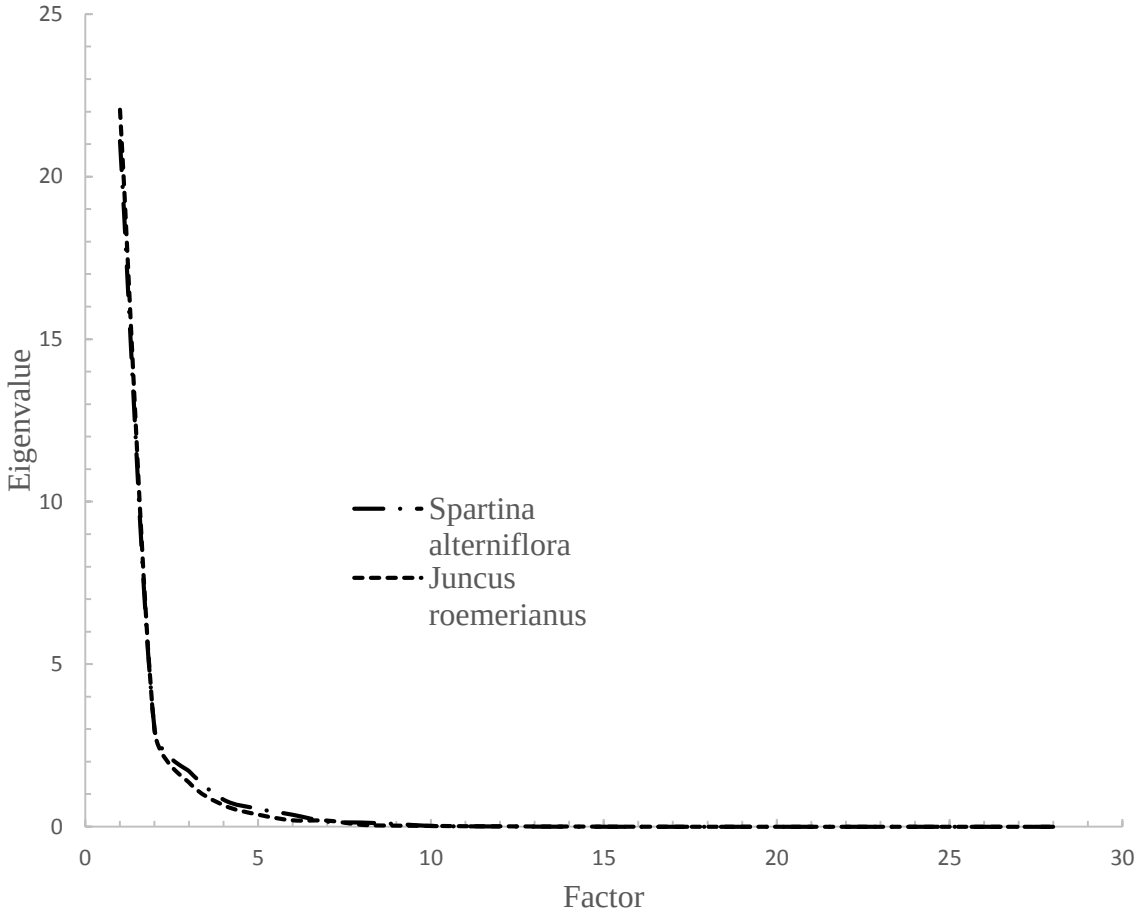

Figure 4.3. Scree plot of *S. alterniflora* and *J. roemerianus* factor number vs respective eigenvalue.

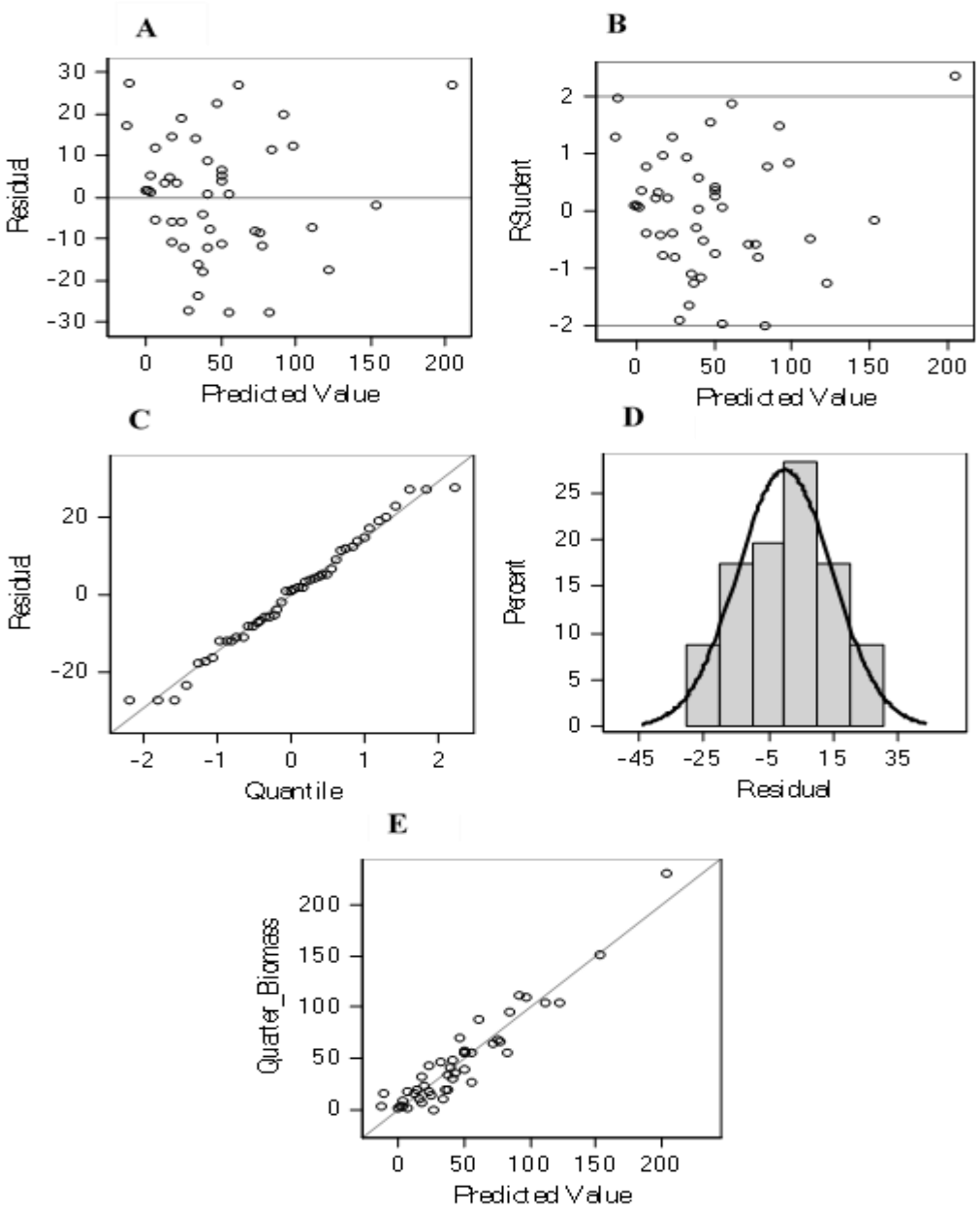

Figure 4.4: *S. alterniflora* model diagnostics for the best fit linear model after removing the bottom 5% of intensity returns. Residual behavior (A) and normalized residual behavior (B) compared against model predicted biomass estimates. Residual quantile plot (C) is provided to depict behavior of residuals as compared to a normal distribution (diagonal). Distribution of residuals (D) used to depict the histogram of residuals compared to a normal distribution. Model predicted biomass vs actual field measured biomass is depicted in Panel E.

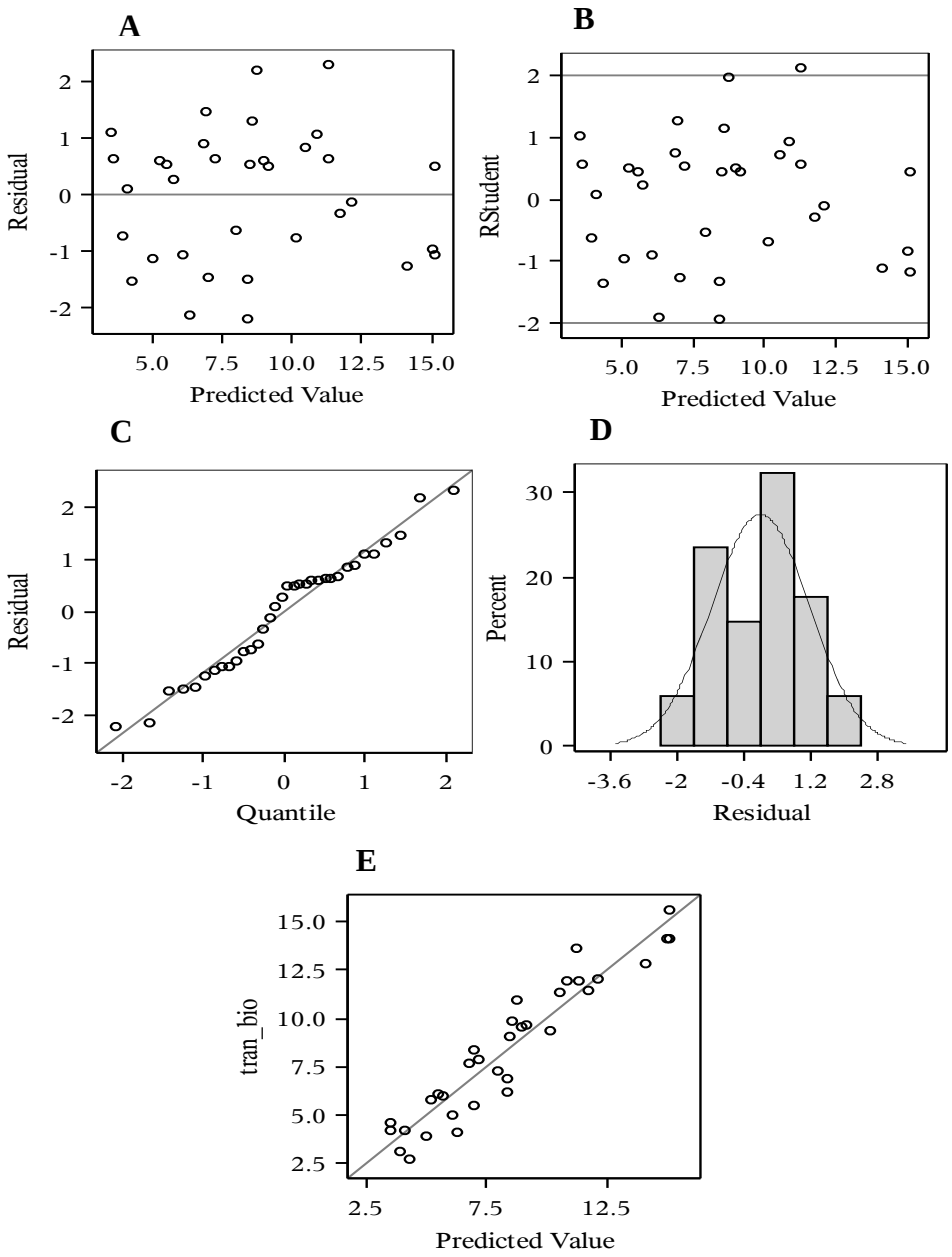

Figure 4.5*: J. roemerianus* model diagnostics for the best fit linear model removing no intensity returns. Residual behavior (A) and normalized residual behavior (B) compared against model predicted biomass estimates. Residual quantile plot (C) is provided to depict behavior of residuals as compared to a normal distribution (diagonal). Distribution of residuals (D) used to depict the histogram of residuals compared to a normal distribution. Model predicted biomass vs transformed actual field measured biomass is depicted in Panel E. Square root transformation of the dependent variable biomass justified from boxcox analysis (λ=0.5).

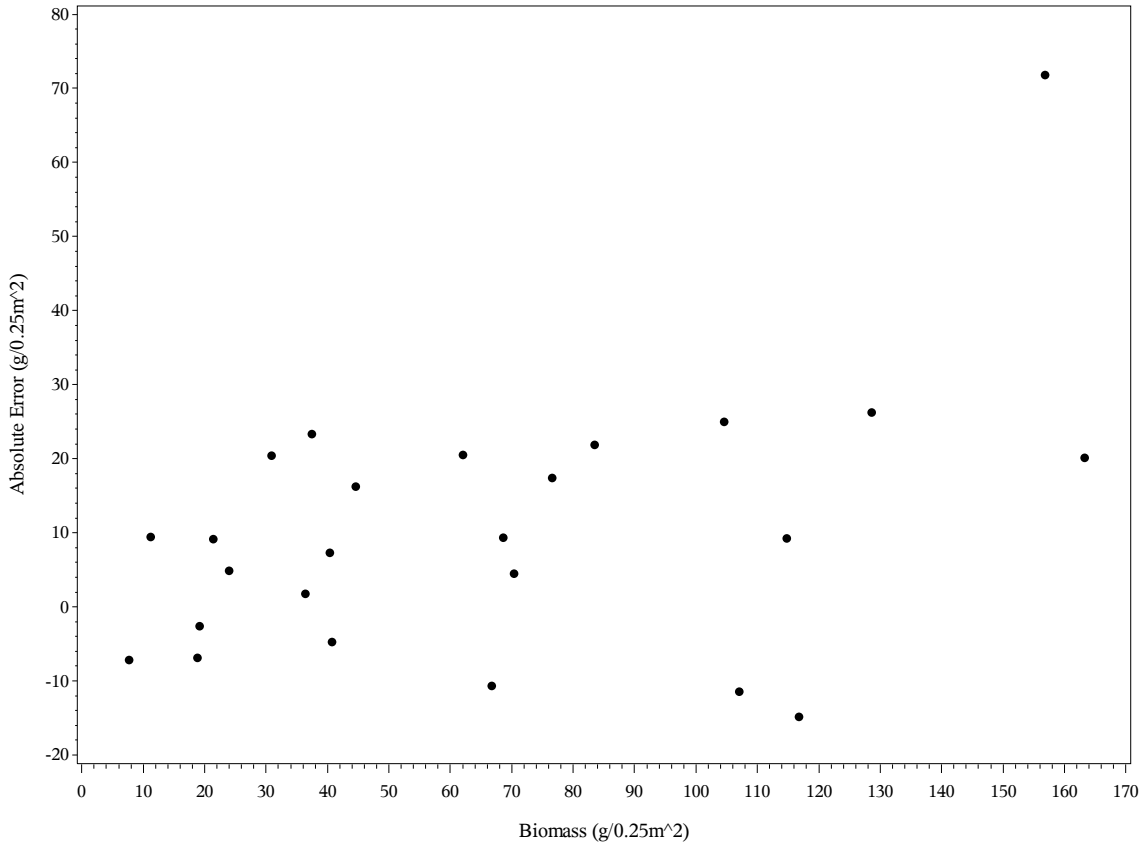

Figure 4.6. *S. alterniflora* biomass vs absolute error.

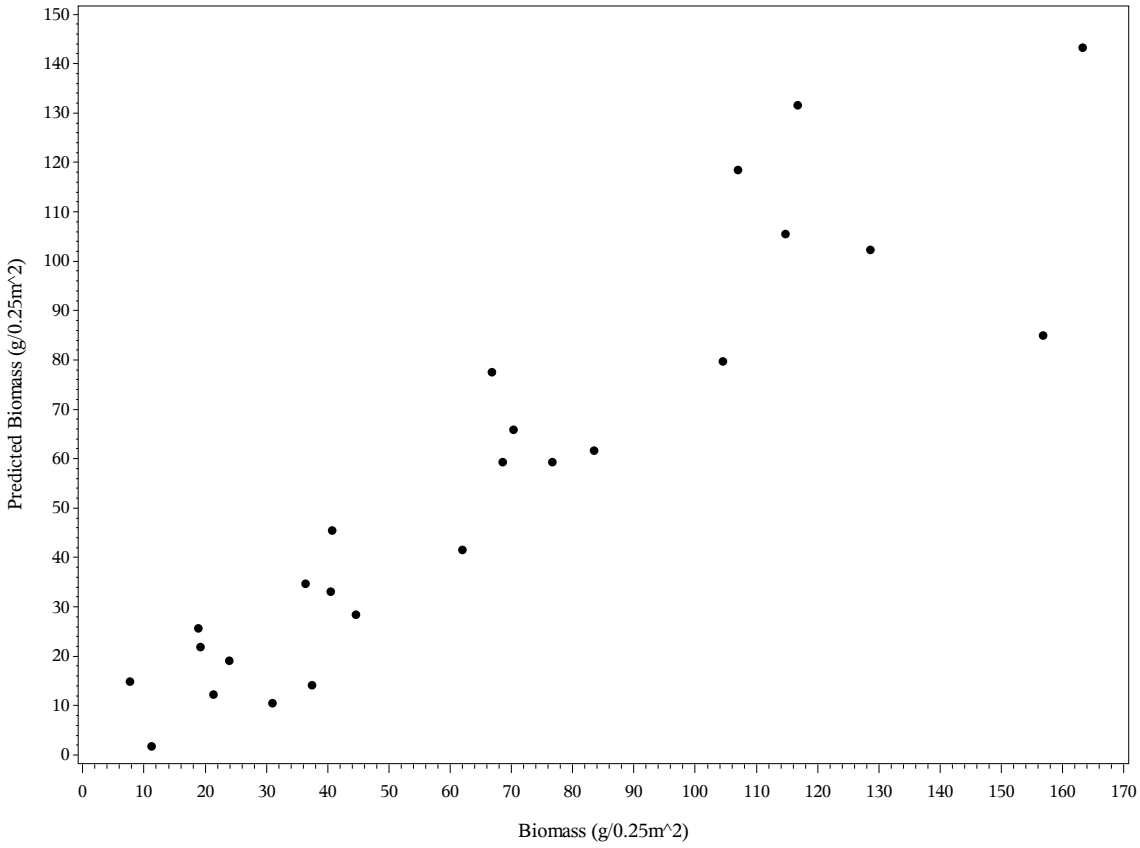

Figure 4.7. *S. alterniflora* biomass vs. predicted biomass.

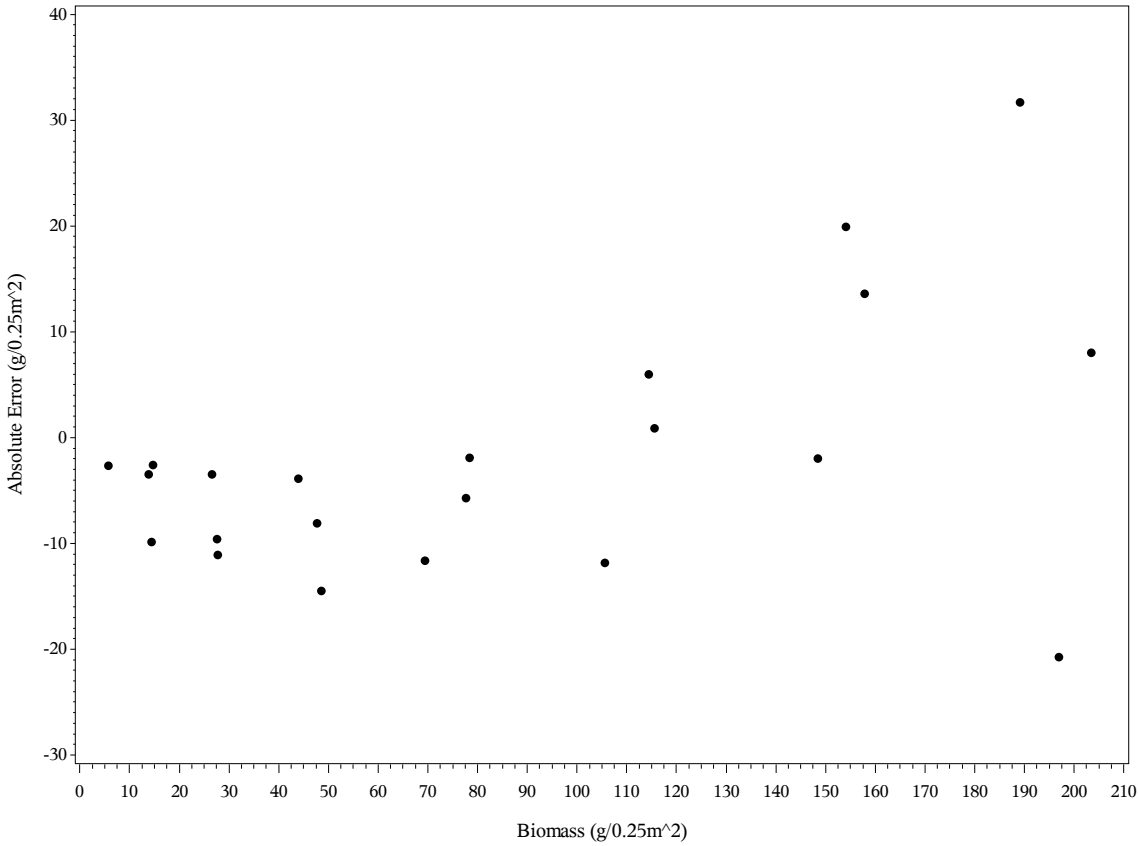

Figure 4.8. *J. roemerianus* biomass vs absolute error.

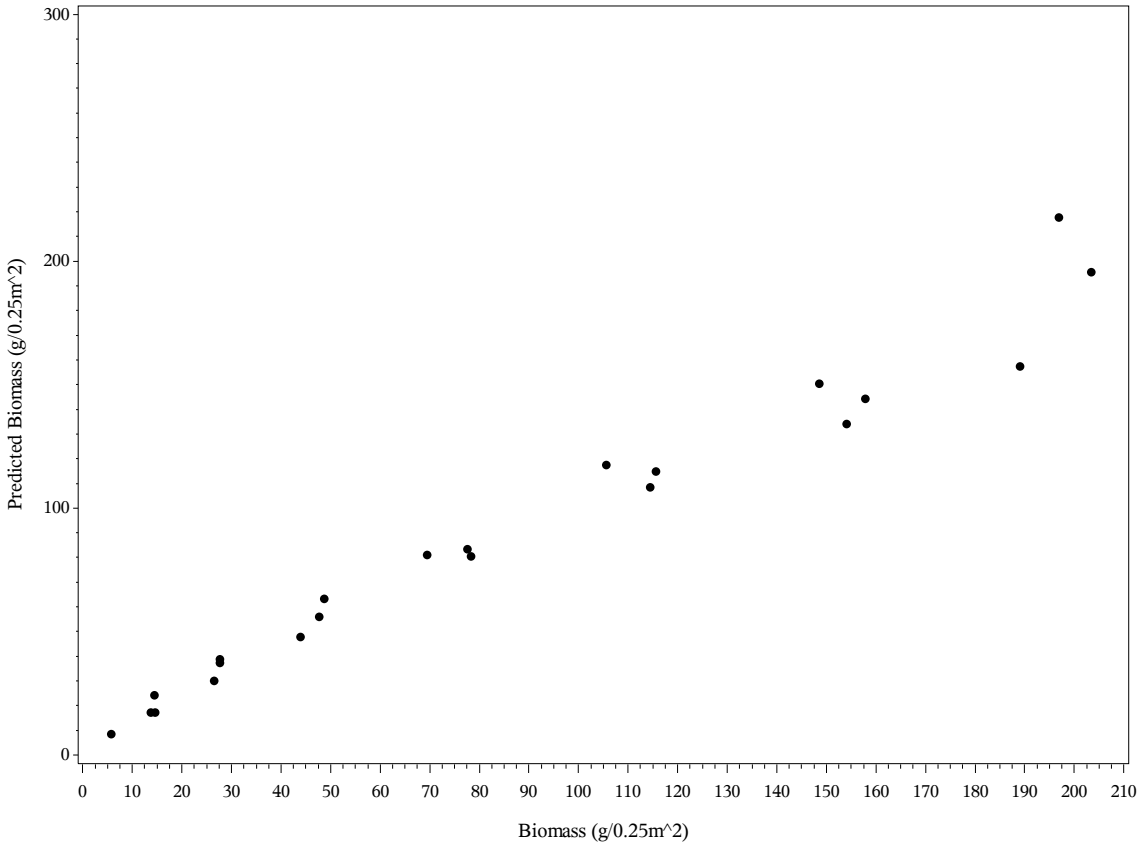

Figure 4.9. *J. roemerianus* biomass vs predicted biomass.

Chapter 5: Conclusion

The use of LiDAR technology in saltmarshes enables scientists to analyze the effects of climate change and sea-level rise during the next century in a variety of ways. The research presented herein demonstrates multiple ways that the use of LiDAR technology contributes to understanding saltmarsh dynamics. Landscape-scale elevation models provide high accuracy elevation corroborated by ground-based surface elevation tables, particularly when data is collected when vegetation is absent and is corrected for noise. These datasets, augmented with classified land cover, provide a detailed description of the elevation frequency distribution associated with zonal patterns observed in halophytic vegetation. This data provides the necessary information to model trends in species distributions as a function of sea-level rise. An additional contribution of landscape-scale LiDAR is the availability of georeferenced elevation for inclusion in zero-dimensional models accounting for vegetative feedback during modeled sea-level rise. The georeferenced elevation provides a means to link spatial procedures of a GIS to analyze marsh dynamics, specifically addressing the question of where saltmarsh change will occur. A final contribution of LiDAR technology to saltmarsh studies is demonstrated with the use of a terrestrial laser scanner (TLS) to produce estimates of saltmarsh biomass that are not the result of destructive harvesting.

A spatial model was used with classified land cover to predict the current and future distribution of Plum Island Estuary (PIE), Massachusetts, salt marshes. This model

was a bathtub model that disregarded any vegetative feedback mechanisms, such as capture of suspended solids. This was deemed appropriate for an initial assessment of the response of PIE to sea level rise as PIE is sediment-limited, with very small amounts of sediment entering the system. Data reported from a land cover classification indicate that in 2011 PIE was dominated by large *S. patens* meadows with a smaller coverage of fringing *S. alterniflora*. Modelling an accelerating sea-level rise of 1 m over 100 years resulted in increases of intertidal area with a complete species turnover to *S. alterniflora* dominance expected to occur by approximately 2030.

An initial version of MEM3D has been written in the freely available Python programming language with only a single external software license needed – ArcGIS. The MEM3D includes vegetative feedback, by accounting for the accumulation of belowground biomass as well as vegetation capture of suspended solids, a mechanism ignored in other spatial models such as SLAMM. Input spatial data was kept to a minimum of any freely available LiDAR dataset and an associated boundary for analysis. The optimal resolution for input LiDAR DEM's, assuming landscape-scale graphics, is 5 m for the NI-Winyah Bay study site. This resolution has the most accurate elevations (0 m mean, 0.11 m standard deviation) and area (+0.01%) when aggregated from 1 m LiDAR. Data indicate that the model produces satisfactory landscape-scale results clearly identifying temporal transitions in coastal land cover. Results from modelling a 1 m SLR this century for NI-Winyah Bay suggest the saltmarshes are migrating inland with SLR thereby expanding area. The expansion of area, however, is misleading as the saltmarshes are losing elevation relative to MSL within every 10-year model iteration. The saltmarshes will reach a tipping point in approximately 40 years when SLR is expected to

exceed 0.86 cm/year. By the end of the simulation, the estuary will shift from current saltmarsh dominance to mudflat. Total aboveground biomass decreased 27.51% from a 2007 level of 31,047.15 kg/km^2.

Aboveground biomass is a critical component of MEM3D that contributes to increases in vertical elevation of the marsh platform through organic production and trapping of mineral sediment. Traditionally biomass is harvested through destructive means for lab analysis. With the recent development of terrestrial laser scanners it is possible to obtain this data in a quick and non-destructive method for salt marshes. Regression of aboveground standing biomass against TLS-derived point cloud statistics provides satisfactory biomass predictive models for *S. alterniflora* and *J. roemerianus*. It was found that the optimal resolution for data collection in saltmarshes is 6.3 mm at 10 m height and that this resolution provides a density sufficient to penetrate all layers of the canopy. Principle components analysis indicates that there exists four significant factors for *S. alterniflora* and 3 for *J. roemerianus*. The quality of point cloud returns was found to effect the predictive power of *S. alterniflora*, not *J. roemerianus*. Final biomass predictors were highly correlated (R^2=0.89 for both species). Verification of the models against independent data suggests *S. alterniflora* is underestimated an average of 10.39 g/0.25 m^2 and *J. roemerianus* is overestimated an average of 4.31 g/0.25 m^2.

Results from the presented modelling analyses are dependent on the rate of sea-level rise and can be described as conservative estimates. Although recent studies suggest global sea levels will rise 1 m in the next century (Craft et al. 2008; Schile et al. 2014), newly published studies suggest a higher rate exceeding several meters within the century (Hansen et al. 2016). Sea-level rise exceeding the modelled 1 m assumption would result

in quicker species turnover and saltmarsh collapse than reported from the findings. The presented models do not address topics such as erosion or tide creek expansion. While it is known that erosion increases and tide creeks expand with increasing tidal volume (Kirwan & Guntenspergen 2010), modelling these changes was beyond the scope of the analyses. Inclusion of these dynamics would ultimately increase the predictive power of the developed MEM3D.

This thesis demonstrates the capacity for using LiDAR technology as a tool to assess landscape response to changes in sea level rise. Classified land cover should continue to be used with landscape-scale LiDAR to not only differentiate species elevation frequency distributions, but also provide estimates of vertical error associated with canopy structure. A TLS is capable of penetrating the dense canopy of saltmarsh vegetation to collect data representative of the entire vertical distribution of biomass. This finding provides the opportunity to model three-dimensional canopy structure that, when coupled with species classification and coincident with airborne LiDAR missions, can aid in the identification of species and biomass-dependent vertical error in the airborne dataset. Despite the limitations included within the presented analyses, the results provide direction for future research on the use of LiDAR technologies in saltmarshes and provide immediate tools for stakeholders in saltmarsh management. The methods used in this research are intended to be used to identify the most stable saltmarshes where limited resources can be directed to protect these valuable ecosystems.

Works Cited

Adriaensen, F., Chardon, J. P., De Blust, G., Swinnen, E., Villalba, S., Gulinck, H., & Matthysen, E. (2003). The application of 'least-cost' modelling as a functional landscape model. *Landscape and urban planning*, *64*(4), 233-247.

Alexander, C.R. & Robinson, M.H., (2004). GIS and field-based analysis of the impacts of recreational docks on the saltmarshes of Georgia. Technical report prepared for the Georgia coastal zone management program. Georgia Department of Natural Resources. Coastal Resource Division. Brunswick, GA.

Alonso, M. C., & Malpica, J. A. (2010). Satellite imagery classification with LiDAR data. *Trees* (A), 2106(19), 11.

Antonarakis, A. S., Richards, K. S., Brasington, J., & Muller, E. (2010). Determining leaf area index and leafy tree roughness using terrestrial laser scanning. *Water Resources Research*, *46*(6).

Artigas, F. J., & Yang, J. (2006). Spectral discrimination of marsh vegetation types in the New Jersey Meadowlands, USA. *Wetlands*, *26*(1), 271-277.

Baart, F., Van Gelder, P. H., De Ronde, J., Van Koningsveld, M., & Wouters, B. (2011). The effect of the 18.6-year lunar nodal cycle on regional sea-level rise estimates. *Journal of Coastal Research*, *28*(2), 511-516.

Baldwin, I., & Newman, P. (2012, May). Road vehicle localization with 2D push-broom LIDAR and 3D priors. In *Robotics and automation (ICRA), 2012 IEEE international conference on* (pp. 2611-2617). IEEE.

Barbier, E. B. (2012). Progress and challenges in valuing coastal and marine ecosystem services. *Review of Environmental Economics and Policy*, *6*(1), 1-19.

Bartholdy, A. T., Bartholdy, J., & Kroon, A. (2010). Salt marsh stability and patterns of sedimentation across a back barrier platform. *Marine Geology*, *278*(1), 31-42.

Baskerville, G. L. (1972). Use of logarithmic regression in the estimation of plant biomass. *Canadian Journal of Forest Research*, *2*(1), 49-53.

Bertness, M. D., & Ellison, A. M. (1987). Determinants of pattern in a New England salt marsh plant community. *Ecological Monographs*, 129-147.

Bouma, T. J., Van Duren, L. A., Temmerman, S., Claverie, T., Blanco-Garcia, A., Ysebaert, T., & Herman, P. M. J. (2007). Spatial flow and sedimentation patterns within patches of epibenthic structures: combining field, flume and modelling experiments. *Continental Shelf Research*, *27*(8), 1020-1045.

Brinson, M. M., Christian, R. R., & Blum, L. K. (1995). Multiple states in the sea-level induced transition from terrestrial forest to estuary. *Estuaries*, *18*(4), 648-659.

Cavatorta, J. R., Johnston, M., Hopkinson, C., & Valentine, V. (2003). Patterns of sedimentation in a salt marsh-dominated estuary. *The Biological Bulletin*, *205*(2), 239-241.

Chai, T., & Draxler, R. R. (2014). Root mean square error (RMSE) or mean absolute error (MAE)?–Arguments against avoiding RMSE in the literature. *Geoscientific Model Development*, *7*(3), 1247-1250.

Chai, T., Kim, H.C., Lee, P., Tong, D., Pan, L., Tang, Y., Huang, J., McQueen, J., Tsidulko, M., & Stajner, I. (2013). Evaluation of the United States National Air Quality Forecast Capability experimental real-time predictions in 2010 using Air Quality System ozone and NO_2 measurements, *Geosci. Model Dev.*, 6, 1831–1850.

Chang, K.T. (2008). Viewsheds and watersheds. In Chang, K. T. (eds.), Introduction to geographic information systems (4^{th} edition; p302-325). McGraw-Hill New York, NY.

Chassereau, J. E., Bell, J. M., & Torres, R. (2011). A comparison of GPS and LIDAR salt marsh DEMs. *Earth Surface Processes and Landforms*, *36*(13), 1770-1775.

Chmura, G. L. (2011). What do we need to assess the sustainability of the tidal salt marsh carbon sink? *Ocean & Coastal Management*, *83*, 25-31.

Craft, C., Clough, J., Ehman, J., Joye, S., Park, R., Pennings, S., & Machmuller, M. (2008). Forecasting the effects of accelerated sea-level rise on tidal marsh ecosystem services. *Frontiers in Ecology and the Environment*, *7*(2), 73-78.

Craft, C.B., Seneca, E.D., & S.W. Broome. (1991). Loss on ignition and digestion for estimating organic carbon and total nitrogen in estuarine marsh soils: calibration with dry combustion. *Estuaries*, 14 (2), 175-179.

Dassot, M., Constant, T., & Fournier, M. (2011). The use of terrestrial LiDAR technology in forest science: application fields, benefits and challenges. *Annals of Forest Science*, *68*(5), 959-974.

Devauchelle, O., Petroff, A. P., Seybold, H. F., & Rothman, D. H. (2012). Ramification of stream networks. *Proceedings of the National Academy of Sciences*, *109*(51), 20832-20836.

Drake, J. B., Dubayah, R. O., Clark, D. B., Knox, R. G., Blair, J. B., Hofton, M. A., Chazdon, R. L., Weishampel, J. F., & Prince, S. (2002). Estimation of tropical forest structural characteristics using large-footprint lidar. *Remote Sensing of Environment*, *79*(2), 305-319.

Drake, J. B., Knox, R. G., Dubayah, R. O., Clark, D. B., Condit, R., Blair, J. B., & Hofton, M. (2003). Above-ground biomass estimation in closed canopy neotropical forests using LIDAR remote sensing: factors affecting the generality of relationships. *Global Ecology and Biogeography*, *12*(2), 147-159.

Eitel, J. U., Vierling, L. A., & Magney, T. S. (2013). A lightweight, low cost autonomously operating terrestrial laser scanner for quantifying and monitoring ecosystem structural dynamics. *Agricultural and Forest Meteorology*, *180*, 86-96.

Feagin, R. A., M. Luisa Martinez, G. Mendoza-Gonzalez, & R. Costanza. (2010). Salt Marsh Zonal Migration and Ecosystem Service Change in Response to Global Sea-Level Rise: A Case Study from an Urban Region. *Ecology and Society*, 15(4), 14.

Fielding, A. H., & Bell, J. F. (1997). A review of methods for the assessment of prediction errors in conservation presence/absence models. *Environmental conservation*, *24*(01), 38-49.

Foody, G. M. (2002). Status of land cover classification accuracy assessment. *Remote sensing of environment*, *80*(1), 185-201.

French, J. (2006). Tidal marsh sedimentation and resilience to environmental change: exploratory modelling of tidal, sea-level and sediment supply forcing in predominantly allochthonous systems. *Marine Geology*, *235*(1), 119-136.

Gallagher, J.L. (1975). Effect of ammonium nitrate pulse on the growth and elemental composition of natural stands of *Spartina alterniflora* and *Juncus roemerianus*. *American Journal of Botany*, 62 (6): 644-648

García, M., Riaño, D., Chuvieco, E., & Danson, F. M. (2010). Estimating biomass carbon stocks for a Mediterranean forest in central Spain using LIDAR height and intensity data. *Remote Sensing of Environment*, *114*(4), 816-830.

Gedan, K. B., Altieri, A. H., & Bertness, M. D. (2011). Uncertain future of New England salt marshes. *Marine Ecology Progress Series*, *434*, 229-237.

Gedan, K. B., Kirwan, M. L., Wolanski, E., Barbier, E. B., & Silliman, B. R. (2011). The present and future role of coastal wetland vegetation in protecting shorelines: answering recent challenges to the paradigm. *Climatic Change*, *106*(1): 7-29.

Gedan, K. B., Silliman, B. R., & Bertness, M. D. (2009). Centuries of human-driven change in salt marsh ecosystems. *Annual Review of Marine Science*, *1*: 117-141.

Gesch, D. B. (2009). Analysis of LiDAR elevation data for improved identification and delineation of lands vulnerable to sea-level rise. *Journal of Coastal Research*, 49-58.

Gross, M.F., Hardisky M.A., & Klemas, V. (1990). Inter-annual spatial variability in the response of *Spartina alterniflora* biomass to amount of precipitation. *Journal of Coastal Research*: 949–960.

Hansen, J., Sato, M., Hearty, P., Ruedy, R., Kelley, M., Masson-Delmotte, V., Russell, G., Tselioudis, G., Cao, J., Rignot, E. and Velicogna, I. (2016). Ice melt, sea level rise and superstorms: evidence from paleoclimate data, climate modeling, and modern observations that 2° C global warming could be dangerous. *Atmospheric Chemistry and Physics*, 16(6), 3761-3812.

Henning, J. G., & Radtke, P. J. (2006). Detailed stem measurements of standing trees from ground-based scanning LiDAR. *Forest Science*, *52*(1), 67-80.

Hladik, C., & Alber, M. (2012). Accuracy assessment and correction of a LIDAR-derived salt marsh digital elevation model. *Remote Sensing of Environment*, *121*, 224-235.

Hodgson, M. E., & Bresnahan, P. (2004). Accuracy of airborne LIDAR-derived elevation. *Photogrammetric Engineering & Remote Sensing*, *70*(3), 331-339.

Hopkinson, C., Chasmer, L., Young-Pow, C., & Treitz, P. (2004). Assessing forest metrics with a ground-based scanning LiDAR. *Canadian Journal of Forest Research*, *34*(3), 573-583.

Hughes, Z. J., FitzGerald, D. M., Wilson, C. A., Pennings, S. C., Więski, K., & Mahadevan, A. (2009). Rapid headward erosion of marsh creeks in response to relative sea level rise. *Geophysical Research Letters*, *36*(3).

Jensen, J. R. (1996). *Remote sensing of the environment: An earth resource perspective 2/e*. Pearson Education India.

Jenson, S. K., & Domingue, J. O. (1988). Extracting topographic structure from digital elevation data for geographic information system analysis. *Photogrammetric engineering and remote sensing*, *54*(11), 1593-1600.

Johnson, D. S. (2014). Fiddler on the roof: a northern range extension for the marsh fiddler crab *Uca pugnax*. *Journal of Crustacean Biology*, *34*(5), 671-673.

Johnson, D., S. (2015). The savory swimmer swims North: A northern range extension of the blue crab *Callinectes sapidus*? *Journal of Crustacean Biology*, 35, 105-110.

Kim, D., Cairns, D.M., & Bartholdy, J. (2010). Environmental controls on multiscale spatial patterns of salt marsh vegetation. *Physical Geography*, 31 (1), 58–78.

Kirwan, M.L., Christian R.R., Blum, L.K., & Brinson, M.M. (2012). On the relationship between sea level and *spartina alterniflora* production. *Ecosystems*, 15 (1), 140–147.

Kirwan, M. L., & Guntenspergen, G. R. (2010). Influence of tidal range on the stability of coastal marshland. *Journal of Geophysical Research: Earth Surface*, *115*(F2).

Kirwan, M. L., Guntenspergen, G. R., D'Alpaos, A., Morris, J. T., Mudd, S. M., & Temmerman, S. (2010). Limits on the adaptability of coastal marshes to rising sea level. *Geophysical Research Letters*, *37*(23).

Kirwan, M. L., & Megonigal, J. P. (2013). Tidal wetland stability in the face of human impacts and sea-level rise. *Nature*, *504*(7478), 53-60.

Krone, R. B. (1985). Simulation of marsh growth under rising sea levels. In *Hydraulics and hydrology in the small computer age* (pp. 106-115). ASCE.

Landis, J. R., & Koch, G. G. (1977). The measurement of observer agreement for categorical data. *biometrics*, 159-174.

Lefsky, M. A., Cohen, W. B., Acker, S. A., Parker, G. G., Spies, T. A., & Harding, D. (1999). Lidar remote sensing of the canopy structure and biophysical properties of Douglas-fir western hemlock forests. *Remote sensing of environment*, *70*(3), 339-361.

Leica Geosystems. (2016a). HDS Laser Scanners & SW. Retrieved from http://www.leica-geosystems.us/en/HDS-Laser-Scanners-SW_5570.htm.

Leica Geosystems. (2016b). Leica Cyclone. Retrieved from http://hds.leica-geosystems.com/en/Leica-Cyclone_6515.htm.

Leonard, L. A., & Croft, A. L. (2006). The effect of standing biomass on flow velocity and turbulence in *spartina alterniflora* canopies. *Estuarine, Coastal and Shelf Science*, *69*(3), 325-336.

Leonard, L. A., & Luther, M. E. (1995). Flow hydrodynamics in tidal marsh canopies. *Limnology and Oceanography*, *40*(8), 1474-1484.

Leonard, L. A., & Reed, D. J. (2002). Hydrodynamics and sediment transport through tidal marsh canopies. *Journal of Coastal Research*, *36*(2), 459-469.

Lin, Y., Jaakkola, A., Hyyppä, J., & Kaartinen, H. (2010). From TLS to VLS: biomass estimation at individual tree level. *Remote Sensing*, *2*(8), 1864-1879.

Loudermilk, E. L., Hiers, J. K., O'Brien, J. J., Mitchell, R. J., Singhania, A., Fernandez, J. C., Cropper, W.P., & Slatton, K. C. (2009). Ground-based LiDAR: a novel approach to quantify fine-scale fuelbed characteristics. *International Journal of Wildland Fire*, *18*(6), 676-685.

Luettich Jr, R. A., Westerink, J. J., & Scheffner, N. W. (1992). *ADCIRC: an advanced three-dimensional circulation model for shelves, coasts, and estuaries. Report 1. Theory and methodology of ADCIRC-2DDI and ADCIRC-3DL* (No. CERC-TR-DRP-92-6). Coastal engineering research center. Vicksburg, MS.

Marani, M., Da Lio, C., & D'Alpaos, A. (2013). Vegetation engineers marsh morphology through multiple competing stable states. *Proceedings of the National Academy of Sciences*, *110*(9), 3259-3263.

McGranahan, G., Balk, D., & Anderson, B. (2007). The rising tide: assessing the risks of climate change and human settlements in low elevation coastal zones. *Environment and urbanization*, *19*(1), 17-37.

McKeen, S., Wilczak, J., Grell, G., Djalalova, I., Peckham, S., Hsie, E. Y., ... & McHenry, J. (2005). Assessment of an ensemble of seven real-time ozone forecasts over eastern North America during the summer of 2004. *Journal of Geophysical Research: Atmospheres*, *110*(D21).

Means, J.E., Acker, S.A., Harding, D.J., Blair, J.B., Lefsky, M.A., Cohen, W.B., Harmon, M.E., & McKee, W.A. (1999). Use of large-footprint scanning airborne LiDAR to estimate forest stand characteristics in the western Cascades of Oregon. *Remote Sensing of Environment*, 67(3), 298-308.

Michel, P., Jenkins, J., Mason, N., Dickinson, K. J. M., & Jamieson, I. G. (2008). Assessing the ecological application of lasergrammetric techniques to measure fine-scale vegetation structure. *Ecological Informatics*, *3*(4), 309-320.

Millette, T. L., Argow, B. A., Marcano, E., Hayward, C., Hopkinson, C. S., & Valentine, V. (2010). Salt marsh geomorphological analyses via integration of multitemporal multispectral remote sensing with LIDAR and GIS. *Journal of Coastal Research*, 809-816.

Montane, J. M., & Torres, R. (2006). Accuracy assessment of LIDAR saltmarsh topographic data using RTK GPS. *Photogrammetric Engineering & Remote Sensing*, *72*(8), 961-967.

Moorhead, K. K., & Brinson, M. M. (1995). Response of wetlands to rising sea level in the lower coastal plain of North Carolina. *Ecological Applications*, 261-271.

Morris, J. T. (2007). Ecological engineering in intertidal saltmarshes. *Hydrobiologia*, *577*(1), 161-168.

Morris, J. T., Porter, D., Neet, M., Noble, P. A., Schmidt, L., Lapine, L. A., & Jensen, J. R. (2005). Integrating LIDAR elevation data, multi-spectral imagery and neural network modelling for marsh characterization. *International Journal of Remote Sensing*, *26*(23), 5221-5234.

Morris, J. T., Shaffer, G. P., & Nyman, J. A. (2013). Brinson review: Perspectives on the influence of nutrients on the sustainability of coastal wetlands. *Wetlands*, *33*(6), 975-988.

Morris, J. T., Sundareshwar, P. V., Nietch, C. T., Kjerfve, B., & Cahoon, D. R. (2002). Responses of coastal wetlands to rising sea level. *Ecology*, *83*(10), 2869-2877.

Morris, J. T., Sundberg, K., & Hopkinson, C. S. (2013). Salt marsh primary production and its responses to relative sea level and nutrients. *Oceanography*, 26, 78-84.

Mudd, S. M., D'Alpaos, A., & Morris, J. T. (2010). How does vegetation affect sedimentation on tidal marshes? Investigating particle capture and hydrodynamic controls on biologically mediated sedimentation. *Journal of Geophysical Research: Earth Surface*, *115*(F3).

Nepf, H. M., & Vivoni, E. R. (2000). Flow structure in depth-limited, vegetated flow. *Journal of Geophysical Research: Oceans*, *105*(C12), 28547-28557.

Najjar, R.G., Pyke, C.R., Adams, M.B., Breitburg, D., Hershner, C., Kemp, M., Howarth, R., Mulholland, M.R., Paolisso, M. Secor, D., Sellner, K., Wardop, D., & R. Wood. (2010). Potential climate change impacts on the Chesapeake Bay. *Estuarine, Coastal, and Shelf Science*, 86: 1-20.

National Geodetic Survey. (2016, Jan. 25). Vertical Datums. Retrieved April 1, 2016 from http://www.ngs.noaa.gov/datums/vertical/.

National Oceanic and Atmospheric Administration. (2013a, Oct. 15). Tides and currents. Tidal datums. Retrieved Dec. 1, 2013, from http://tidesandcurrents.noaa.gov/datum_options.html.

National Oceanic and Atmospheric Administration. (2013b, Oct. 15). Tides and currents. Datums for 8443970, Boston, MA. Retrieved Nov. 13, 2013, from http://tidesandcurrents.noaa.gov/datums.html?id=8443970.

National Oceanic and Atmospheric Administration. (2013c, Oct. 15). Tides and currents. Mean Sea Level Trend 8443970 Boston, Massachusetts. Retrieved Nov. 13, 2013, from http://tidesandcurrents.noaa.gov/sltrends/sltrends_station.shtml?stnid=8443970.

National Oceanic and Atmospheric Administration. (2013d, Oct. 15). Tides and currents. Datums for 8662245, Oyster Landing (N. Inlet estuary), SC. Retrieved July 15, 2015, from http://tidesandcurrents.noaa.gov/datums.html?id=8662245.

Nelson, J. A., Deegan, L., & Garritt, R. (2015). Drivers of spatial and temporal variability in estuarine food webs. *Marine Ecology Progress Series*, *533*, 67-77.

Nelson, R., Krabill, W., & Tonelli, J. (1988). Estimating forest biomass and volume using airborne laser data. *Remote sensing of environment*, *24*(2), 247-267.

Nepf, H. M., & Vivoni, E. R. (2000). Flow structure in depth-limited, vegetated flow. *Journal of Geophysical Research: Oceans*, *105*(C12), 28547-28557.

Nydick, K. R., Bidwell, A. B., Thomas, E., & Varekamp, J. C. (1995). A sea-level rise curve from Guilford, Connecticut, USA. *Marine Geology*, *124*(1), 137-159.

O'brien, R. M. (2007). A caution regarding rules of thumb for variance inflation factors. *Quality & Quantity*, *41*(5), 673-690.

Olsoy, P. J., Glenn, N. F., & Clark, P. E. (2014). Estimating sagebrush biomass using terrestrial laser scanning. *Rangeland Ecology and Management*, *67*(2), 224-228.

Orson, R. A., Warren, R. S., & Niering, W. A. (1998). Interpreting sea level rise and rates of vertical marsh accretion in a southern New England tidal salt marsh. *Estuarine, Coastal and Shelf Science*, *47*(4), 419-429.

Osgood, D.T., and J.C. Zieman. (1993). Factors controlling aboveground *Spartina alterniflora* (smooth cordgrass) tissue element composition and production in different-age barrier island marshes. *Estuaries*, 16 (4), 815-826.

Peterson, C.H., Luettich, R.A., Micheli, F., & Skilleter, G.A. (2004). Attenuation of water flow inside seagrass canopies of differing structure. *Marine Ecology Progress Series,* 268, 81–92.

Pontius Jr, R. G., & Millones, M. (2011). Death to Kappa: birth of quantity disagreement and allocation disagreement for accuracy assessment. *International Journal of Remote Sensing*, *32*(15), 4407-4429.

Popescu, S. C., Wynne, R. H., & Nelson, R. F. (2003). Measuring individual tree crown diameter with lidar and assessing its influence on estimating forest volume and biomass. *Canadian Journal of Remote Sensing*, *29*(5), 564-577.

Popescu, S. C., Wynne, R. H., & Scrivani, J. A. (2004). Fusion of small-footprint lidar and multispectral data to estimate plot-level volume and biomass in deciduous and pine forests in Virginia, USA. *Forest Science*, *50*(4), 551-565.

Redfield, A. C. (1972). Development of a New England salt marsh. *Ecological Monographs*, 201-237.

Redfield, A.C., & Ruben, M. (1962). The age of salt marsh peat and its relation to sea level at Barnstable, Massachusetts. *Proc. Nat. Acad. Sci*., 48(10), 1728-1735.

Roman, C. T., Jaworski, N., Short, F. T., Findlay, S., & Warren, R. S. (2000). Estuaries of the northeastern United States: habitat and land use signatures. *Estuaries*, *23*(6), 743-764.

Rosell, J. R., Llorens, J., Sanz, R., Arnó, J., Ribes-Dasi, M., Masip, J., Escola, A., Camp, F., Solanellas, F., Gracia, F., Gil, E., Val, L., Planas, S., & Palacín, J. (2009). Obtaining the 3D structure of tree orchards from remote 2D terrestrial LIDAR scanning. *Agricultural and Forest Meteorology*, *149*(9), 1505-1515.

Rosso, P.H., Ustin, S.L., & Hastings, A. (2006). Use of LiDAR to study changes associated with *Spartina* invasion in San Francisco bay marshes. *Remote Sensing of Environment*, 100 (3), 295–306.

Rowell, E., & Seielstad, C. (2012). Characterizing grass, litter, and shrub fuels in longleaf pine forest pre-and post-fire using terrestrial LiDAR. *Proceedings of SilviLaser*, 16-19.

Sadro, S., Gastil-Buhl, M., & Melack, J. (2007). Characterizing patterns of plant distribution in a southern California salt marsh using remotely sensed topographic and hyperspectral data and local tidal fluctuations. *Remote Sensing of Environment*, 110 (2), 226–239.

Savage, N.H., Agnew, P., Davis, L.S., Ordóñez, C., Thorpe, R., Johnson, C.E., O'Connor, F.M. & Dalvi, M. (2013). Air quality modelling using the met office unified model (AQUM OS24-26): model description and initial evaluation. *Geoscientific Model Development*, *6*(2), 353-372.

Schile, L. M., Callaway, J. C., Morris, J. T., Stralberg, D., Parker, V. T., & Kelly, M. (2014). Modeling tidal marsh distribution with sea-level rise: evaluating the role of vegetation, sediment, and upland habitat in marsh resiliency. *PloS one*, *9*(2), e88760.

Schmitt, C., Weston, N., & Hopkinson, C. (1998). Preliminary evaluation of sedimentation rates and species distribution in Plum Island Estuary, Massachusetts. *Biological Bulletin*, 195, 232-233.

Seidel, D., Beyer, F., Hertel, D., Fleck, S., & Leuschner, C. (2011). 3D-laser scanning: a non-destructive method for studying above-ground biomass and growth of juvenile trees. *Agricultural and Forest Meteorology*, *151*(10), 1305-1311.

Silvestri, S., Defina, A., & Marani, M. (2005). Tidal regime, salinity and salt marsh plant zonation. *Estuarine, Coastal and Shelf Science*, *62*(1), 119-130.

Small, C., & Nicholls, R. J. (2003). A global analysis of human settlement in coastal zones. *Journal of Coastal Research*, 584-599.

Stralberg, D., Brennan, M., Callaway, J. C., Wood, J. K., Schile, L. M., Jongsomjit, D., Kelly, M., Parker, T., & Crooks, S. (2011). Evaluating tidal marsh sustainability in the face of sea-level rise: a hybrid modeling approach applied to San Francisco bay. *PloS one*, *6*(11), e27388.

Tanaka, T., Yamaguchi, J., & Takeda, Y. (1998). Measurement of forest canopy structure with a laser plane range-finding method–development of a measurement system and applications to real forests. *Agricultural and Forest Meteorology*, *91*(3), 149-160.

Temmerman, S., Govers, G., Wartel, S., & Meire, P. (2004). Modelling estuarine variations in tidal marsh sedimentation: response to changing sea level and suspended sediment concentrations. *Marine Geology*, *212*(1), 1-19.

Tonelli, M., Fagherazzi, S., & Petti, M. (2010). Modeling wave impact on salt marsh boundaries. *Journal of Geophysical Research: Oceans*, *115*(C9).

Townend, I., Fletcher, C., Knappen, M., & Rossington, K. (2011). A review of salt marsh dynamics. *Water and Environment Journal*, *25*(4), 477-488.

Tyler, C. (1997). Geomorphological and hydrological controls on patterns and process in a developing barrier island salt marsh. Master's Thesis. University of Virginia.

University of South Carolina. (2008). College of Arts and Sciences Mechanical Prototype Facility. Retrieved from http://artsandsciences.sc.edu/mepf/.

Wandinger, U. (2005). *Introduction to LiDAR* (pp. 1-18). Springer New York.

Warren, R. S., Fell, P. E., Rozsa, R., Brawley, A. H., Orsted, A. C., Olson, E. T., Swammy, V., & Niering, W. A. (2002). Salt marsh restoration in Connecticut: 20 years of science and management. *Restoration Ecology*, *10*(3), 497-513.

Watt, P. J., & Donoghue, D. N. M. (2005). Measuring forest structure with terrestrial laser scanning. *International Journal of Remote Sensing*, *26*(7), 1437-1446.

Willmott, C. J., & Matsuura, K. (2005). Advantages of the mean absolute error (MAE) over the root mean square error (RMSE) in assessing average model performance. *Climate research*, *30*(1), 79.

Willmott, C. J., Matsuura, K., & Robeson, S. M. (2009). Ambiguities inherent in sums-of-squares-based error statistics. *Atmospheric Environment*, *43*(3), 749-752.

Wing, M. G., Eklund, A., & Kellogg, L. D. (2005). Consumer-grade global positioning system (GPS) accuracy and reliability. *Journal of forestry*, *103*(4), 169-173.

Wu, S. Y., Najjar, R., & Siewert, J. (2009). Potential impacts of sea-level rise on the mid-and upper-Atlantic region of the United States. *Climatic Change*, *95*(1-2), 121-138.

Zedler, J. B., & Kercher, S. (2005). Wetland resources: status, trends, ecosystem services, and restorability. *Annual Review of Environmental Resources*, *30*: 39-74.